REPORT DOCUMENTATION PAGE

Form Approved
OMB No. 0704-0188

1. AGENCY USE ONLY (Leave Blank)	2. REPORT DATE 4/25/95	3. REPORT TYPE AND DATES COVERED Final Technical

4. TITLE AND SUBTITLE
Nonlinear Stability of Unsteady Viscous Flow

5. FUNDING NUMBERS
Grant No.:
-F49620-92-J-0097 P00003

2304/BS
61102F

6. AUTHOR(S)
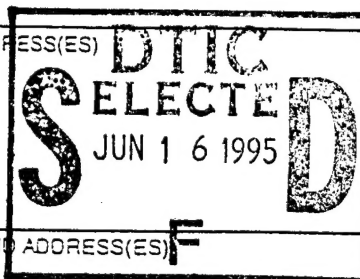A. P. Rothmayer

7. PERFORMING ORGANIZATION NAME(S) AND ADDRESS(ES)
Iowa State University
Contracts and Grants Office
213 Beardshear Hall
Ames, IA 50011

DTIC
SELECTED
JUN 1 6 1995
F

8. PERFORMING ORGANIZATION REPORT NUMBER
AFOSR-TR· 9 5 - 0 3 8 2

9. SPONSORING/MONITORING AGENCY NAME(S) AND ADDRESS(ES)
AFOSR/NM
110 Duncan Ave., Suite B115
Bolling AFB DC 20332-0001

10. SPONSORING/MONITORING AGENCY REPORT NUMBER
F49620- 92-J-0097

11. SUPPLEMENTARY NOTES

19950614 045

12a. DISTRIBUTION/AVAILABILITY STATEMENT

Approved for public release;
distribution unlimited.

13. ABSTRACT (Maximum 200 words)

The stability and development of unsteady separation on airfoil leading edges has been investigated. In particular, attention was focused on investigations of 2D unsteady incompressible flow past a parabola at angle of attack which models the leading edge of many airfoils. This study has direct application to leading edge stall (LES) and thin airfoil stall as well as unsteady flow past leading edges. The general character of much of this study allows for application to other classes of unsteady boundary layer flow.

DTIC QUALITY INSPECTED 3

14. SUBJECT TERMS
Boundary layer stability, unsteady flow, high Reynolds number flow

15. NUMBER OF PAGES
96

16. PRICE CODE

17. SECURITY CLASSIFICATION OF REPORT	18. SECURITY CLASSIFICATION OF THIS PAGE	19. SECURITY CLASSIFICATION OF ABSTRACT	20. LIMITATION OF ABSTRACT
Unclassified	Unclassified	Unclassified	UL

Nonlinear Stability of Unsteady Viscous Flow, Final Technical Report, A.P. Rothmayer

The stability and development of unsteady separation on airfoil leading edges has been investigated. In particular, attention was focused on investigations of 2D unsteady incompressible flow past a parabola at angle of attack which models the leading edge of many airfoils. This study has direct application to leading edge stall (LES) and thin airfoil stall as well as unsteady flow past leading edges. The general character of much of this study allows for application to other classes of unsteady boundary layer flow. The accomplishments are detailed below.

1.0 Investigations of Boundary Layer Approaches:

A number of issues were examined related to unsteady leading edge separation solved using the classical boundary layer approximation at high Reynolds numbers (see Fig. 1), the equations being:

$$u_x + v_Y = 0$$

and

$$u_t + uu_x + vu_Y = Ue_t + UeUe_x + u_{YY},$$

where Ue is the inviscid slip velocity at the solid surface, which in general is a function of time and position along the solid surface and is specified for the problem in question. The boundary conditions are

$$u(x, 0, t) = v(x, 0, t) = 0$$

and

$$u(x, Y, t) \rightarrow U_e(x, t) \quad \text{as} \quad Y \rightarrow \infty \quad .$$

For the parabola at angle of attack the inviscid solution is

$$U_e(x, t) = \frac{y(x) + K(t)}{\sqrt{y(x)^2 + 1}}$$

and y(s) is given by

$$x = \frac{1}{2}\left[y \sqrt{y^2 + 1} + \ln\left(y + \sqrt{y^2 + 1}\right) \right] \quad .$$

The angle of attack parameter, K(t), measures the height of the stagnation point below the horizontal axis, and may be related to the physical angle of attack in thin airfoil theory when the parabola is the leading edge correction for flow past a thin airfoil. The K(t) is arbitrary. For the case of uniform pitch−up, K(t) has been chosen as

$$K(t) = \frac{a}{2}\left[t + \frac{1}{b}\ln\frac{\cosh(bt + c)}{\cosh(c)} \right] \quad ,$$

where, a, b and c are constants and a is the ultimate slope of the $K(t)$ curve (see Fig. 2).

a.) The existence of boundary layer instability modes for flow past a pitching parabola at angle of attack was verified by local stability analysis (i.e. Orr−Sommerfeld analysis applied to the boundary layer equations) (see Figs. 3 and 4). Modeshapes and growth rates were successfully compared with the asymptotic theory of Cowley, Hocking & Tutty (1985), CHT, (see Figs. 4 and 5). The stability equations were developed from a linear perturbation about a known solution of the classical boundary layer equations, (u_0, v_0). The perturbation takes the form

$$(u, v) \sim (u_0, v_0) + \varepsilon(u_1, v_1) + \dots \quad , \quad \varepsilon \ll 1 \quad ,$$

which gives the perturbation equations

$$u_{1x} + v_{1Y} = 0$$

and

$$u_{1t} + u_0 u_{1x} + u_1 u_{0x} + v_0 u_{1Y} + v_1 u_{0Y} = u_{1YY} \quad .$$

These equations are nonparallel and have a disturbance growth evolving on the time scale of the original boundary layer. To examine high frequency instabilities, we made a partially parallel flow approximation:

$$(u_1, v_1) = e^{i\alpha}(u', v') \quad ,$$

which gives the equations:

$$i\alpha u' + v'_Y = 0$$

$$u'_t + i\alpha u_0 u'_x + u' u_{0x} + v_0 u'_Y + v' u_{0Y} = u'_{YY} \quad .$$

The boundary conditions are:

$$u'(x, 0, t) = v'(x, 0, t) = 0 \quad .$$

and

$$u'(x, \infty, t) \to 0 \quad .$$

This system was solved as a time marching problem with central differences in Y. The growth rates and mode shapes were computed numerically from the long−time solutions. The above equations are a non−asymptotic high frequency, short wavelength, version of the Cowley *et al* (1985) work. The actual asymptotic structure of the high frequency instability is a bit more complicated than this. Any high frequency instability which has streamwise wavelength α^{-1} will be inviscid at leading order, and neutral for the classical boundary layer. The CHT instability is driven by viscous effects which re−enter through a viscous critical layer centered at the minimum velocity point in an unsteady separation or maximum in a jet (see Fig. 3).

These instabilities should render the unsteady boundary layer equations ill−posed in time due

to the fact that the instabilities at zero wavelength have unbounded growth rates. However, the instabilities do have low growth rates, and so a smooth enough boundary layer solution which evolves more rapidly than the slow growth of the instabilities should be computable.

b.) Joint work with F.T. Smith concluded that the above CHT instability could be connected to marginal separation in a limit as initial separation was approached. That is, the unstable modes with infinite growth rate at zero wavelength continued to exist until the point of first separation (with the scaled growth rates tending to zero in a limit as the first separation point was approached).

c.) In the early computations, grid−grid numerical oscillations were encountered whose modeshapes (see Figs. 6 and 7), growth rates and overall qualitative/quantitative properties coincided quite well with those of the linear boundary layer instability computed above.

d.) The boundary layer oscillations were later removed in the full parabola at angle of attack computations by an appropriate choice of numerical scheme, which was a Crank−Nicholson method with the farfield conditions removed to true infinity (see Fig. 8). We believe that sufficient smoothing of the scheme and boundary conditions removed the oscillations.

The current boundary layer equations were solved in streamfunction−velocity form with stretching transformations in the streamwise and normal directions:

$$s = s_{max} \frac{\sinh(a\bar{s})}{\sinh(a)} \qquad -1 \leqq \bar{s} \leqq 1 \quad , \quad -s_{max} \leqq s \leqq s_{max}$$

$$N = N_{max} \frac{\sinh(b\bar{N})}{\sinh(b)} \qquad 0 \leqq \bar{N} \leqq 1 \quad , \quad 0 \leqq N \leqq N_{max} \ .$$

The boundary layer equations are given by

$$u - \bar{N}_N \psi_{\bar{N}} = 0$$

and

$$u_t + \bar{s}_s u u_{\bar{s}} - \bar{s}_s \bar{N}_N \psi_{\bar{s}} u_{\bar{N}} = U e_t + U e U e_s + \bar{N}_{NN} u_{\bar{N}} + \bar{N}_N^2 u_{\bar{N}\bar{N}} \ .$$

These equations were solved with a second order backward temporal difference and central differences on all other terms including the streamwise convective terms. The method is globally iterated to convergence at each time level with each alternate sweep being in opposite directions to accelerate convergence.

e.) The discrepancy between the above two results, i.e. the fact that an Orr−Sommerfeld linear stability analysis of the smooth boundary layer solution clearly indicated that instability modes should be present and would be dominated by the shortest wavelength modes, whereas the numerical computations seemed to indicate that they could be removed, led us to examine extensions into the nonlinear regime of the linear asymptotic CHT boundary layer instability

theory.

The nonlinear critical layer is structured as follows.

The nonlinear structure corresponding to the linear work of Cowley *et al* (1985) is found, after some trial and error, to occur when the disturbance within the critical layer (see Fig. 3) rise to the level of the locally small parabolic contribution of the mean flow. In the critical layer, it is nominally expected that:

$$u \sim U_0(y) + \varepsilon U + ... \sim U_0(y_c) + (y - y_c)U_{0_y}(y_c) + \frac{(y - y_c)^2}{2}U_{0_{yy}}(y_c) + ... + \varepsilon U + ...$$

For simplicity the following variables were defined:

$$U_{0c} = U_0(y_c) \qquad U'_{0c} = U_{0_y}(y_c) \qquad U''_{0c} = U_{0_{yy}}(y_c) \quad .$$

The critical layer is placed at a velocity minimum or maximum and so it was assumed that

$$U'_{0c} = U_{0_y}(y_c) = 0$$

To preserve the connection with linear theory, the critical layer thickness was taken to be the Cowley *et al* (1985) value:

$$y = y_c + \alpha^{-1/4}Y \ , \qquad \alpha \gg 1 \ .$$

With these assumptions, the streamwise velocity expansion becomes

$$u \sim U_0(y) + \varepsilon U + ... \sim U_{0c} + \frac{\alpha^{-1/2}Y^2}{2}U''_{0c} + ... + \varepsilon U + ... \quad .$$

Therefore the perturbation within the critical layer becomes comparable to the dominant parabolic portion of the mean flow which drives the linear boundary layer instability when the perturbation rises to the still small value $\varepsilon = \alpha^{-1/2}$. This may be shown to generate a vertical velocity of $O(\alpha^{1/4})$ within the critical layer which provides the displacement driving the main linearized boundary layer flow. Pressure displacement interaction is negligible provided the wavelengths of the disturbances are sufficiently long.

In the main boundary layer flow y is $O(1)$ and the streamwise length scale is taken to be a small specified value (see Region I of Fig. 3):

$$\frac{\partial}{\partial x} = \alpha\frac{\partial}{\partial X} \quad .$$

Consistency within the critical layer requires that the disturbance be approximately convected with the flow velocity (as is the case in the linear CHT mode) and so

$$\frac{\partial}{\partial t} = -\alpha c_0\frac{\partial}{\partial X} + \alpha^{1/2}\frac{\partial}{\partial T} \quad .$$

The first term is the local convection with the flow velocity, where c_0 is the wavespeed, which

is the velocity at the reversed flow minimum

$$c_0 = U_{0_c} = U_0(y_c) \ .$$

The second term is determined by bringing unsteady effects into play within the critical layer. The outer flow is then forced by the displacement effect from the critical layer and is found to have the expansions:

$$u \sim \overline{U_0(y)} + \alpha^{-1/4}u_1 + \alpha^{-1/2}u_2 + \alpha^{-3/4}u_3 + \ldots$$

and

$$v \sim \alpha^{3/4}v_1 + \alpha^{1/2}v_2 + \alpha^{1/4}v_3 + \ldots \ .$$

Three orders of magnitude are required to reproduce the linear results presented in Cowley *et al* (1985). In addition, the critical layer has algebraic decay in the matching with the main boundary layer and the higher order terms are useful for numerically imposing that matching boundary condition. Substitution into the unsteady boundary layer equations,

$$u_x + v_y = 0$$

and

$$u_t + uu_x + vu_y = -p_x(x,t) + u_{yy}$$

gives the continuity equations

$$u_{iX} + v_{i\,y} = 0 \qquad\qquad i=1,2,3$$

and the momentum equations

$$(U_0(y) - c_0)u_{1X} + U_0'(y)v_{1\,y} = 0$$

$$(U_0(y) - c_0)u_{2X} + U_0'(y)v_{2\,y} = -u_1u_{1X} - v_1u_{1y}$$

$$(U_0(y) - c_0)u_{3X} + U_0'(y)v_{3\,y} = -u_{1T} - u_1u_{2X} - u_2u_{1X} - v_1u_{2y} - v_2u_{1y} \ .$$

These equations were integrated to give the expansions in the main boundary layer

$$u \sim U_0(y) + \alpha^{-1/4}A(X,T)U_0'(y) + \alpha^{-1/2}\left[B(X,T)U_0'(y) + \frac{1}{2}A^2U_0''(y)\right]$$

$$+ \alpha^{-3/4}\left[C(X,T)U_0'(y) + ABU_0''(y) + \frac{1}{6}A^3U_0'''(y)\right] + \ldots$$

$$v \sim - \alpha^{3/4} A_X \big(U_0(y) - c_0\big) - \alpha^{1/2}\Big[B_X\big(U_0(y) - c_0\big) + AA_X U_0'(y)\Big]$$

$$- \alpha^{1/4}\Big[A_X\big(U_0(y) - c_0\big) + A_T + (AB)_X U_0'(y) + \tfrac{1}{6}(A^3)_X U_0''(y)\Big] + \dots \; ,$$

where $A=A(X,T)$, $B=B(X,T)$, and $C=C(X,T)$ are unknown displacement functions. Notice that the smallest term entering into the momentum equation in the first three orders is $O(\alpha^{1/4})$ which is larger than any $O(1)$ effect coming in from variations in the mean flow. Also notice that the leading order v−velocity is set by matching with the critical layer, but the rest of the terms are forced by nonlinear interactions in the momentum equation (i.e. the power series expansion is set once the leading order v−velocity is known).

The scales of the nonlinear critical layer are set by a viscous balance and by assuming that the perturbations to the main boundary layer flow enters at the same order of magnitude as the parabolic mean flow. It turns out that long scale variations from the main boundary layer flow also enter this balance at the same order of magnitude. Therefore, two sets of scales are operating in the boundary layer, one on the scale of the local perturbation and the other on the scale of the main boundary layer:

$$\frac{\partial}{\partial x} = \alpha \frac{\partial}{\partial X} + \frac{\partial}{\partial x_0}$$

$$\frac{\partial}{\partial t} = - \alpha c_0 \frac{\partial}{\partial X} + \alpha^{1/2} \frac{\partial}{\partial T} + \frac{\partial}{\partial t_0} \; .$$

The vertical scale of the critical layer is determined by a convective−viscous balance and is found to be:

$$\frac{\partial}{\partial y} = \alpha^{1/4} \frac{\partial}{\partial Y} + \frac{\partial}{\partial y_0} \; .$$

The perturbations to the original boundary layer flow are on the local scales (X,Y,T), whereas the original boundary layer flow is a known function of the longer scales (x_0, y_0, t_0), i.e. $U_0 = U_0(x_0, y_0, t_0)$. The expansions in the critical layer are found to be:

$$u \sim U_{0c}(x_0, y_c, t_0) + \alpha^{-1/2}\Big[\frac{Y^2}{2} U_{0\,y_0 y_0}(x_0, y_c, t_0) + U(X, Y, T)\Big] + \alpha^{-3/4}U_2 + \alpha^{-1}U_3 + \dots$$

and

$$v \sim \alpha^{1/4}V(X, Y, T) + V_2 + \alpha^{-1/4}V_3 + \dots \; .$$

The higher order terms drop from the equations, and are set from matching with the main boundary layer. Substitution into the mass conservation equation gives:

$$U_X + V_Y = 0$$

The momentum equation yields the following equations for the first three terms in the expan-

sion:

$$(U_0(x_0, y_c, t_0) - c_0)U_X = 0$$

$$(U_0(x_0, y_c, t_0) - c_0)U_{2X} = 0$$

$$(U_0(x_0, y_c, t_0) - c_0)U_{3X} + \overline{U_T} + \left[\frac{Y^2}{2}U_{0y_0y_0}(x_0, y_c, t_0) + U\right]U_X + YU_{0y_0y_0}(x_0, y_c, t_0)V$$

$$+ VU_Y = U_{YY} - p_{0x}(x, t) + U_{0y_0y_0} - U_{0\,t_0} - U_0U_{0x_0} \quad .$$

It is assumed that the critical layer lies at a local minimum or maximum in the velocity profile and so

$$U'_{0c} = U_{0y_0}(x_0, y_c, t_0) = 0$$

Furthermore, the disturbance is convected with the local flow velocity in the critical layer which implies that

$$c_0 = U_0(x_0, y_c, t_0) \quad .$$

At the critical layer, the original boundary layer satisfies the momentum equation

$$U_{0\,t_0} + U_0U_{0x_0} = -p_{0x}(x, t) + U_{0y_0y_0} \quad .$$

Therefore, the first two equations from the momentum equation are identically satisfied and the third momentum equation becomes, essentially, a classical unsteady boundary layer problem:

$$U_T + \left[\frac{Y^2}{2}U''_{0c} + U\right]U_X + YU''_{0c}V + VU_Y = U_{YY}$$

where

$$U''_{0c} = U_{0y_0y_0}(x_0, y_c, t_0)$$

is a known constant. Matching the critical layer with the main boundary layer gives

$$U(X, Y, T) \to YAU''_{0c} + \frac{A^2}{2}U''_{0c} \qquad \text{as } Y \to \infty$$

and

$$V(X, Y, T) \to -\left[\frac{Y^2}{2} + AY + \frac{1}{2}A^2\right]A_XU''_{0c} - A_T \quad \text{as } Y \to \infty \quad .$$

Within the critical layer, the streamfunction is

$$\psi \sim \alpha^{-1/4} U_{0c} Y + \alpha^{-3/4}\left[\frac{Y^3}{6} U_{0c}'' + \Psi\right] + \dots$$

where

$$U = \Psi_Y \qquad V = -\Psi_X \; ,$$

and the vorticity is

$$\omega = u_y - v_x \sim \alpha^{5/4}\Omega + \dots$$

where

$$\Omega = -V_X = \Psi_{XX} \; .$$

From the above discussion, the nonlinear critical layer at the point of minimum velocity in the reversed flow region was found to be governed by the following system of equations, obtained after scaling out the various constants:

$$U_X + V_Y = 0$$

and

$$U_T + UU_X + VU_Y = -1 + U_{YY}$$

with the boundary conditions

$$U(X, Y, T) \to \frac{Y^2}{2} + YA + \frac{A^2}{2} \qquad\qquad \text{as } Y \to \infty$$

$$V(X, Y, T) \to -\left[\frac{Y^2}{2} + AY + \frac{1}{2}A^2\right]A_X - A_T \qquad \text{as } Y \to \infty$$

and

$$U(X, Y, T) \to \frac{Y^2}{2} \qquad\qquad \text{as } Y \to -\infty$$

$$V(X, Y, T) \to 0 \qquad\qquad \text{as } Y \to -\infty \; .$$

Numerical computations of the early initiation phase of a boundary layer separation were developed and compared with existing computations. This was done for an inviscid vortex traveling over a plate which induces an unsteady separation in the boundary layer on the plate (see Fig. 9). These computations are representative of current state−of−the−art boundary layer computational methods in the early pre−singularity unsteady separation stage. This numerical method is also the same method used to obtain smooth solutions on the parabola at angle of attack and is the method used by Peridier *et al* (1991) and others to compute the early stages

8

of unsteady laminar boundary layer separation. Wall shears for the vortex convection problem are shown in Fig. 10 and comparisons with Peridier *et al* (1991) are shown in Fig. 11. Numerical computations were attempted for the nonlinear critical layer, described above, using this algorithm (which was a trivial change in the algorithm from the above–mentioned test case). The changes were due to the coupling algorithm for the farfield boundary conditions. The finite difference equations are:

$$\frac{1}{X_{\xi_{i-1/2}}}\left[\frac{U_{X_{i-1/2,j}}^{n+1} + U_{X_{i-1/2,j-1}}^{n+1}}{2}\right] + \frac{V_{i,j}^{n+1} - V_{i,j-1}^{n+1}}{2\Delta Y} + \frac{V_{i-1,j}^{n+1} - V_{i-1,j-1}^{n+1}}{2\Delta Y} = 0 \quad,$$

where the streamwise derivatives are central differenced about $i-1/2$. The momentum equation is central differenced about $n+1/2,j$ after substitution of the mass equation for the streamwise convective term:

$$\frac{U_{i,j}^{n+1} - U_{i,j}^{n}}{\Delta T} - \left[\frac{U^{n+1} + U^n}{2}\right]\left[\frac{V_Y^{n+1} + Y_Y^n}{2}\right] -$$

$$+ \left[\frac{V^{n+1} + V^n}{2}\right]\left[\frac{U_Y^{n+1} + U_Y^n}{2}\right] = -1 + \frac{U_{YY}^{n+1} + U_{YY}^n}{2} \quad.$$

The resulting equation is Newton linearized and coupled to the mass equation using a block tri–diagonal algorithm. The lower boundary conditions are

$$U_{i,1}^{n+1} = \frac{Y_1^2}{2}$$

and

$$V_{i,1}^{n+1} = 0 \quad.$$

The upper boundary conditions are the mass equation applied at $j=N$ and the central differenced form of the matching conditions. The v–matching condition is

$$V_{i,N-1/2}^{n+1/2} \rightarrow \frac{U_{i,N-1/2}^{n+1/2} V_{Y_{i,N-1/2}}^{n+1/2}}{Y_{N-1/2} + A_i^{n+1/2}} - \frac{A_i^{n+1} - A_i^n}{\Delta T} \quad.$$

This equation is Newton linearized and central differenced about the $N-1/2$ gridpoint, which is taken at a large value of Y. The u–matching condition gives

$$U_{i,N}^{n+1} \rightarrow \frac{Y_N^2}{2} + Y_N A_i^{n+1} + A_i^{n+1} A_i^{n+1g} - \frac{\left(A_i^{n+1g}\right)^2}{2} \quad.$$

where g denotes guessed values from the Newton linearization which are iterated to convergence at each time level. The boundary condition is implemented in the quasi–simultaneous manner of Davis & Werle (1985). Following Davis & Werle (1985), the displacement function computed from the first equation (i.e. A_i^{n+1}) is substituted into the second equation, giving

9

a single boundary condition expressed only in terms of variables contained within the critical layer equations. After the boundary layer equations are inverted at a particular i location the displacement function is post–calculated from:

$$A_i^{n+1} = \frac{1}{Y_N + A_i^{n+1}} \left[U_{i,N}^{n+1} - \frac{Y_N^2}{2} + \frac{\left(A_i^{n+1}\right)^2}{2} \right]$$

The method is converged at each time level by repeatedly sweeping the grid in X from a fixed upstream location to a fixed downstream location. The method is converged to a local absolute error on the displacement function and all velocities at all points on the grid. Stretching is used in the streamwise direction to isolate disturbances near the origin which are input as initial conditions which satisfy mass conservation.

The results were inconclusive. Exponential growth was observed at low to moderate amplitude (see Figs. 12 through 15), but eventually point–point oscillations occurred with no clear way to remove them. Large amplitude limits could be constructed, but without a numerical solution to connect the linear instabilities to the large amplitude limit we did not feel that we could justify the limit solution. Over–clustering the grid at earlier times showed that these point–point oscillations could be moved forward in time. This was done using stretchings comparable to those used in the parabola at angle of attack problem and the vortex–over–a–plate problem. Our feeling at this point is that there is a problem with the boundary layer equations, which can be made to go away if the numerical method and initial/boundary conditions are sufficiently smooth (and the above critical layer is under–resolved), but can re–occur if the grid spacing is made small enough.

The results of this part of the study were inconclusive due to the fact that we cannot obtain a "grid–independent" verification of the CHT modes. To summarize

1. Non–asymptotic linear stability analysis of the boundary layer equations in regions of flow separation clearly confirmed the existence of boundary layer instability modes. These computations are smooth and regular.

2. Early numerical simulations which appeared smooth to graphical inspection yielded point–point numerical oscillations which were in complete agreement with the CHT theory.

3. The instability encountered in #2 was found to be due to the numerical scheme and boundary conditions. It is believed that the new scheme, which now conforms to current state–of–the art boundary layer solution strategies for early separations, is smoother than our first scheme. The boundary layer instability modes computed from linear stability analysis in #1 are still present.

4. We constructed the nonlinear critical layer to look for nonlinear amplitude modulation and/ or growth continuation. The critical layer was successfully constructed, but the numerical

10

method used in #3 yielded the same problem encountered in #2. It was found that the numerical oscillations were controlled by grid spacing (which was the same conclusion reached in #2). This result is sensible. Our very tentative conclusion is that boundary layer schemes which resolve the critical layer will eventually run into numerical difficulty at sufficiently small grid spacing. This suggestion still needs to be verified.

2.0 Stability Analysis:

Due to the potential difficulties encountered with the boundary layer equations we decided to focus part of our attention on the pre–separation instabilities, and chose the Rayleigh instability as a first candidate for study. Our feeling at this point is that the Rayleigh instability is one of a number of possible dominant flow solutions which may occur depending on the frequency of the laminar flow and the particular flow conditions (The likely candidates right now for 2D are: Tollmien–Schlichting waves, laminar boundary layer with singularity termination to local Euler regions, unsteady marginal separation with singularity termination to local Euler regions, CHT modes – which are likely just the marginal separations, and Rayleigh instabilities). We believe that the Rayleigh instability will dominate the flow near a leading edge separation in two dimensions providing that the unsteady forcing (say change in angle of attack) is not too fast.

a.) We performed a stability analysis for the primary Rayleigh modes in the flow past a pitching parabola at angle of attack, and verified that they do occur prior to boundary layer separation. See Fig. 16 for the neutral stability curve. This was simply a solution of the Rayleigh equation given a boundary layer input profile and is substantially the same as the other Rayleigh stability analyses described later in this report.

It should be noted that the eigensolutions for this primary boundary layer instability do produce eigenvalues which would allow for the secondary instability cascading discussed below (see Fig. 17).

b. It was recognized that a series of cascading secondary instabilities could be constructed at low disturbance amplitude. The first step of a cascade could be constructed where the primary inviscid instability creates a Stokes sublayer. This sublayer becomes unstable to secondary Rayleigh instabilities at a low critical disturbance amplitude.

The classical Rayleigh instability has been shown by Smith & Bodonyi (1985) to occur in a finite aspect ratio region centered within a classical Prandtl boundary layer. Long–wave versions of this instability for triple–decks have been considered by Tutty & Cowley (1986). The scales for the dominant Smith & Bodonyi (1985) instability are (see Fig. 19, Region II):

$$(x, y, t) = (x_0, 0, t_0) + Re^{-1/2}(X, Y, T) \ .$$

Within this region, the streamwise velocity and pressure are $O(1)$ to match with the oncoming boundary layer flow, and the normal velocity is finite to preserve mass conservation:

$$(u, v, p) \sim (U, V, P) + \ldots \quad .$$

The nonlinear instability is governed by Euler equations

$$U_X + V_Y = 0 \quad ,$$

$$U_T \pm UU_X + VU_Y = -P_X$$

and

$$V_T + UV_X + VV_Y = -P_Y \quad ,$$

with tangency conditions at the airfoil surface and the initial conditions being the rotational boundary layer flow. In streamfunction–vorticity form these equations become

$$\Omega = \Psi_{XX} + \Psi_{YY} \quad ,$$

and

$$\frac{\mathfrak{D}\Omega}{\mathfrak{D}T} = \Omega_t + \Psi_Y \Omega_X - \Psi_X \Omega_Y = 0 \quad .$$

The linear version of this problem is the classical Rayleigh equation

$$i\alpha(U_0(Y) - c)\left[\psi_{YY} - \alpha^2 \psi\right] - i\alpha U_0''(Y)\psi = 0 \quad ,$$

where

$$U_0 = \Psi_0'(Y) \quad ,$$

and linear normal–mode perturbations have been assumed

$$(\Psi, \Omega) \sim (\Psi_0(Y), \Omega_0(Y)) + \varepsilon\left[(\psi(Y), \xi(Y))e^{i\alpha(X - cT)} + \text{c.c.}\right] \quad .$$

In all cases, this equation was solved numerically using a nonlinear Newton iteration method, by treating the complex eigenvalue, c, as an additional unknown, with

$$c_Y = 0 \quad .$$

Non–trivial eigensolutions are enforced by requiring that

$$\psi_Y(0) = 1 \quad .$$

Quasi–linearizing and central differencing of the above equations in the forms indicated allow inversion of the resulting finite–difference system as a set of coupled block tri–diagonal equations. This computation becomes difficult near neutral points due to the logarithmic singularity in the classical Tollmien expansions about the critical layer. The solutions exhibited the standard properties of the linear Rayleigh instability. The growth rate is a local maximum within the Euler region and is stable below some critical wavelength. The disturbance growth rates also become small as the scaled wavelength becomes large, which connects up with the long–wave Rayleigh instability (see Tutty & Cowley (1986) for example). For dynamic stall on the parabola at angle of attack we expect all inflectional profiles to potentially admit Rayleigh instabilities (though this is not a sufficient condition for instability). The unsteady reverse

flow profiles are inflectional. However, boundary layer velocity profiles prior to flow reversal are also inflectional. Examination of the numerical boundary layer solutions shows that the inflection point starts at the wall (as opposed to the flow interior). This at least opens up the possibility that the Rayleigh instabilities could grow out of a Navier−Stokes region near the wall. However, when the flow near the wall is inflectional, the wall shear is non−zero. This means that the velocity profiles in any near wall region will be approximately pure shear profiles, which are stable. What we find instead is that the neutral solution occurs when the inflection point is at a finite scaled height within the boundary layer. The neutral solution is an inviscid neutral mode of the Smith & Bodonyi (1985) structure, i.e. the classical Rayleigh problem, and we find that the neutral curve for the dynamic stall occurs somewhere between the curve of first inflection point creation (which is at the wall) and first unsteady flow reversal.

The inviscid Rayleigh instability does not satisfy viscous no−slip conditions at the wall. Therefore, a viscous sublayer is needed. For low instability amplitude this sublayer will be a Stokes layer (Region III, Fig. 19). Can this Stokes layer be destabilized? The answer is yes. At the critical wave amplitude

$$u \sim U_0(Y) + \varepsilon\left[\hat{u}(Y)e^{i\alpha(X-cT)} + c.c\right]$$

with

$$\varepsilon = Re^{-1/4} \quad,$$

a Stokes layer is generated with

$$(x,y,t) = (x_0,0,t_0) + (Re^{-1/2}X, Re^{-3/4}Y, Re^{-1/2}T)$$

and

$$(u,v,p) \sim (Re^{-1/4}\hat{U}, Re^{-1/2}\hat{V}, Re^{-1/4}\hat{P}) + \ldots \quad,$$

with governing equations

$$\hat{U}_X + \hat{V}_Y = 0$$

and

$$\hat{U}_T = -\hat{P}_X(X,T) + \hat{U}_{YY} \quad.$$

Given the driving disturbance which is the slip velocity of the linear Rayleigh instability at the edge of the Stokes sublayer, the exact solution is

$$\hat{U}_0 = U_0{}'(0)\overline{Y} + \hat{u}(0)\left(1 - e^{-k_+Y}\right)e^{i\alpha(X-cT)} + c.c \quad,$$

where

$$k_+ = \sqrt{\alpha|c|}\, e^{i(Arg(c)/2 - \pi/4 + (0,\pi))}$$

and the + indicates that the complex root with positive real part is chosen. The wave amplitude of $Re^{-1/4}$ is the critical case, since it is the first amplitude at which a Navier−Stokes region can be created within the Stokes layer. This brings nonlinear terms into play, which will allow

13

secondary Rayleigh instabilities in the presence of sufficiently inflectional velocity profiles. The Navier−Stokes region has the scales (see Region IV, Fig. 19):

$$(x, y, t) = (x_0, 0, t_0) + (Re^{-1/2}X_0, 0, 0) + (Re^{-3/4}\overline{X}, Re^{-3/4}\overline{Y}, Re^{-1/2}T)$$

and

$$(u, v, p) \sim (0, 0, Re^{-1/4}P_0) + (Re^{-1/4}\overline{U}, Re^{-1/4}\overline{V}, Re^{-1/2}\overline{P}) + .. \ .$$

The region is governed by the full Navier−Stokes equations:

$$\overline{U}_X + \overline{V}_Y = 0 \quad ,$$

$$\overline{U}_T + \overline{U}\overline{U}_X + \overline{V}\overline{U}_Y = -\overline{P}_X + \overline{U}_{XX} + \overline{U}_{YY}$$

and

$$\overline{V}_T + \overline{U}\overline{V}_X + \overline{V}\overline{V}_Y = -\overline{P}_Y + \overline{V}_{XX} + \overline{V}_{YY} \ .$$

We solved a linear version of the above equations in streamfunction vorticity form, which gives the linear stability, Orr−Sommerfeld, initial value problem:

$$\xi = \psi_{\overline{Y}\overline{Y}} - \alpha^2\psi$$

$$\xi_T + i\alpha\hat{U}_0(\overline{Y}, T)\xi - i\alpha\hat{U}_{0\overline{Y}\overline{Y}}(\overline{Y}, T)\psi = -\alpha^2\xi + \xi_{\overline{Y}\overline{Y}} \ .$$

These equations cannot be solved using normal modes in time, due to the fact that the time scale of the Stokes layer is the same as the Navier−Stokes region and T appears explicitly in the base velocity. This linear problem was solved for a model Rayleigh instability of a form similar to the one given above, but with arbitrarily prescribed growth rates and other constants. The results are shown in Figs. 20 and 21, where the average streamwise velocity is

$$|U|_{ave} = \frac{1}{L_y} \int_0^{L_y} |\psi_{\overline{Y}}(\overline{Y}, \tau)| d\overline{Y} \ , \quad L_y \gg 1 \ .$$

We identified two typical cases. The first was for standing wave instabilities (i.e. zero wavespeed of the original Rayleigh instability) in which the solution in the Stokes layer is simply dragged along with the Rayleigh instability (see Fig. 20). The second case was a traveling wave instability with sufficiently large wavespeed (see Fig. 21). In this case the solution developed local spikes which grew at a faster rate than the main Rayleigh instability. This strongly suggests that secondary instabilities could occur within the Stokes layer, and could develop fast time scales and large amplitudes.

b.) We developed a general theory of cascading linear Rayleigh instabilities emerging from the above structure (see Figs. 18 and 22). We showed that a self−similar discrete scale cascade of instabilities could occur which asymptotes from the boundary layer scale to the viscous dissipation scale in the following order (for linear instabilities):

14

$$\Delta_{n+1} = \mathrm{Re}^{-\sum\limits_{k=1}^{n} 1/2^k} \left\{ \prod_{k=1}^{n} \varepsilon_{n-k}^{-1/2^k} \right\} \Delta_1^{1/2n} \quad .$$

If the disturbance amplitude at each step of the cascade is assumed to be $O(1)$ and it is assumed that the initial instability occurs in a classical boundary layer, then the cascade scales are:

$$\left(\Delta_1, \Delta_2, \Delta_3, \overline{\Delta_4}, ... \right) = \left(\mathrm{Re}^{-1/2}, \mathrm{Re}^{-3/4}, \mathrm{Re}^{-7/8}, \mathrm{Re}^{-15/16}, ... \right)$$

and they converge quickly to the dissipation scale Re^{-1}. Details of this cascade are given as follows.

It is assumed that the primary Rayleigh instability occurs in a region of dimension $(\Delta_1, \delta_1 = \Delta_1)$, where for the classical steady or unsteady Prandtl boundary layer (see Fig. 23)

$$\delta_1 = \Delta_1 = \mathrm{Re}^{-1/2} \quad .$$

Other base flows may be used, for the: natural convection boundary layer $\Delta_1 = \mathrm{Re}^{-1/4}$, triple$-$deck separation $\Delta_1 = \mathrm{Re}^{-5/8}$, Tollmein$-$Schlicting waves $\Delta_1 = \mathrm{Re}^{-5/8}$, for internal flows separation of $O(1)$ streamwise scale $\Delta_1 = \mathrm{Re}^{-2/3}$, etc. The primary instability in this first step of the cascade is governed by the nonlinear Euler equations, written here in stream-function vorticity form

$$\Omega = \Psi_{XX} + \Psi_{YY} \quad ,$$

$$\frac{\mathfrak{D}\Omega}{\mathfrak{D}t} = \Omega_t + U\Omega_X + V\Omega_Y = 0 \quad .$$

For all the Rayleigh stability calculations in this study, a linear stability analysis is performed on this system of equations, in which case

$$(\Psi, \Omega) \sim (\Psi_0(Y), \Omega_0(Y)) + \varepsilon_1 \left[(\psi(Y), \xi(Y)) e^{i\alpha(X - cT)} + \mathrm{c.c.} \right] \quad .$$

Substitution into the above equations gives

$$\psi_{YY} - \alpha^2\psi = \xi$$

and

$$i\alpha(\Psi_0'(Y) - c)\xi - i\alpha\Psi_0'''(Y)\psi = 0 \quad ,$$

which may be combined to give the classical Rayleigh equation

$$i\alpha(U_0(Y) - c)\left[\psi_{YY} - \alpha^2\psi\right] - i\alpha U_0''(Y)\psi = 0 \quad ,$$

15

where

$$U_0 = \Psi_0'(Y) \quad .$$

This equation may be solved using the method described previously.

The inviscid instability of $O(\varepsilon_1)$ has a non−trivial slip velocity at the wall and so a viscous Stokes layer is needed to satisfy viscous no−slip conditions. To be more general in our outlook we assumed that the Rayleigh instability is occurring in a region of dimension $(\Delta_n, \delta_n = \Delta_n)$, where Δ_1 is given above (see Fig. 24). Furthermore, it was assumed that the base velocity and perturbation (i.e. the main Rayleigh instability) are given by

$$u \sim \varepsilon_{n-1} U_n + \varepsilon_n u'_n + \cdots$$

where U_n is the base velocity which is assumed known from a previous Stokes sublayer and u'_n is the perturbation giving rise to the Rayleigh instability in the current step (i.e. the n−step). The time scale of this particular Rayleigh instability is given by

$$-t_n = \frac{\Delta_n}{\varepsilon_{n-1}} \quad .$$

Note that for the classical boundary layer

$$\varepsilon_0 = 1$$

and the base flow in the first step of the cascade is a classical boundary layer velocity profile. For other values of n the base flow is a Stokes layer solution (see Fig. 25). Now consider the behavior of the Rayleigh instability as the scaled y−coordinate approaches the wall. For sufficiently large values of ε_n the expansion will break down in an inviscid region of dimension (see Fig. 24)

$$(x, y) \sim O\left(\Delta_n, \frac{\varepsilon_n}{\varepsilon_{n-1}} \delta_n\right) \quad .$$

We assume, for now, that ε_n is large enough that this region remains inviscid. What we find is that the region is a trivial continuation of the Rayleigh solution that lies in Region II, but acts to switch the role of the base flow and the perturbation. Therefore the slip velocity at the wall is $O(\varepsilon_n)$ and a Stokes layer is created with dimensions

$$(x, y) \sim O\left[\Delta_n, \left(\frac{\Delta_n}{Re\varepsilon_{n-1}}\right)^{1/2}\right] \quad .$$

A new secondary Rayleigh instability can occur within a region of the same streamwise length as the height of the Stokes layer, i.e.

$$(x, y) \sim O\left[\left(\frac{\Delta_n}{Re\varepsilon_{n-1}}\right)^{1/2}, \left(\frac{\Delta_n}{Re\varepsilon_{n-1}}\right)^{1/2}\right]$$

and so

16

$$\Delta_{n+1} = \left(\frac{\Delta_n}{\mathrm{Re}\,\varepsilon_{n-1}}\right)^{1/2},$$

providing that

$$-\left(\frac{\varepsilon_{n-1}}{\mathrm{Re}\,\Delta_n}\right)^{1/2} \ll \varepsilon_n \ll \varepsilon_{n-1} \quad .$$

The lower bound on ε_n is the critical perturbation scale for: the inviscid region collapsing into the Stokes layer (in which case the Stokes layer is driven by contributions from both the base flow and Rayleigh instability), and that the secondary region, Region V, be inviscid. If ε_n is at the lower bound then the secondary instability region is viscous and governed by full Navier–Stokes equations. The upper bound is the requirement that the flow in the primary Rayleigh instability be linear and governed by the classical Rayleigh equation. At any step of the cascade it may be easily shown that the secondary Rayleigh instability problem (i.e. Region V, Fig. 24) is given by the classical Rayleigh equation

$$i\alpha\big(U_0(Y) - c\big)\big[\psi_{YY} - \alpha^2\psi\big] - i\alpha U_0''(Y)\psi = 0 \quad ,$$

with the standard boundary conditions

$$\psi(0) = \psi(\infty) = 0 \quad .$$

The base flow is given by the solution to the boundary layer equations in the first step and by the exact solution to the Stokes layer in all subsequent steps, which is

$$U_0 = u'_n(X_o, 0, T_o)\big(1 - e^{-k_+ Y}\big)e^{i\alpha(X_o - cT_o)} + c.c$$

where

$$k_+ = \sqrt{\alpha|c|}\,e^{i(\mathrm{Arg}(c)/2 - \pi/4 + (0,\pi))}$$

and the $+$ indicates that the complex root with positive real part is chosen, see Fig. 25.

Various properties of the cascade are outlined below. As noted above, bounds on allowable perturbations at each step of the cascade may be found. A lower bound may be set at

$$\varepsilon_{n_{crit}} = \left(\frac{\varepsilon_{n-1}}{\mathrm{Re}\,\Delta_n}\right)^{1/2}$$

and it is assumed that

$$\varepsilon_{n_{crit}} \ll \varepsilon_n \ll \varepsilon_{n-1} \quad .$$

It may be easily shown that if $\varepsilon_n \gg \varepsilon_{n_{crit}}$ then

$$\frac{\varepsilon_n}{\varepsilon_{n-1}} \delta_n \gg \left(\frac{\Delta_n}{Re\varepsilon_{n-1}} \right)^{1/2}$$

which means that the inviscid sublayer (Region III, Fig. 24) lies above the Stokes layer (Region IV, Fig. 24). More importantly, if $\varepsilon_n \gg \varepsilon_{n_{crit}}$ then it may be shown that

$$t_{n+1} \ll t_n$$

which means that the time scales of successive Rayleigh instabilities is decreasing and the instability develops sooner on the shorter length scales which are closer to the wall. Also, if $\varepsilon_n \gg \varepsilon_{n_{crit}}$ then it may be shown that

$$\Delta_{n+1} \ll \Delta_n$$

which means that the instability cascade occurs on successively shorter length scales. Finally, if $\varepsilon_n \gg \varepsilon_{n_{crit}}$ then it may be shown that

$$\varepsilon_{n+1_{crit}} \gg \varepsilon_{n_{crit}}$$

which means that as the length scale of the secondary instability gets smaller it takes a larger disturbance amplitude to trigger the next secondary instability. The recursive expression for the scale of the Rayleigh instability may be iterated to the first Rayleigh instability scale, in which case

$$\Delta_{n+1} = Re^{-\sum_{k=1}^{n} 1/2^k} \left\{ \prod_{k=1}^{n} \varepsilon_{n-k}^{-1/2^k} \right\} \Delta_1^{1/2n} \ .$$

For the Prandtl boundary layer

$$\varepsilon_0 = 1 \qquad \Delta_1 = Re^{-1/2}$$

and so

$$\Delta_{n+1} = Re^{-1/4n - \sum_{k=1}^{n} 1/2^k} \prod_{k=1}^{n-1} \varepsilon_{n-k}^{-1/2^k} \ .$$

In the limit as $n \rightarrow \infty$, the geometric series converges to

$$\sum_{k=1}^{\infty} \frac{1}{2^k} = 1$$

and so

$$\Delta_{n+1} \to \mathrm{Re}^{-1} \prod_{k=1}^{\infty} \varepsilon_{n-k}^{-1/2^k} \qquad \text{as } n \to \infty \ .$$

The right hand side is bounded by the inequality

$$\Delta_{n+1} \to \mathrm{Re}^{-1} \prod_{k=1}^{\infty} \varepsilon_{n-k}^{-1/2^k} \geqslant \mathrm{Re}^{-1} \prod_{k=1}^{\infty} \varepsilon_0^{-1/2^k} = \mathrm{Re}^{-1}\varepsilon_0^{-1} \ .$$

Since $\varepsilon_0 = 1$ this means that for all n

$$\Delta_n \geqslant \mathrm{Re}^{-1} \ .$$

This limit is achieved rather quickly for large amplitude disturbances. For example if the disturbance amplitude at each step of the cascade is assumed to be $O(1)$ then the cascade scales are

$$\left(\Delta_1, \Delta_2, \Delta_3, \Delta_4, ...\right) = \left(\mathrm{Re}^{-1/2}, \mathrm{Re}^{-3/4}, \mathrm{Re}^{-7/8}, \mathrm{Re}^{-15/16}, ...\right)$$

and the scales asymptote quickly to the dissipation scale Re^{-1}. The other bound is easy to see from the individual steps of the cascade. If $\varepsilon_n = \varepsilon_{n_{crit}}$ at each step of the cascade then it may be easily shown that

$$\varepsilon_{n_{crit}} = \mathrm{Re}^{-1/4}$$

for all n. The scales in this case are found to be

$$\Delta_1 = \mathrm{Re}^{-1/2} \ , \quad \Delta_n = \mathrm{Re}^{-3/4}, \text{ for all } n \geq 2 \ .$$

The physical interpretation of this result is simply that the second step of the cascade occurs in a full Navier–Stokes region and so no more cascading is possible. This does form a reasonable upper bound for the scales of the cascade, since the perturbation at each level may be taken just slightly larger than the critical amplitude. This means that a cascade can be found where, at each level, the spatial scale is just slightly smaller than $\mathrm{Re}^{-3/4}$. Therefore, the cascade scales are bounded by

$$\mathrm{Re}^{-1} \ll \Delta_n \ll \mathrm{Re}^{-3/4} \ .$$

At any step of the cascade the secondary Rayleigh instability problem (i.e. Region V, Fig. 24) is given by the classical Rayleigh equation

$$i\alpha_n\left(U_0(Y) - c_n\right)\left[\psi_{YY} - \alpha_n^2\psi\right] - i\alpha_n U_0''(Y)\psi = 0$$

together with the boundary conditions

$$\psi(0) = 0 \quad \psi'(0) = 1 \quad \psi'(\infty) = 0 \ .$$

The baseflow is simply the Stokes layer flow generated by the Rayleigh instability in the previous step in the cascade, which is

$$U_0 = u'_{n-1}(X_o, 0, T_o)\left(1 - e^{-k_+ Y}\right)e^{i\alpha_{n-1}(X_o - c_{n-1}T_o)} + c.c$$

This equation may be written in the form

$$U_0(Y) = Re^{i\theta}\left(1 - e^{-k_+ Y}\right) + c.c \ ,$$

where θ is a parameter that positions the current step of the cascade within the Stokes layer and

$$k_+ = \sqrt{\alpha_{n-1}|c_{n-1}|}\,e^{i(\mathrm{Arg}(c_{n-1})/2 - \pi/4 + (0,\pi))} \ .$$

and the + indicates that the complex root with positive real part is chosen. The subscripts $n-1$ denote values which are known from the Rayleigh solution in the previous cascade step and the subscript n denotes values in the current step. Note that the eigenvalue c in step n is an unknown, whereas the wavelength α in step n is a specified parameter. Solving the above problem directly would consist of solving a very large number of Rayleigh equations coupled through the Stokes layer profiles. At each step, parametric variations in streamwise location within the Stokes layer as well as wavelength would have to be accounted for. It is clear that only 2 or 3 steps could be solved by a direct method. Fortunately, the entire cascade problem can be reduced to an iterative mapping on a reduced Rayleigh problem. The transformation

$$(Y, \psi, \tilde{\alpha}) = \frac{1}{\sqrt{\alpha_{n-1}|c_{n-1}|}}\left(\tilde{Y}, \tilde{\psi}, \alpha\right) \quad \left(c_n, U_0\right) = R\left(\tilde{c}_n, \tilde{U}_0\right)$$

yields the following reduced problem: the Rayleigh equation and boundary conditions are the same as above, but the base velocity is replaced by:

$$\tilde{U}_0(\tilde{Y}) = e^{i\theta}\left(1 - e^{-\tilde{k}_+ \tilde{Y}}\right) + c.c \ ,$$

where

$$\tilde{k}_+ = e^{i(\mathrm{Arg}(c_{n-1})/2 - \pi/4 + (0,\pi))} \ .$$

The only parameter which survives from the initial Rayleigh instability driving the Stokes flow is the argument of the complex wavespeed in the previous step of the cascade. The only other two independent parameters in the problem are α_n and θ, but they do not affect the next step of the cascade. Therefore, the only thing we need to check is whether or not the flow is unstable and then compute $\arg(c_n)$ in the unstable regions. An interesting consequence of this transformation is that the entire secondary instability cascade is completely determined by the argument of the eigenvalue of the primary instability in the original unsteady boundary layer (i.e. by arg(c) computed from the instability of the original boundary layer). A schematic diagram

of the reduced problem is shown in Fig. 26.

The above equations are Newton linearized and finite differenced, which gives

$$\left[\frac{U_0 - c_j^g}{\Delta Y^2}\right]\psi_{j-1} - \left[2\frac{U_0 - c_j^g}{\Delta Y^2} + \alpha^2\left(U_0 - c_j^g\right) + U_0''\right]\psi_j + \left[\frac{U_0 - c_j^g}{\Delta Y^2}\right]\psi_{j+1}$$

$$+ \left[\alpha^2\psi_j^g - \psi_{YY}^g\right]c_j = \left[c_j^g\left(\alpha^2\psi_j^g - \psi_{YY}^g\right)\right]$$

and

$$[-1]c_{j-1} + [1]c_j = 0$$

with the boundary condition y=0 at the wall,

$$\psi_1 = 0$$

and the second order accurate boundary condition $\psi_Y = 0$ at the wall,

$$\psi_2 = \Delta Y$$

The free−stream boundary condition is imposed by considering the solution to Rayleigh's equation in the region where $U_0'' = 0$, this gives the solution $\psi \propto e^{-\alpha Y}$ which means that y satisfies the equation $\psi_Y + \alpha\psi = 0$. This last equation is finite differenced in a second order accurate manner to give the boundary condition:

$$\left[\frac{2}{\Delta Y^2}\right]\psi_{N-1} - \left[2\frac{1 + \alpha\Delta Y}{\Delta Y^2} + \alpha^2\right]\psi_N = 0 \quad .$$

This system of equations is inverted using a complex valued block tri−diagonal algorithm. A good initial guess is needed for this algorithm to converge, due to the fact that there are nonunique solutions to the Rayleigh equation. In general, unstable modes coexist with stable modes and the algorithm has a tendency to lock onto the stable modes. We generate the initial guess either from a previously converged solution or by solving the initial value problem for the Rayleigh equation, written in streamfunction vorticity form

$$\psi_{YY} - \alpha^2\psi = \xi$$

and

$$\xi_T + i\alpha\Psi_0'(Y)\xi - i\alpha\Psi_0'''(Y)\psi = 0 \quad ,$$

with boundary conditions that mimic a fixed wall roughness:

$$\psi(0, T) = 1 \quad .$$

These equations are marched long enough in time so that the instability modeshape is fully developed. The solution of this initial value problem is only needed for the very first computation. Subsequent eigenvalue computations use initial guesses from the previously computed eigensolution.

Since the only parameter from the $n-1$ step driving the n'th step of the cascade is arg(c) from the $n-1$ step, self similar solutions occur at fixed points where the arg(c) computed at the n step is equal to the arg(c) input as a parameter from the $n-1$ step (see Fig. 26). The full reduced problem was solved near a region where self−similar solutions (i.e. fixed points) were observed possible (see Figs. 27 and 28). Self similar solutions of this scale cascade were computed and are shown in Figs. 29 and 30. Fig. 27 shows fixed wavelength slices through the unstable region. Fig. 29 shows one of those slices with contours of the $n-$step arg(c) and the fixed point surface indicated. Fig. 30 shows the function arg(c) along the cuts $1-5$ indicated in Fig. 29. The passage from one step of the cascade to the next occurs by specifying arg(c) in the $n-1$ step and using it to generate arg(c) in the n step. The new arg(c) then becomes the input arg(c) at $n-1$ for the next step of the cascade and so an iterative map is generated. The cascade solutions shown in Fig. 30 assume that the instabilities in the various steps of the cascade have the same scaled wavelength (i.e. relative to the Reynolds number scaling). Furthermore, it was found that the instabilities with maximum growth rate at each step of the cascade could also form self−similar cascades to the dissipation scale (see Fig. 28). The essential idea is that any solution with fixed arg(c) and fixed relative position in the Stokes layer, θ, will have a single maximum growth rate at a finite value of wavenumber, α. This means that the waves with maximum growth rate form a surface which is roughly parallel to the (arg(c),θ) plane. If that surface intersects the the fixed point surface in such a way that contours of arg(c) cut across the fixed point line (i.e. the intersection of the two surfaces) then solutions in the maximum growth rate surface look similar to Fig. 29 and cascading solutions can be found. Fig. 28 shows that the maximum growth rate surface, mg, does indeed intersect the fixed point surface, fp. Similar scale cascades are likely for other boundary layer instabilities. The one which dominates is likely to depend on the particular solution considered. The present Rayleigh instability cascade will likely occur for loaded airfoils approaching leading edge separation and lower frequency problems near separation.

It is clear that the present instability, if continued to the viscous dissipation scale, will yield a fractal structure in the streamwise direction at infinite Reynolds number.

3.0 Local Numerical Computations:

The local nonlinear problems for Rayleigh instabilities in the boundary layer, or any step of the cascade, are governed by Euler equations written in local Cartesian coordinates:

22

$$U_X + V_Y = 0 \quad ,$$

$$U_T + UU_X + VU_Y = -P_X$$

and

$$V_T + UV_X + VV_Y = -P_Y \quad .$$

In streamfunction vorticity form these are

$$\Omega = \Psi_{XX} + \Psi_{YY} \, ,$$

$$\frac{\mathcal{D}\Omega}{\mathcal{D}t} = \Omega_t + U\Omega_X + V\Omega_Y = 0 \quad .$$

A model problem to simulate the approach of the above structure to the viscous dissipation scale is the Navier−Stokes problem:

$$\Omega = \Psi_{XX} + \Psi_{YY} \quad ,$$

$$\frac{\mathcal{D}\Omega}{\mathcal{D}t} = \Omega_t + U\Omega_X + V\Omega_Y = Re^{-1}\left(\Omega_{xx} + \Omega_{yy}\right) \quad .$$

A wide variety of numerical methods were employed to compute the local nonlinear development of one step of the cascade. For the sake of conciseness, only the schemes which are currently the most viable will be discussed below. Convective Taylor series expanded, explicit central difference and implicit central difference schemes were used to compute both Euler and Navier−Stokes equations in an attempt to find a two dimensional soliton emerging from the initial linear instability. Local Navier−Stokes solutions at lower Reynolds numbers did show this soliton like behavior (see Figs. 31 through 33)

Three stages were observed in this growth to the soliton candidate. The first was the classical cats−eye pattern with linear growth about the critical layer, the second was a stage with a main nonlinear eddy and multiple smaller eddies and the third was a stage with a single large scale eddy of finite aspect ratio. The creation of asymptotically small scale eddies is believed to be unlikely in the nonlinear inviscid equations which make up each step of the cascade, due to the fact that all functions of vortcity must be conserved in an inviscid flow which tends to mitigate against the development of asymptotically smaller scale structure (note that many, but not all, cases have been ruled out).

First, we note that the full nonlinear coupling in the Euler equations can be preserved for short wavelength regions, with the scalings

$$(X, Y, T) = \delta(X, Y, T) \quad,$$

where δ is the specified small spatial extent of the vortex. The dependent variables must satisfy

$$(\Psi, \Omega) = (\delta\Psi, \delta^{-1}\Omega) \quad.$$

These last conditions are required to preserve $O(1)$ velocities, which seems reasonable since the wall slip velocity and all other velocities within most of the small scale Euler region are likely to be finite. An important conclusion is that the vorticity of the small scale vortex must become locally large in order to preserve a fully rotational flow. Now we turn to the conservation of vorticity. The vorticity equation may easily be manipulated into the following form

$$\frac{\mathfrak{D}F(\Omega)}{\mathfrak{D}t} = (F(\Omega))_t + \Psi_Y(F(\Omega))_X - \Psi_X(F(\Omega))_Y = 0 \ .$$

In vector notation, for a fixed control volume, this equation is equivalent to:

$$\frac{\partial}{\partial t}\int\int\int F(\Omega)\,dV + \int\int F(\Omega)\,\vec{V}\cdot\hat{n}\,dS = 0 \quad,$$

where V is a fixed volume, S is the bounding surface of that volume, $\hat{n}$ is the unit outward normal vector to the surface S and $\vec{V}$ is the velocity $(\Psi_Y, -\Psi_X)$. If we assume that the volume is a periodic box with one surface on the plate, another parallel to the wall, but at large Y, and the period taken to be the prescribed period of the flow, then it may be easily verified that the spatial mean of any function of the vorticity is conserved. Written in the two–dimensional coordinate system this means that

$$\langle F(\Omega)\rangle = \int_{-L/2}^{L/2}\int_{0}^{\infty} F(\Omega)\,dYdX = const \ .$$

We note that periodicity is not likely to play an important role in the final conclusions drawn from the above integral equation. For example, in a "localized" disturbance we could take the edges of the box to be far from the disturbance and arrive at the same result. Such a formulation would allow for complex spatial evolution, but would be difficult to verify computationally. The above result has a simple physical interpretation. Each differentially small patch of fluid has a well defined mean–vorticity attached to it (i.e. approximately equal to the area of the fluid patch multiplied by the magnitude of the local vorticity). In an inviscid flow, the vorticity is convected with the patch of fluid. This means that all vorticity within the flow will be preserved, along with all functions that can be formed from the vorticity (note that incompressibility and two–dimensionality is an important part of this). Particular cases that were examined in the numerical solutions were: conservation of mean vorticity, mean square vorticity, mean quartic vorticity, which gives

$$\langle \Omega^m \rangle = \int\limits_{-L/2}^{L/2} \int\limits_{0}^{\infty} \Omega^m \, dY dX = const$$

for m=1,2,and 4, as well as mean exponential vorticity, which gives

$$\langle \overline{e^{\Omega} - 1} \rangle = \int\limits_{-L/2}^{L/2} \int\limits_{0}^{\infty} \left(e^{\Omega} - 1 \right) dY dX = const \quad .$$

Conservation of even powers of vorticity greater than 2, as well as the exponential vorticity, do not allow for the creation of small scale structures with finite velocity that are governed by the full Euler equations. This is because of the fact that the total integral over such regions would yield values which are much greater than those present in the original flow (which is set be the Stokes sublayer). It is also believed that these conservation laws will play a key role in constructing global nonlinear descriptions of the dynamic stall boundary layer with embedded eddies.

In the numerical computations it is important to maintain both stable, oscillation free, computations as well as conservation of different functions of vorticity which will guarantee that the smaller scale structure will not be created.

When numerical methods used for the Navier–Stokes equations were applied to the Euler equations they could not get past the intermediate nonlinear multiple–eddy stage (note that the Euler computations are at very high Reynolds numbers and are the computations most relevant to the scale cascade and asymptotic theory). The most successful straightforward computations were a central difference method in conservation form. It was found that the central difference schemes could be progressed further and further ahead in time with repeated spatial grid refinement. However, progress was slow and a lot of spatial grid refinement was needed to make even modest gains in time. The finest grids run in our computations were 500 by 500 spatial grids with 20,000 time steps. Central difference schemes were found to conserve vorticity functions well (see Fig. 38), but suffered from spurious oscillations within the middle of the multiple eddy stage. Low order upwind schemes could eliminate the numerical oscillations and pass through the multiple eddy stage to the later stage, but failed the vorticity–function conservation test quite badly at very early times.

One scheme used for the Euler and Navier–Stokes solutions consisted of convecting the vorticity and then Taylor series expanding the convected vorticity back to a fixed grid. This scheme was used for both the inviscid and viscous solutions. It was found that a conservative central difference scheme yielded substantially the same results as the following scheme. Both the convective and central difference scheme are currently being abandoned in favor of the CUD (compact upwind difference) scheme to be discussed later. The three schemes are outlined here for the Euler equations.

For the Euler equations, a velocity field is calculated at the $n-1$ time step by central differenc-

ing the streamfunction. The points on the Eulerian grid are convected with the flow via an explicit time difference:

$$\Delta \hat{x} = \Psi_Y^{n-1} \Delta T + O(\Delta T^2) \ ,$$

$$\underline{\Delta \hat{y}} = - \Psi_X^{n-1} \Delta T + O(\Delta T^2) \ .$$

The above velocities are evaluated with second order accurate central differences. The above equations can be extended to second order accuracte expressions, which are:

$$\Delta \hat{x} = \Psi_Y^{n-1} \Delta T + \frac{\Delta T^2}{2} \left(\Psi_{YT}^{n-1} + \Psi_Y^{n-1} \Psi_{YX}^{n-1} - \Psi_X^{n-1} \Psi_{YY}^{n-1} \right) + O(\Delta T^3) \ ,$$

and

$$\Delta \hat{y} = - \Psi_X^{n-1} \Delta T - \frac{\Delta T^2}{2} \left(\Psi_{XT}^{n-1} + \Psi_Y^{n-1} \Psi_{XX}^{n-1} - \Psi_X^{n-1} \Psi_{XY}^{n-1} \right) + + O(\Delta T^3) \ .$$

The vorticity of a convected gridpoint is taken to be the same as the original vorticity at the corresponding Eulerian gridpoint

$$\Omega_{\hat{i},\hat{j}}^n = \Omega_{i,j}^{n-1} \ .$$

The vorticity on the Lagrangian grid is then used to generate new values of vorticity on the Eulerian grid via Taylor series expansion, which for the first order scheme is:

$$\Omega_{\hat{i},\hat{j}}^n = \Omega_{i,j}^n + \Delta \hat{x}_{i,j} \Omega_{X_{i,j}} + \Delta \hat{y}_{i,j} \Omega_{Y_{i,j}} + O(\Delta \hat{x}^2, \Delta \hat{y}^2) \ .$$

These equations are combined into the following Poisson−like equation for the vorticity

$$\Omega_{i,j}^{n-1} = \Omega_{i,j}^n + \Delta \hat{x}_{i,j} \frac{\Omega_{i+1,j}^n - \Omega_{i-1,j}^n}{2\Delta X} + \Delta \hat{y}_{i,j} \frac{\Omega_{i,j+1}^n - \Omega_{i,j-1}^n}{2\Delta Y} + \Omega_\tau \ ,$$

where τ is a pseudo−time used to accelerate and/or stabilize the solution within each physical time step. For the second order scheme the above becomes

$$\Omega_{i,j}^{n-1} = \Omega_{i,j}^n + \Delta \hat{x}_{i,j} \frac{\Omega_{i+1,j}^n - \Omega_{i-1,j}^n}{2\Delta X} + \Delta \hat{y}_{i,j} \frac{\Omega_{i,j+1}^n - \Omega_{i,j-1}^n}{2\Delta Y} + \Omega_\tau$$

$$+ \frac{\Delta \hat{x}_{i,j}^2}{2} \frac{\Omega_{i+1,j}^n - 2\Omega_{i,j}^n + \Omega_{i-1,j}^n}{\Delta X^2} + \frac{\Delta \hat{y}_{i,j}^2}{2} \frac{\Omega_{i,j+1}^n - 2\Omega_{i,j}^n - \Omega_{i,j-1}^n}{\Delta Y^2} + \Delta \hat{x}_{i,j} \Delta \hat{y}_{i,j} \Omega_{XY}^n \ .$$

These equations are solved with a Peaceman−Rachford ADI method, and converged in the pseudo−time. The spatial cross−derivative in the second order method is iteratively updated within the ADI method. After the vorticity has been obtained, the central difference form of the streamfunction equation is solved using an ADI method with specified vorticity

26

$$\frac{\Psi^n_{i-1,j} - 2\Psi^n_{i,j} + \Psi^n_{i+1,j}}{\Delta X^2} + \frac{\Psi^n_{i-1,j} - 2\Psi^n_{i,j} + \Psi^n_{i+1,j}}{\Delta Y^2} = \Omega^n_{i,j} + \Psi_\tau \quad .$$

The entire numerical method is formally second order accurate in time space. Higher order accurate temporal schemes were tested, but did not yield significant improvements over the above scheme on fine temporal grids (as is to be expected). It should be noted that this method is equivalent to a central difference strongly implicit method if the velocity evaluations are taken to be implicit and the streamfunction and vorticity equations are coupled.

It should be noted that the above scheme was used to generate early solutions and has been abandoned in favor of central difference and CUD schemes.

A number of central difference schemes were tested. Of those tested, the most successful explicit central difference scheme was found to be

$$\frac{\psi^n_{i-1j} - 2\psi^n_{ij} + \psi^n_{i+1j}}{\Delta x^2} + \frac{\psi^n_{ij-1} - 2\psi^n_{ij} + \psi^n_{ij+1}}{\Delta y^2} = \Omega^n_{ij} + \psi_\tau$$

$$\frac{\Omega^{n+1}_{ij} - \Omega^{n-1}_{ij}}{2\Delta t} + \left(\psi^n_Y \Omega^n\right)_X - \left(\psi^n_X \Omega^n\right)_Y = 0$$

or

$$\frac{\Omega^{n+1}_{ij} - \Omega^{n-1}_{ij}}{2\Delta t} + \frac{\left(\psi^n_Y \Omega^n\right)_{i+1j} - \left(\psi^n_Y \Omega^n\right)_{i-1j}}{2\Delta X} - \frac{\left(\psi^n_Y \Omega^n\right)_{ij+1} - \left(\psi^n_Y \Omega^n\right)_{ij-1}}{2\Delta Y} = 0 \quad .$$

Both of the above schemes, as well as the current CUD scheme, were solved with periodicity conditions of the form

$$\Psi^n_{1,j} = \Psi^n_{N,j}$$

and

$$\Omega^n_{1,j} = \Omega^n_{N,j} \quad .$$

These periodicity conditions did not significantly slow the numerical method. The actual periodicity conditions used in the computations were applied by extending the grid one point on either side and iteratively updating the extended points from the solution on the interior of the grid. The actual conditions used were

$$\Psi^n_{1,j} = \Psi^n_{N-1,j} \qquad \Psi^n_{N+1,j} = \Psi^n_{3,j}$$

and

$$\Omega_{1,j}^n = \Omega_{N-1,j}^n \qquad \Omega_{N+1,j}^n = \Omega_{3,j}^n \quad ,$$

where 1 and N+1 are the added points and N−1 and 3 are on the grid interior. These periodicity conditions were applied to all local schemes, including the CUD−3 scheme discussed below. Some use was also made of fixed extrapolated periodicity conditions of the form (also used as initial guesses on the above)

$$\Psi_{1,j}^n = 2\Psi_{N,j}^{n-1} - \Psi_{N,j}^{n-2} + O(\Delta t^2)$$

$$\Omega_{1,j}^n = 2\Omega_{N,j}^{n-1} - \Omega_{N,j}^{n-2} + O(\Delta t^2)$$

$$\Psi_{N,j}^n = 2\Psi_{1,j}^{n-1} - \Psi_{1,j}^{n-2} + O(\Delta t^2)$$

and

$$\Omega_{N,j}^n = 2\Omega_{1,j}^{n-1} - \Omega_{1,j}^{n-2} + O(\Delta t^2) \quad .$$

However, it was found that this did not significantly enhance the convergence of the method. The limiting factor in overall convergence was, and still is, the solution of the Poisson equation for streamfunction.

Discussion was initiated with the United Technologies Corporation to interact with Professor Andrei Tolstykh of the Russian academy of sciences to learn the CUD methods (Compact Upwind Difference). CUD schemes are high order upwind (i.e. one−sided) differencing schemes that maintain 3−point computational molecules. The third order CUD−3 scheme was successfully applied to the Euler equations and appears capable of passing through to the soliton stage while maintaining reasonably good conservation of vorticity and a minimal amount of spurious oscillations. The implementation of this scheme is not sufficiently far along for results to be presented. However, since it was implemented during the grant period and since it will likely form the core of future work the basics of the scheme will be discussed below. The method presented below is first order accurate in time, and first order accurate in the viscous terms (to be discussed later). Second order temporal and viscous schemes are straightforward modifications of this scheme, but do not retain the natural simplicity given below.

The streamfunction equation is solved using an implicit central difference ADI with pseudo time stepping within the iteration

$$\frac{\psi_{i-1j}^n - 2\psi_{ij}^n + \psi_{i+1j}^n}{\Delta x^2} + \frac{\psi_{ij-1}^n - 2\psi_{ij}^n + \psi_{ij+1}^n}{\Delta y^2} = \Omega_{ij}^n - \psi_\tau \quad .$$

The vorticity transport equation was solved with a spatially 3rd order accurate CUD−3 scheme

$$\Omega_t + (u\Omega)_x + (v\Omega)_y = 0 \quad .$$

This equation is particularly appropriate for testing the CUD schemes, as the schemes are intended to use upwind differencing at high order to model convective terms. To construct the CUD−3 differencing, consider the upwind approximation of a derivative

$$f = \frac{\partial u}{\partial x} \quad .$$

Normally the equation is evaluated at i and a one sided difference of the derivative yields first order accuracy. Third order accuracy is achieved by distributing both the right hand side and the left hand side of the above equation over a tri−diagonal grid using the difference operators

$$A_{x\pm}f_i = \frac{\Delta_{x\pm}u_i}{\Delta x} + O(\Delta x^3) \quad .$$

where the standard upwind operators (taken in x and y directions) are

$$\Delta_{x+} = 0^n_{i+1j} - 0^n_{ij} \quad , \quad \Delta_{x-} = 0^n_{ij} - 0^n_{i-1j}$$

$$\Delta_{y+} = 0^n_{ij+1} - 0^n_{ij} \quad , \quad \Delta_{y-} = 0^n_{ij} - 0^n_{j-1}$$

and the CUD−3 operators are

$$A_{x+} = -\frac{1}{12}0^n_{i-1j} + \frac{8}{12}0^n_{ij} + \frac{5}{12}0^n_{i+1j}$$

$$A_{x-} = \frac{5}{12}0^n_{i-1j} + \frac{8}{12}0^n_{ij} - \frac{1}{12}0^n_{i+1j}$$

$$A_{y+} = -\frac{1}{12}0^n_{ij-1} + \frac{8}{12}0^n_{ij} + \frac{5}{12}0^n_{ij+1}$$

$$A_{y-} = \frac{5}{12}0^n_{ij-1} + \frac{8}{12}0^n_{ij} - \frac{1}{12}0^n_{ij+1} \quad .$$

These operators may be written in terms of a switching parameter s. For example, in the x−direction

$$\Delta_x(s) = \frac{s-1}{2}0^n_{i-1j} - s0^n_{ij} + \frac{1+s}{2}0^n_{i+1j}$$

$$A_x(s) = \frac{2-3s}{12}\Omega^n_{i-1j} + \frac{2}{3}\Omega^n_{ij} + \frac{2+3s}{12}\Omega^n_{i+1j} \ ,$$

where the switching parameter gives

$$s = \begin{cases} -1, \text{ backward difference}, - \text{ operator} \\ \ \ 0, \text{ central difference} \\ +1, \text{ forward difference}, + \text{ operator} \end{cases}$$

The same form holds for the $y-$direction. The forward and backward differences are formally 3rd order accurate, while the central difference is formally 4th order accurate. To enhance stability it is sometimes desirable to smoothly switch the upwind operators between a forward and backward difference. For example, this avoids the situation of a single grid$-$point oscillating from forward to backward difference. This was accomplished by using the smooth switching parameter, given in the x$-$direction by

$$s = - \tanh\left[\frac{S u_i}{1.35S\, \Delta u + |u_i|}\right] \ ,$$

where S is some arbitrary large number (S=20 was used in our computations) and Δu is roughly the velocity half range about u=0 where the smooth switch is applied (that is, when u=Δu the switch is at 0.95). As mentioned before, if s=+1,$-$1 the CUD$-$3 scheme is 3rd order accurate and upwinded. If s=0 the CUD$-$3 scheme is 4th order accurate and central differenced. Other values of s give first order accuracy, but these are confined to thin regions where the velocity is low.

Consider the application of the CUD$-$3 scheme to the vorticity transport equation in two dimensions

$$\Omega_t + (u\Omega)_x + (v\Omega)_y = 0 \ .$$

The first order temporal CUD$-$3 scheme was taken in our computations to be

$$\frac{3\Omega^n_{ij} - 4\Omega^{n-1}_{ij} + \Omega^{n-2}_{ij}}{2\Delta t} + \frac{1}{\Delta x}A_x^{-1}(s)\Delta_x(s)(u\Omega)^n_{ij} + \frac{1}{\Delta y}A_y^{-1}(s)\Delta_y(s)(v\Omega)^n_{ij} = 0 \ .$$

In approximately factored form, this scheme becomes

$$\left[1 + \frac{2\Delta t}{3\Delta x}A_x(s)^{-1}\Delta_x(s)u^n_{ij}\right]\left[1 + \frac{2\Delta t}{3\Delta y}A_y(s)^{-1}\Delta_y(s)v^n_{ij}\right](\Omega)^n_{ij} = \frac{4}{3}\Omega^{n-1}_{ij} - \frac{1}{3}\Omega^{n-2}_{ij} \ .$$

This scheme is formally first order accurate in time, but may easily be extended to second order accuracy by adding a grid function to the right hand side of the equation. The factored scheme is solved in the standard fashion by splitting it into two steps

30

$$\left[1 + \frac{2\Delta t}{3\Delta x} A_x(s)^{-1} \Delta_x(s) u_{ij}^n\right] (Q)_{ij}^n = \frac{4}{3}\Omega_{ij}^{n-1} - \frac{1}{3}\Omega_{ij}^{n-2}$$

and

$$\left[1 + \frac{2\Delta t}{3\Delta y} A_y(s)^{-1} \Delta_y(s) v_{ij}^n\right] (\Omega)_{ij}^n = Q_{ij}^n \ .$$

Each step of the CUD−3 algorithm is solved by multiplying through by the appropriate operator, giving:

$$A_x(s)(Q)_{ij}^n + \frac{2\Delta t}{3\Delta x} A_x(s)(uQ)_{ij}^n = A_x(s)\left\{\frac{4}{3}\Omega_{ij}^{n-1} - \frac{1}{3}\Omega_{ij}^{n-2}\right\}$$

and

$$A_y(s)(\Omega)_{ij}^n + \frac{2\Delta t}{3\Delta y} A_y(s)(v\Omega)_{ij}^n = A_y(s)Q_{ij}^n \ .$$

Now consider the actual implementation of each step:

I) x−direction:

$$A_x(s)(Q)_{ij}^n + \frac{2\Delta t}{3\Delta x} A_x(s)(uQ)_{ij}^n = A_x(s)\left\{\frac{4}{3}\Omega_{ij}^{n-1} - \frac{1}{3}\Omega_{ij}^{n-2}\right\}$$

which implies that

$$\frac{2 - 3s}{12} Q_{i-1j}^n + \frac{2}{3} Q_{ij}^n + \frac{2 + 3s}{12} Q_{i+1j}^n + \frac{2\Delta t}{3\Delta x}\left[\frac{s - 1}{2}(uQ)_{i-1j}^n - s(uQ)_{ij}^n\right.$$
$$\left. + \frac{s + 1}{2}(uQ)_{i+1j}^n\right] = A_x(s)\left\{\frac{4}{3}\Omega_{ij}^{n-1} - \frac{1}{3}\Omega_{ij}^{n-2}\right\} \ .$$

A linearization was used in which the u and v velocities were treated as known guessed values (in our problem these equations were iterated with an ADI solution of the Poisson equation for streamfunction). The above gives the tri−diagonal system:

$$\left[\frac{2 - 3s}{12} + \frac{\Delta t(s - 1)}{3\Delta x} u_{i-1j}^n\right]Q_{i-1j}^n + \left[\frac{2}{3} - \frac{2s\Delta t}{3\Delta x} u_{ij}^n\right]Q_{ij}^n$$
$$+ \left[\frac{2 + 3s}{12} + \frac{\Delta t(s + 1)}{3\Delta x} u_{i+1j}^n\right]Q_{i+1j}^n = A_x(s)\left\{\frac{4}{3}\Omega_{ij}^{n-1} - \frac{1}{3}\Omega_{ij}^{n-2}\right\}$$

which must be inverted for Q at all i,j gridpoints. Note that the right hand side is easily computed by applying the A(s) operator to the known vorticity at the old time levels.

<u>II) y−direction:</u>

$$A_y(s)(\Omega)_{ij}^n + \frac{2\Delta t}{3\Delta y}\Delta_y(s)(v\Omega)_{ij}^n = A_y(s)Q_{ij}^n \quad .$$

The above equations imply that

$$\frac{2-3s}{12}\Omega_{ij-1}^n + \frac{2}{3}\Omega_{ij}^n + \frac{2+3s}{12}\Omega_{ij+1}^n + \frac{2\Delta t}{3\Delta y}\left[\frac{s-1}{2}(v\Omega)_{ij-1}^n - s(v\Omega)_{ij}^n\right.$$

$$\left. + \frac{s+1}{2}(v\Omega)_{ij+1}^n\right] = A_y(s)Q_{ij}^n \quad$$

Again, assuming that the v velocities are treated as known guessed values, the above gives the tri−diagonal system:

$$\left[\frac{2-3s}{12} + \frac{\Delta t(s-1)}{3\Delta y}v_{ij-1}^n\right]\Omega_{ij-1}^n + \left[\frac{2}{3} - \frac{2s\Delta t}{3\Delta y}v_{ij}^n\right]\Omega_{ij}^n$$

$$+ \left[\frac{2+3s}{12} + \frac{\Delta t(s+1)}{3\Delta y}v_{ij+1}^n\right]\Omega_{ij+1}^n = A_y(s)Q_{ij}^n$$

which must be inverted for Ω at all i,j gridpoints. Note that the right hand side is again easily computed by applying the $A(s)$ operator to the known values of Q computed during the x−inversion. Also note that the switching operator s is different for the x and y inversions. Care must be taken to consistently apply the appropriate switch and boundary conditions to the above equations.

For example the boundary conditions for the Euler equations are given by flow tangency, or

$$v = -\psi_x = 0$$

The vorticity equation evaluated at y=0 with v=0 is:

$$\Omega_t + u\Omega_x = 0 \quad .$$

This equation may be written in a conservation form which mimics the interior solution:

$$\Omega_t + (u\Omega)_x - \Omega u_x = 0 \quad .$$

The CUD−3 scheme for this equation is

$$\frac{3\Omega_{ij}^n - 4\Omega_{ij}^{n-1} + \Omega_{ij}^{n-2}}{2\Delta t} + \frac{1}{\Delta x}A_x(s)^{-1}\Delta_x(s)(u\Omega)_{ij}^n + \Omega_{ij}^n\frac{1}{\Delta x}\left[A_x(s)^{-1}\Delta_x(s)u_{ij}^n\right] = 0 \quad .$$

This equation may be written in a form similar to the interior equations by multiplying the

equation by 2Dt/3 and carrying terms to be treated as known to the right hand side

$$\Omega_{ij}^n + \frac{2\Delta t}{3\Delta x} A_x(s)^{-1}\Delta_x(s)(u\Omega)_{ij}^n = \frac{4}{3}\Omega_{ij}^{n-1} - \frac{1}{3}\Omega_{ij}^{n-2} - \Omega_{ij}^n\frac{2\Delta t}{3\Delta x}\left[A_x(s)^{-1}\Delta_x(s)u_{ij}^n\right] \quad .$$

Now, a grid function g is defined such that

$$g = A_x(s)^{-1}\Delta_x(s)u_{ij}^n \quad .$$

The grid function g is found by inverting the tri−diagonal equation

$$A_x(s)g = \Delta_x(s)u_{ij}^n$$

or, in expanded form,

$$\frac{2-3s}{12}g_{i-1j}^n + \frac{2}{3}g_{ij}^n + \frac{2+3s}{12}g_{i+1j}^n = \Delta_x(s)u_{ij}^n \quad ;$$

where

$$\Delta_x(s) = \frac{s-1}{2}0_{i-1j}^n - s0_{ij}^n + \frac{1+s}{2}0_{i+1j}^n \quad .$$

The vorticity transport equation at the wall becomes

$$\Omega_{ij}^n + \frac{2\Delta t}{3\Delta x} A_x(s)^{-1}\Delta_x(s)(u\Omega)_{ij}^n = \frac{4}{3}\Omega_{ij}^{n-1} - \frac{1}{3}\Omega_{ij}^{n-2} - \Omega_{ij}^n\frac{2\Delta t}{3\Delta x}\left[g_{ij}^n\right]$$

or

$$A_x(s)\Omega_{ij}^n + \frac{2\Delta t}{3\Delta x}\Delta_x(s)(u\Omega)_{ij}^n = A_x(s)\left\{\frac{4}{3}\Omega_{ij}^{n-1} - \frac{1}{3}\Omega_{ij}^{n-2} - \frac{2\Delta t}{3\Delta x}\Omega_{ij}^n g_{ij}^n\right\} \quad .$$

In expanded form this last equation is

$$\left[\frac{2-3s}{12} + \frac{2\Delta t}{3\Delta x}\frac{s-1}{2}u_{i-1j}^n\right]\Omega_{i-1j}^n + \left[\frac{2}{3} - \frac{2\Delta t}{3\Delta x}su_{ij}^n\right]\Omega_{ij}^n$$

$$+ \left[\frac{2+3s}{12} + \frac{2\Delta t}{3\Delta x}\frac{1+s}{2}u_{i+1j}^n\right]\Omega_{i+1j}^n = A_x(s)\left\{\frac{4}{3}\Omega_{ij}^{n-1} - \frac{1}{3}\Omega_{ij}^{n-2} - \frac{2\Delta t}{3\Delta x}\Omega_{ij}^n g_{ij}^n\right\} \quad .$$

Note that the CUD−3 operator on the right hand side of the equation is simply

$$A_x(s) = \frac{2-3s}{12}0_{i-1j}^n + \frac{2}{3}0_{ij}^n + \frac{2+3s}{12}0_{i+1j}^n \quad .$$

The switching parameter may be the simple switch from backward to forward difference or the more complex smooth switch:

$$s = -\tanh\left[\frac{S u_{ij}}{1.35 S \Delta u + |u_{ij}|}\right] \quad .$$

4.0 Global Numerical Navier–Stokes Computations:

The Navier–Stokes equations in streamfunction vorticity form were solved for flow past a parabola at angle of attack

A series of full Navier–Stokes codes have been written for flow past a parabolic leading edge. The main code used was a pseudo–ADI with central differencing. This algorithm was based on a globally iterated parabolized Navier–Stokes code coupled with an alternating ADI step for the streamfunction and vorticity diffusion (see Davis (1972)). In one version of the code the dependent variables in the Navier–Stokes equations were split into an inviscid and a correction such that the sum of the two yielded the correct viscous variables. The nonlinear "perturbation" equations for the corrections were solved by the above–mentioned method. Details of the various codes and solutions are given below.

The Navier–Stokes equations written in Cartesian coordinates and non–dimensionalized with the leading edge radius of curvature of the parabola are given by

$$-\Omega = \Psi_{xx} + \Psi_{yy}$$

and

$$\Omega_t + \Psi_y \Omega_x - \Psi_x \Omega_y = Re^{-1}(\Omega_{xx} + \Omega_{yy}) \quad .$$

These equations were transformed to parabolic coordinates using

$$x = \frac{\xi^2 - \eta^2}{2} \qquad y = \xi\eta$$

which gives the equations

$$-\left(\xi^2 + \eta^2\right)\Omega = \Psi_{\xi\xi} + \Psi_{\eta\eta}$$

and

$$\left(\xi^2 + \eta^2\right)\Omega_t + \Psi_\eta \Omega_\xi - \Psi_\xi \Omega_\eta = Re^{-1}\left(\Omega_{\xi\xi} + \Omega_{\eta\eta}\right) \quad .$$

The boundary conditions are no–slip at the parabola surface

$$\Psi(\xi, 1, t) = \Psi_\eta(\xi, 1, t) = 0$$

and an asymptote to the free–stream

$$\Psi(\xi, \eta_{max}, t) = \Psi_{inv}(\xi, \eta, t)$$

34

and

$$\Omega(\xi, \eta_{max}, t) = \Omega_{inv}(\xi, \eta, t) \quad .$$

The inviscid flow is given by

$$\Psi_{inv}(\xi, \eta, t) = (\xi + K(t))(\eta - 1)$$

and

$$\Omega_{inv}(\xi, \eta, t) = 0 \quad ,$$

where $K(t)$ is the angle of attack parameter discussed in the boundary layer solution. The following grid stretchings were added to cluster points in the boundary layer and in the streamwise directions near regions of interest

$$\overline{\xi} = \overline{\xi}(\xi) \qquad \overline{\eta} = \overline{\eta}(\eta) \quad .$$

Using these transformations, the Navier–Stokes equations become

$$- \left(\xi^2 + \eta^2\right)\Omega = \overline{\xi}_\xi\left(\overline{\xi}_\xi \Psi_{\overline{\xi}}\right)_{\overline{\xi}} + \overline{\eta}_\eta\left(\overline{\eta}_\eta \Psi_{\overline{\eta}}\right)_{\overline{\eta}}$$

and

$$\left(\xi^2 + \eta^2\right)\Omega_t + \overline{\xi}_\xi\overline{\eta}_\eta\left[\Psi_{\overline{\eta}}\Omega_{\overline{\xi}} - \Psi_{\overline{\xi}}\Omega_{\overline{\eta}}\right] = Re^{-1}\left(\overline{\xi}_\xi\left(\overline{\xi}_\xi\Omega_{\overline{\xi}}\right)_{\overline{\xi}} + \overline{\eta}_\eta\left(\overline{\eta}_\eta\Omega_{\overline{\eta}}\right)_{\overline{\eta}}\right) .$$

The stretching in the normal direction to the parabola is used to resolve the boundary layer and sublayers and is given by

$$\frac{\eta - 1}{\eta_{max} - 1} = \frac{\sinh(a_n\overline{\eta})}{\sinh(a_n)} \quad . \qquad \begin{array}{l} 0 \leqq \overline{\eta} \leqq 1 \\ 1 \leqq \eta \leqq \eta_{max} \end{array}$$

To place points near the leading edge, a simple clustering transformation was used

$$\frac{\xi}{\xi_{max}} = \frac{\sinh(a_s\overline{\xi})}{\sinh(a_s)} \quad . \qquad \begin{array}{l} -1 \leqq \overline{\xi} \leqq 1 \\ -\xi_{max} \leqq \xi \leqq \xi_{max} \end{array}$$

The "a" parameters give the degree of stretching in each case. To cluster points in a specific region of interest in the streamwise direction, the grid was split into three regions:

$$
\begin{array}{lll}
\text{Region 1:} & -\xi_{max} \leqq \xi \leqq \xi_1 & -1 \leqq \overline{\xi} \leqq \overline{\xi}_1 \\
\text{Region 2:} & \xi_1 \leqq \xi \leqq \xi_2 & \overline{\xi}_1 \leqq \overline{\xi} \leqq \overline{\xi}_2 \\
\text{Region 3:} & \xi_2 \leqq \xi \leqq \xi_{max} & \overline{\xi}_2 \leqq \overline{\xi} \leqq 1 \quad .
\end{array}
$$

The stretching transformation in Region 1 is:

$$\frac{\xi + \xi_{max}}{\xi_1 + \xi_{max}} = \frac{\sinh\left(a_1\left(1 - \frac{\overline{\overline{\xi}}+1}{\overline{\overline{\xi}}+1}\right)\right)}{\sinh(a_1)} \quad .$$

In Region 2 a uniform grid was used:

$$\xi = \xi_1 + \frac{\overline{\overline{\xi}} - \overline{\overline{\xi}}_1}{\overline{\overline{\xi}}_2 - \overline{\overline{\xi}}_1}(\xi_2 - \xi_1) \quad .$$

In Region 3:

$$\frac{\xi - \xi_2}{\xi_{max} - \xi_2} = \sinh\left[a_3\left(\frac{\overline{\overline{\xi}} - \overline{\overline{\xi}}_2}{1 - \overline{\overline{\xi}}_2}\right)\right] \quad .$$

The a's are chosen so that the streamwise metric is smooth throughout the domain. A typical grid is shown in Fig. 40.

The finite difference scheme is a central difference pseudo−ADI based on global iteration of a parabolized vorticity equation. The first step of the ADI is

$$\Psi_\tau - \left(\xi^2 + \eta^2\right)\Omega^{n+1/2} = \overline{\overline{\xi}}_\xi\left(\overline{\overline{\xi}}_\xi \Psi_{\overline{\overline{\xi}}}^{n+1/2}\right)_{\overline{\overline{\xi}}} + \overline{\eta}_\eta\left(\overline{\eta}_\eta \Psi_{\overline{\eta}}^{n+1/2}\right)_{\overline{\eta}} \quad ,$$

where the first term is a fictitious temporal term added to stabilize the method and is iterated to zero at each real time level. The vorticity transport equation is

$$\left(\xi^2 + \eta^2\right)\frac{\Omega_{ij}^{n+1/2} - \Omega_{ij}^n}{\Delta t/2} + \overline{\overline{\xi}}_\xi\overline{\eta}_\eta\left[\Psi_{\overline{\eta}}^{n+1/2}\Omega_{\overline{\overline{\xi}}}^{n+1/2} - \Psi_{\overline{\overline{\xi}}}^{n+1/2}\Omega_{\overline{\eta}}^{n+1/2}\right]$$

$$= Re^{-1}\left(\overline{\overline{\xi}}_\xi\left(\overline{\overline{\xi}}_\xi\Omega_{\overline{\overline{\xi}}}^n\right)_{\overline{\overline{\xi}}} + \overline{\eta}_\eta\left(\overline{\eta}_\eta\Omega_{\overline{\eta}}^{n+1/2}\right)_{\overline{\eta}}\right) \quad .$$

All solid underlined terms (at the n+1/2 level) were treated implicitly. All dashed underlined terms were assumed known from the n time level. All terms were spatially central differenced. The n+1/2 time level was iterated to convergence using a global iteration procedure in the streamwise direction. That is, the equations were central differenced, Newton−linearized and inverted in the normal direction using a block tri−diagonal algorithm. Repeated sweeps in the streamwise direction were used to converge the n+1/2 time level. The direction of the sweeps were alternated with each pass to enhance information propagation over the upper and lower surfaces of the parabola.

The second step of the ADI method consists of a streamwise inversion of the vorticity equation

$$\left(\xi^2 + \eta^2\right)\frac{\Omega_{ij}^{n+1} - \Omega_{ij}^{n+1/2}}{\Delta t/2} + \overline{\xi}_\xi \overline{\eta}_\eta\left[\Psi_{\overline{\eta}}^{n+1/2}\Omega_{\overline{\xi}}^{n+1/2} - \Psi_{\overline{\xi}}^{n+1/2}\Omega_{\overline{\eta}}^{n+1/2}\right]$$

$$= Re^{-1}\left(\overline{\xi}_\xi\left(\overline{\xi}_\xi\Omega_{\overline{\xi}}^{n+1}\right)_{\overline{\xi}} + \overline{\eta}_\eta\left(\overline{\eta}_\eta\Omega_{\overline{\eta}}^{n+1/2}\right)_{\overline{\eta}}\right).$$

Again, solid underlined terms at the n+1 level are unknown and dashed terms at the n+1/2 level are known. This means that the above equation could be inverted as it stands with a single equation tri−diagonal algorithm applied to each normal grid line. After this is accomplished, the streamfunction is found from

$$\Psi_\tau - \left(\xi^2 + \eta^2\right)\Omega^{n+1} = \overline{\xi}_\xi\left(\overline{\xi}_\xi\Psi_{\overline{\xi}}^{n+1}\right)_{\overline{\xi}} + \overline{\eta}_\eta\left(\overline{\eta}_\eta\Psi_{\overline{\eta}}^{n+1}\right)_{\overline{\eta}}.$$

Again, solid underlined terms are unknown and the fictitious temporal term is iterated to zero at the n+1 time level. The above scheme is formally second order accurate in space and time.

The boundary conditions at downstream infinity on the upper and lower surfaces of the parabola were assumed to be asymptotes to the following Blasius solution

$$\Psi = \xi F(\eta) \qquad \Omega = -\frac{G(\eta)}{\xi}.$$

These equations were used to develop expressions for the various streamwise derivatives appearing in the above equations at the first and last streamwise stations, which are

$$\Psi_\xi = \frac{\Psi}{\xi} \qquad \Omega_\xi = -\frac{\Omega}{\xi}$$

and

$$\Psi_{\xi\xi} = 0 \qquad \Omega_{\xi\xi} = \frac{2\Omega}{\xi^2}.$$

The above Navier−Stokes code has been verified for the symmetric steady case against older well−documented steady symmetric solutions (see Fig. 41)

We have used this code to compute a number cases:

a.) This Navier−Stokes code was used to compute an impulsively started parabola at angle of attack. An initial inviscid flow is used to compute a viscous flow by impulsively applying the no−slip condition at the surface of the parabola. This reproduces results of Reisenthel (1994) (see Figs. 42 and 43). Secondary separation was observed (and will be described below), though we do not believe that this is tied to the instability cascading discussed previously in this report. The impulsive start case is likely to be related to the laminar boundary layer singulari-

ties. It should be noted that we could not obtain grid independence in this particular problem. We believe that this is due to a failure to represent the unsteady Rayleigh layer at the impulsive start−up (i.e. the grid is taken to be fixed). The reason this was done was to keep these particular computations as close as possible to others currently in the literature, which also use a poor initial start−up.

b.) Using this Navier−Stokes code, we have shown that a similar structure occurs in the case of a rapid unsteady pitch−up (see Figs. 44 through 48). The same multiple−eddy structure occurs in the boundary layer (see Figs. 44 and 45). Here, we were able to come close to grid independence (see Figs. 46, 47 and 48). Furthermore, multiple embedded eddies were observed (see Fig. 48)

The Navier−Stokes code used here is slightly modified from the one discussed above. It was found that the free−stream boundary condition could be more effectively imposed on the interior flow if the solution was split into the inviscid part plus a nonlinear perturbation which gives the true viscous solution. That is

$$\overline{\Psi} = \psi + \Psi_{inv}$$

and

$$\Omega = \omega + \Omega_{inv} = \omega$$

since

$$\Omega_{inv} = 0 \ .$$

The original Navier−Stokes equations were

$$-\left(\xi^2 + \eta^2\right)\Omega = \Psi_{\xi\xi} + \Psi_{\eta\eta}$$

and

$$\left(\xi^2 + \eta^2\right)\Omega_t + \Psi_\eta\Omega_\xi - \Psi_\xi\Omega_\eta = Re^{-1}\left(\Omega_{\xi\xi} + \Omega_{\eta\eta}\right) \ .$$

Substituting the above equations for the transformations gives the "perturbation" streamfunction equation

$$-\left(\xi^2 + \eta^2\right)\omega = \psi_{\xi\xi} + \psi_{\eta\eta} \ ,$$

due to the fact that the inviscid solution satisfies the Laplace equation, and the perturbation vorticity transport equation

$$\left(\xi^2 + \eta^2\right)\omega_t + \left(\Psi_{inv_\eta} + \psi_\eta\right)\omega_\xi - \left(\Psi_{inv_\xi} + \psi_\xi\right)\omega_\eta = Re^{-1}\left(\omega_{\xi\xi} + \omega_{\eta\eta}\right) \ .$$

These last two equations for the perturbations were solved in the same manner as the full system. The boundary conditions on these equations become

38

$$\psi(\xi, 1, t) = 0$$

and

$$\psi_\eta(\xi, 1, t) = - \Psi_{inv_\eta}(\xi, 1, t)$$

at the wall, and the asymptote to the free-stream

$$\psi(\xi, \eta_{max}, t) = \omega(\xi, \eta_{max}, t) = 0 \quad .$$

c.) We have also shown that impulsively changing the angle of attach in small increments (which will lead to a sequence of quasi-steady solutions in stable cases) will give rapid multiple eddy breakup in a flow which is immediately post separation. We think that this may be connected either to marginal separations.

d.) Applying the quasi-steady impulsive change in angle of attack in pre-separation cases produces unstable long-lived unsteady flow with multiple eddies (see Fig. 49). The times in these figures are 75 time units which is somewhat longer than the 30 time units in the rapid pitch-up case. A blow-up of the local wall shear near the eddies is shown in Fig. 50 and vorticity contours are shown in Fig. 51. It should be noted that very fine grids were needed to obtain these solutions. A linearized boundary condition was added to the parabola surface to enable us to input surface distortions of small amplitude but arbitrary functional form. The eddy structure is strongly influenced by small changes in surface geometry perturbations (see Fig. 52). Vorticity and streamline patterns in the vicinity of the eddies are shown in Figs. 53 and 54. Note the resemblance of the eddy in Fig. 54 to the earlier computed eddies in the local solution (see Figs. 31 and 34). We believe that these last computations (i.e. impulsive change in angle of attack below separation) are candidates for Rayleigh instabilities. It is clear that we can rule out all separation eddy creation mechanisms, such as marginal separations and boundary layer singularities, due to the fact that the flow remains attached while the initial instability developes. It is not clear at this point what effect of the impulsive change in angle of attack has on the computations. This should be changed to a smooth variation in future computations.

Lastly, a CUD-3 Navier-Stokes algorithm based on the pseudo-ADI parabolized vortcity iteration was written and verified for the steady symmetric solution (Fig. 55) and early stages of the unsteady pitch-up (Fig. 56).

The unsteady CUD-3 Navier-Stokes algorithm uses the stretched equations in parabolic coordinates written in conservation form

$$\frac{\Psi_\tau}{J} - \frac{(\xi^2 + \eta^2)\Omega}{J} = \left[\frac{\overline{\xi}_\xi}{\overline{\eta}_\eta} \Psi_\xi \right]_\xi + \left[\frac{\overline{\eta}_\eta}{\overline{\xi}_\xi} \Psi_\eta \right]_\eta$$

and

$$\frac{\partial}{\partial t}\left(\frac{(\xi^2 + \eta^2)\Omega}{J}\right) + \left(\Psi_{\bar{\eta}}\Omega\right)_{\bar{\xi}} - \left(\Psi_{\bar{\xi}}\Omega\right)_{\bar{\eta}} = Re^{-1}\left[\left[\frac{\bar{\xi}_{\bar{\xi}}}{\bar{\eta}_{\eta}}\Omega_{\bar{\xi}}\right]_{\bar{\xi}} + \left[\frac{\bar{\eta}_{\eta}}{\bar{\xi}_{\bar{\xi}}}\Omega_{\bar{\eta}}\right]_{\bar{\eta}}\right]\ .$$

where

$$J = \bar{\xi}_{\bar{\xi}}\bar{\eta}_{\eta}\ .$$

The CUD-3 algorithm is applied to the above equations in a form similar to the pseudo$-$ADI algorithm discussed above. Nominally, the CUD-3 algorithm is given by:

$$\frac{\partial}{\partial t}\left(\frac{(\xi^2 + \eta^2)\Omega}{J}\right) + \frac{A_{\bar{\xi}}^{-1}\Delta_{\bar{\xi}}}{\Delta\bar{\xi}}\left(\Psi_{\bar{\eta}}\Omega\right) - \frac{A_{\bar{\eta}}^{-1}\Delta_{\bar{\eta}}}{\Delta\bar{\eta}}\left(\Psi_{\bar{\xi}}\Omega\right)$$
$$= Re^{-1}\left(A_{\bar{\xi}}^{-1}\Delta_{\bar{\xi}}\left(\Omega_{ij}^n\right) + A_{\bar{\eta}}^{-1}\Delta_{\bar{\eta}}\left(\Omega_{ij}^n\right)\right)\ ,$$

where the A's and Δ's are the normal CUD-3 operators and upwind operators respectively and the Δ's on the right hand side are central difference operators, given by

$$\Lambda_{\bar{\xi}}\Omega_{ij} = \frac{1}{\Delta\bar{\xi}^2}\left[\lambda_{i+1/2j}\left(\Omega_{i+1j} - \Omega_{ij}\right) - \lambda_{i-1/2j}\left(\Omega_{ij} - \Omega_{i-1j}\right)\right]$$

and

$$\Lambda_{\bar{\eta}}\Omega_{ij} = \frac{1}{\Delta\bar{\eta}^2}\left[\lambda_{ij+1/2}^{-1}\left(\Omega_{ij+1} - \Omega_{ij}\right) - \lambda_{ij-1/2}^{-1}\left(\Omega_{ij} - \Omega_{ij-1}\right)\right]\ ,$$

where

$$\lambda = \frac{\bar{\xi}_{\bar{\xi}}}{\bar{\eta}_{\eta}}\ .$$

The algorithm is implemented in a manner similar to the pseudo$-$ADI algorithm discussed earlier. Since this work has only progressed through the very preliminary stages, further details will be omitted here. The above scheme is second order accurate in time, third order accurate in space in the convective terms and first order accurate in space in the viscous terms (which appears to be a standard accepted limitation of past CUD work). We believe that the CUD schemes will be a major emphasis of future work and attention will be paid to increasing the accuracy of the viscous terms. It is clear that the accuracy of both the unsteady terms in the fully implicit method as well as the viscous terms may be made second order in space and time using methods that should work well within a Newton iteration. Despite the nominally low accuracy, full viscous solutions we computed showed good agreement with the central difference scheme for steady and early unsteady flows.

References

Cowley, S.J., Hocking, L.M., & Tutty, O.R., 1985, "The Stability of Solutions of the Classical Unsteady Boundary–Layer Equation," *Phys. Fluids*, 28(2), pp. 441–443.

Davis, R.T., 1972, "Numerical Solution of the Navier–Stokes Equations for Flow Past a Parabola," J. Fluid Mech., 51, pp. 417–433.

Davis, R.T., & Werle, M.J., 1982, "Progress on Interacting Boundary Layer Computations at High Reynolds Numbers," *Numerical and Physical Aspects of Aerodynamic Flows*, Vol. II, Springer–Verlag, pp. 187–210.

Peridier, V.J., Smith, F.T., & Walker, J.D.A., 1991, "Vortex–Induced Boundary–Layer Separation" (parts I and II), *J. Fluid Mech.*, 232, pp. 99–131 and pp. 133–165.

Reisenthel, P.H., 1994, "A Study of Reynolds Number Effects on Incipient Leading Edge Stall," AIAA paper 94–2339, 25th AIAA Fluid Dynamics Conference.

Smith, F.T., & Bodonyi, R.J., 1985, "On Short–Scale Inviscid Instabilities in Flow Past Surface–Mounted Obstacles and Other Non–parallel Motions," *Aeronaut. J.*, 89, pp. 205–212.

Tolstykh, A.I., 1994, *High Accuracy Non–Centered Compact Difference Schemes for Fluid Dynamics Applications*, World Scientific Press, Advances in Mathematics for Applied Sciences, vol. 21.

Tutty, O.R., & Cowley, S.J., 1986, "On the Stability and the Numerical Solution of the Unsteady Interactive Boundary–Layer Equation," *J. Fluid Mech.*, 168, pp. 431–456.

Werle, M.J., & Davis, R.T., 1971, "Incompressible Laminar Boundary Layers on a Parabola at Angle of Attack: A Study of the Separation Point," *J. of Appl. Mech.*, paper #71–APM–31.
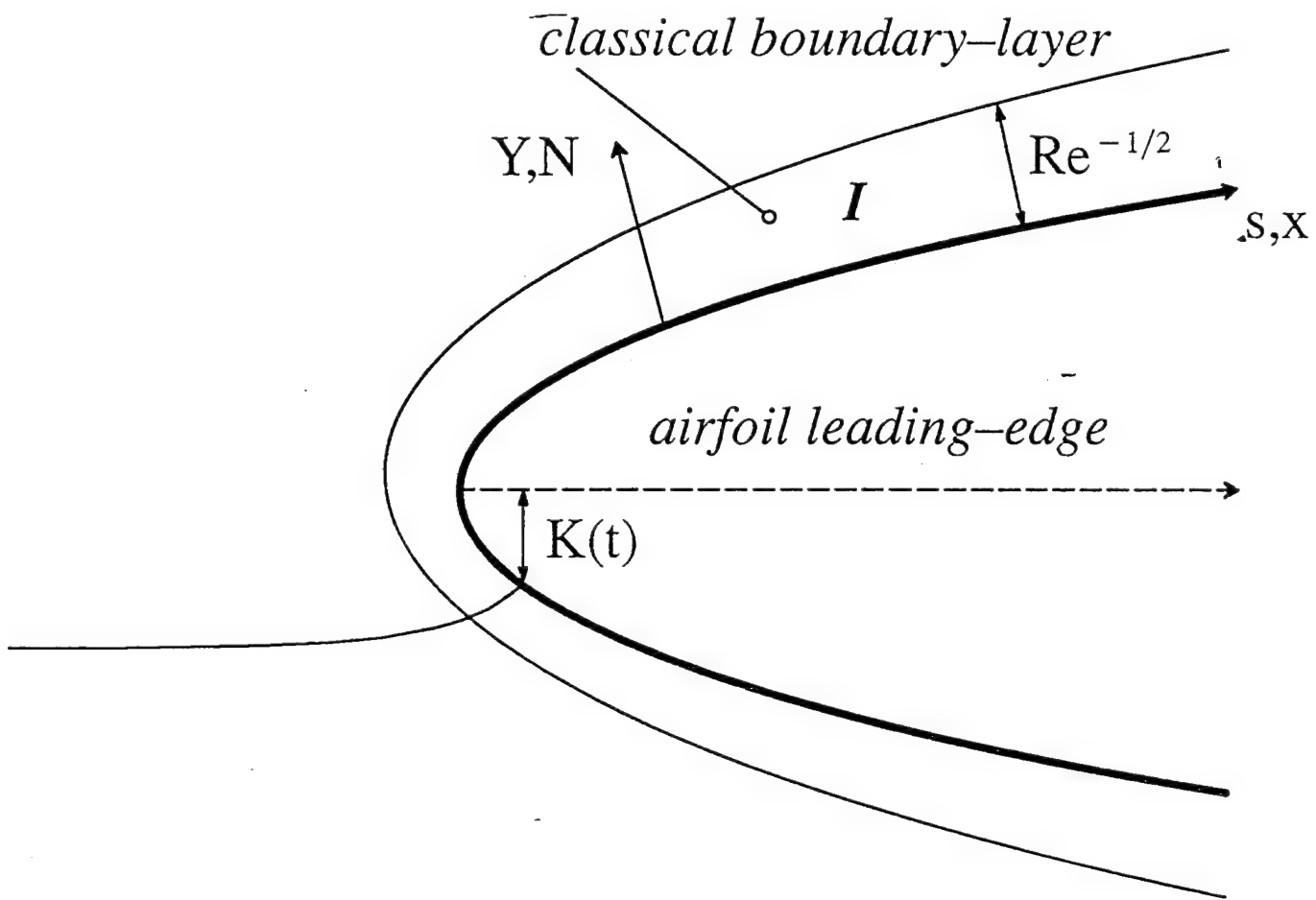
Fig. 1. The high Reynolds number airfoil leading edge and boundary layer structure.
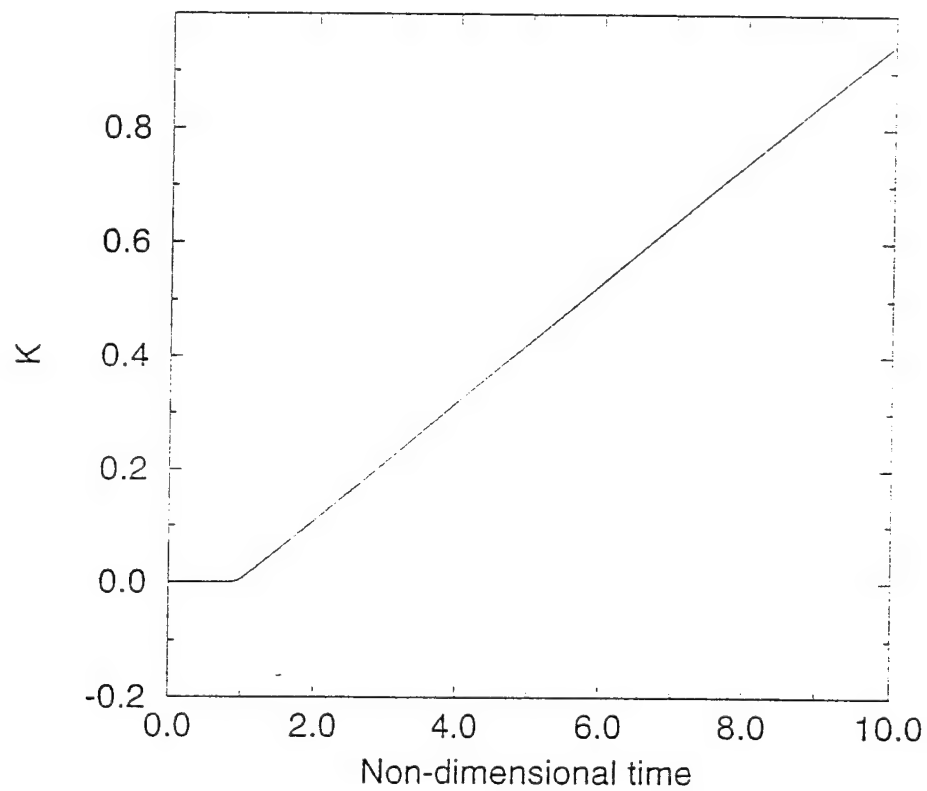
Fig 2. Temporal variation of K(t) for smooth constant rate pitch–up. All solutions are started from the steady solution for a flow past a parabola at zero angle of attack.
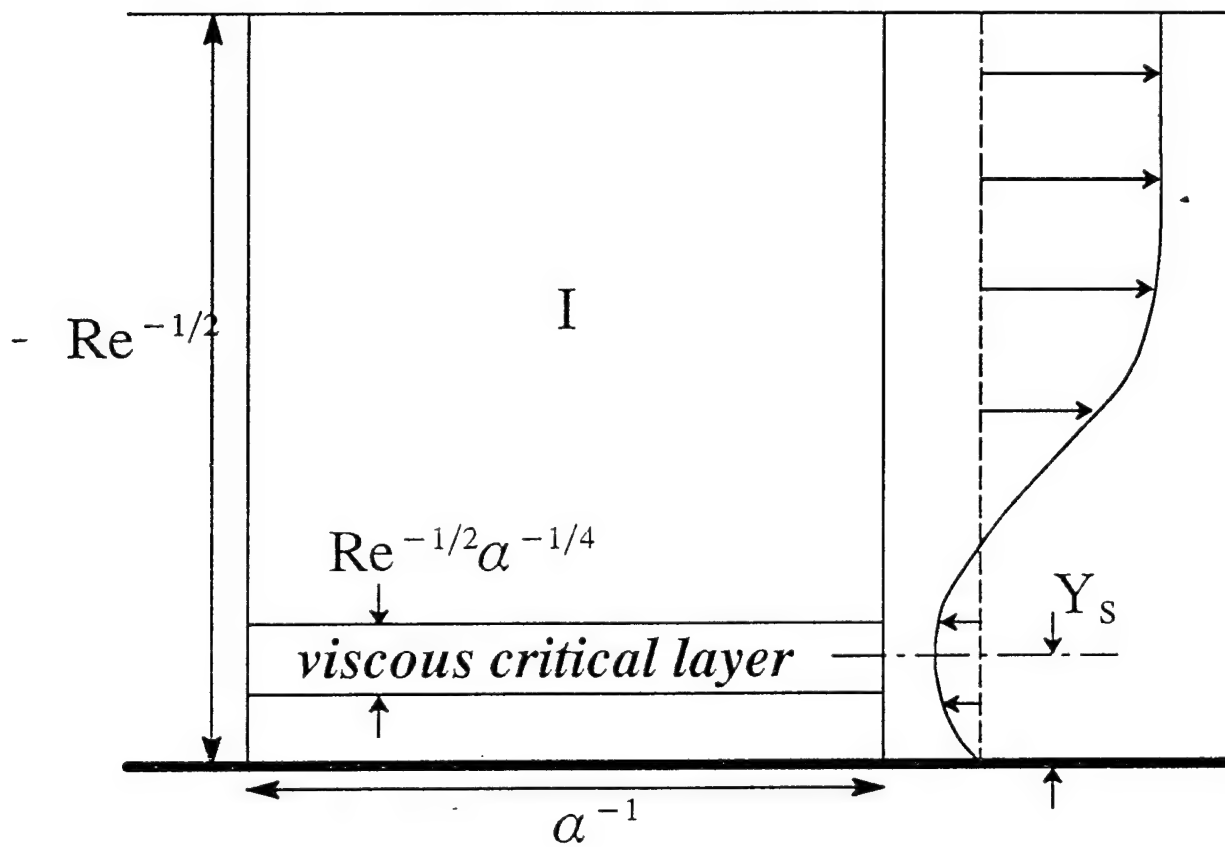
Fig. 3. The high frequency boundary layer instability structure of Cowley, Hocking & Tutty (1985), showing the viscous critical layer positioned at the velocity minimum.
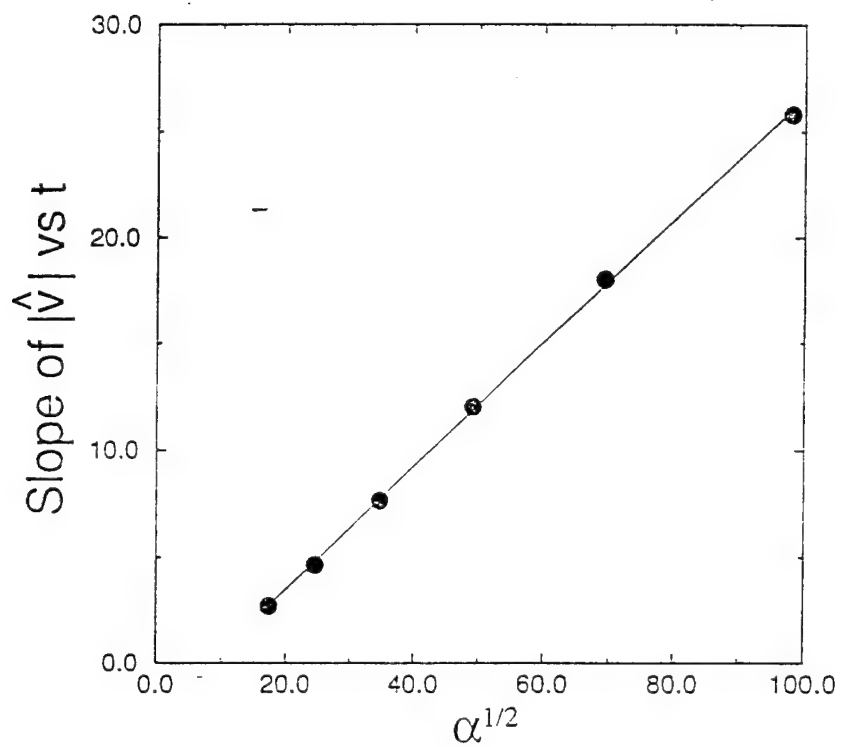
Fig 4. Comparison of Boundary Layer Stability Analysis
Growth Rates with CHT Theory.
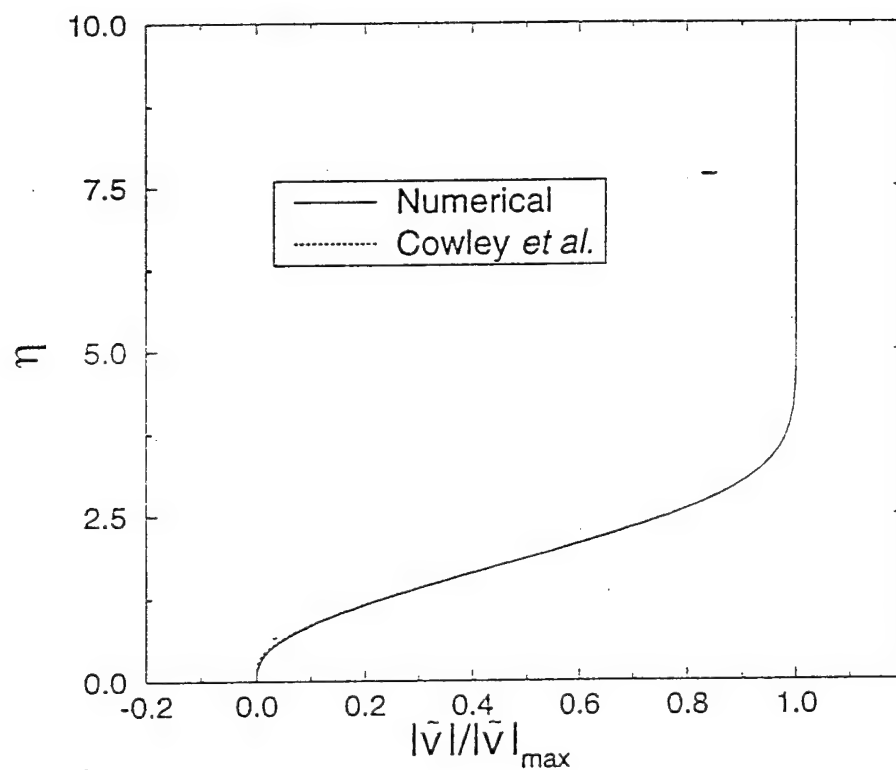
Fig 5. Comparison of Boundary Layer Stability Analysis
Mode Shapes with CHT Theory.

a. Shear stress at K=2.11.
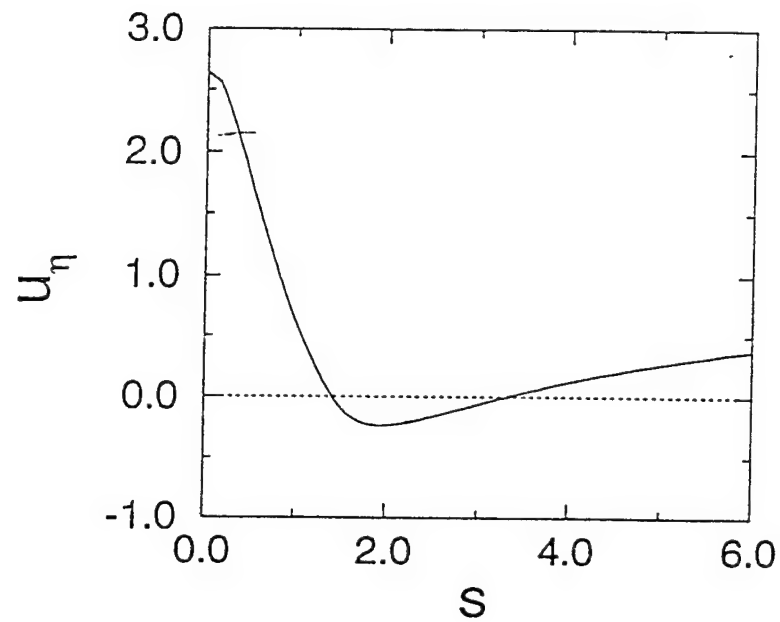
b. Displacement thickness at K=2.11.
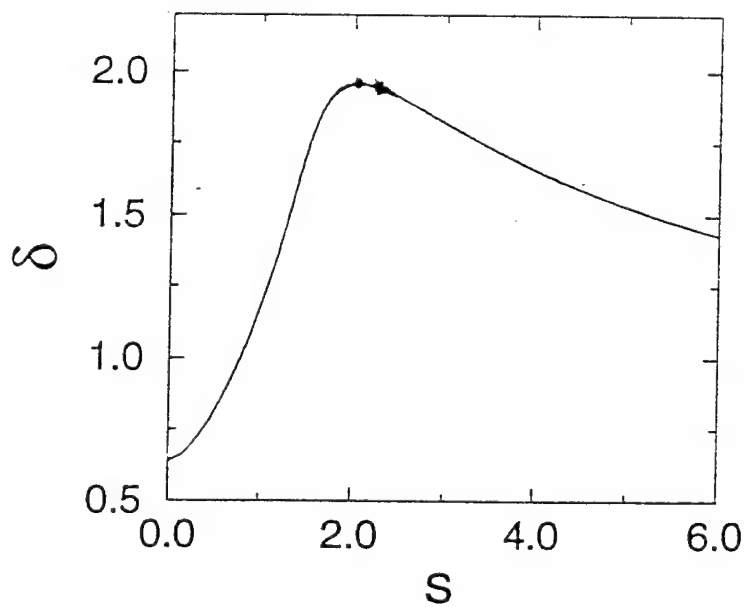
Fig. 6. Wall shear and displacement thickness for early boundary layer computations.
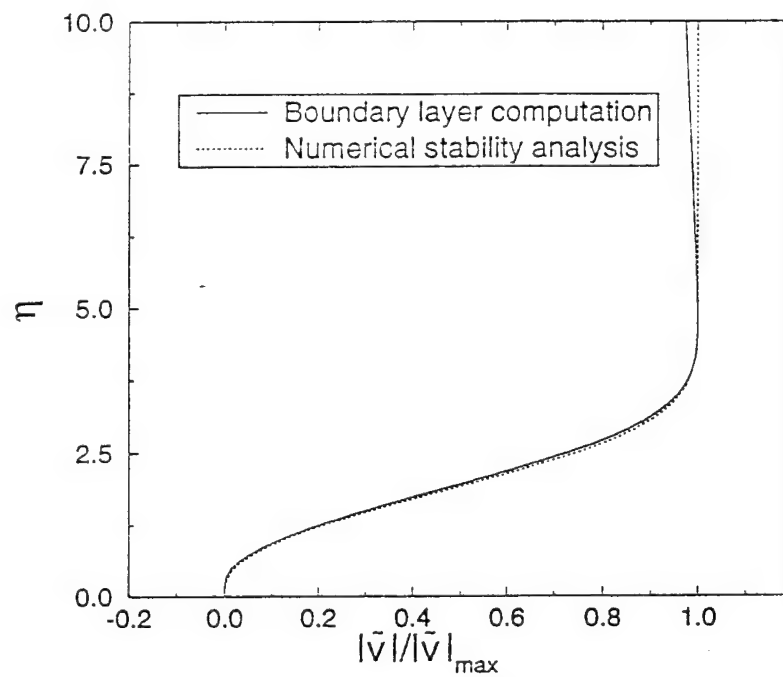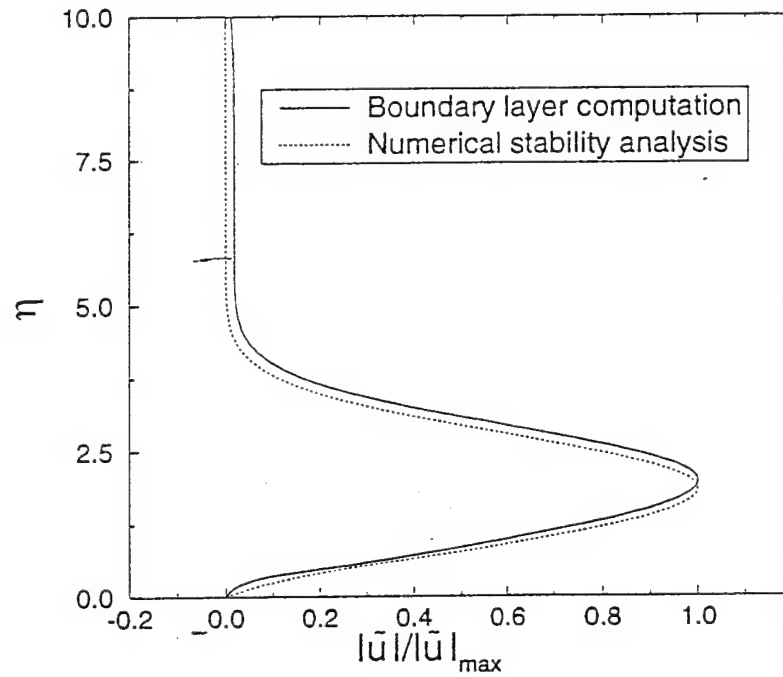
Fig. 7. Comparisons of grid–grid oscillation mode shapes with boundary layer stability mode shapes.
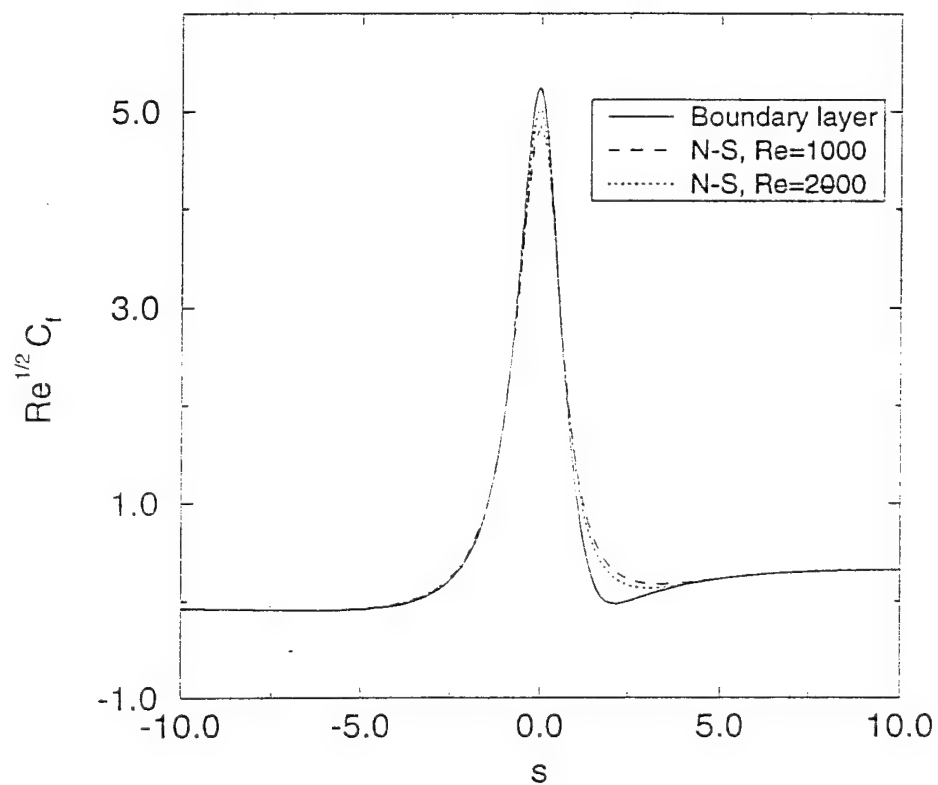
Fig. 8. Wall shear for new boundary layer computations without oscillations.
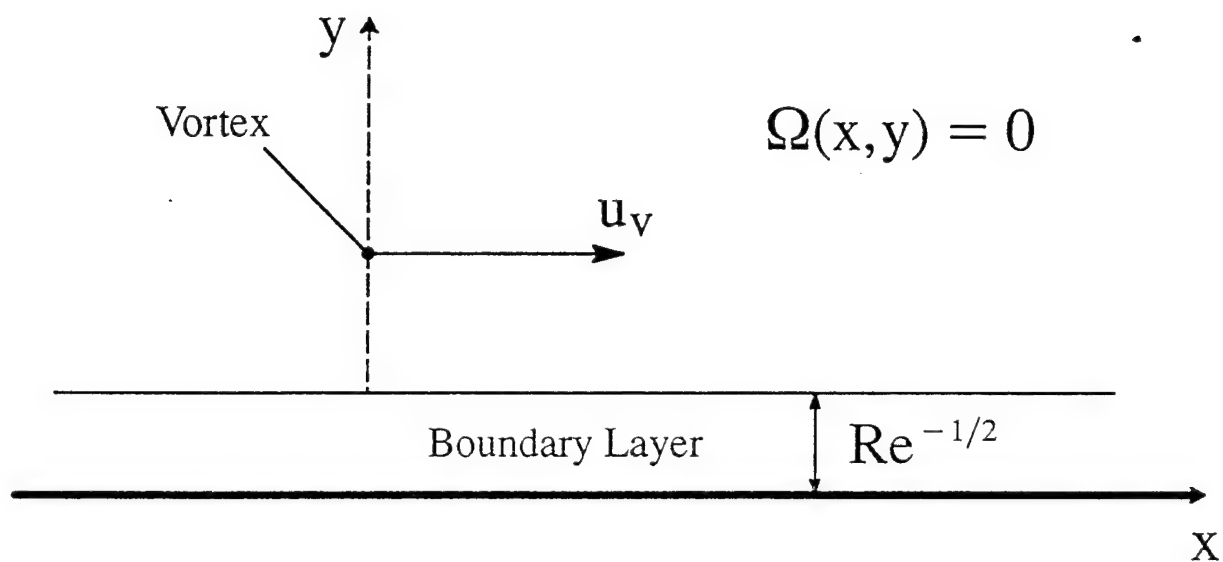
Fig. 9. Geometry for a vortex moving over a
flat plate.
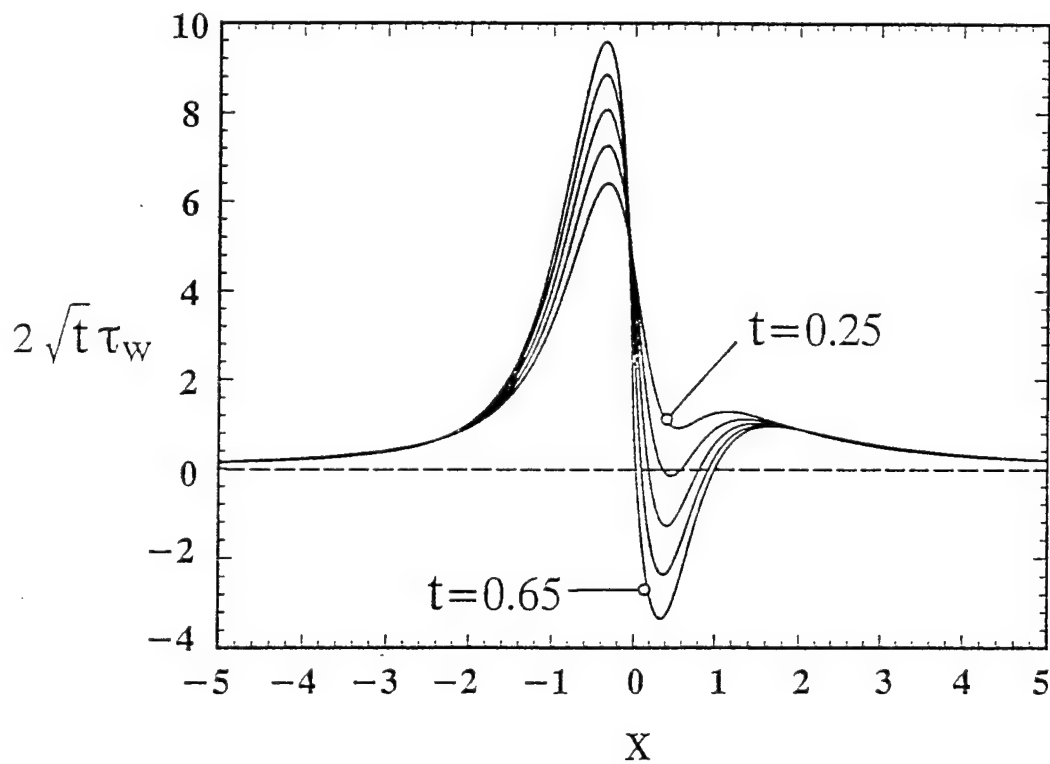
Fig. 10. Scaled wall shear stress early in the unsteady separation computed at various times.
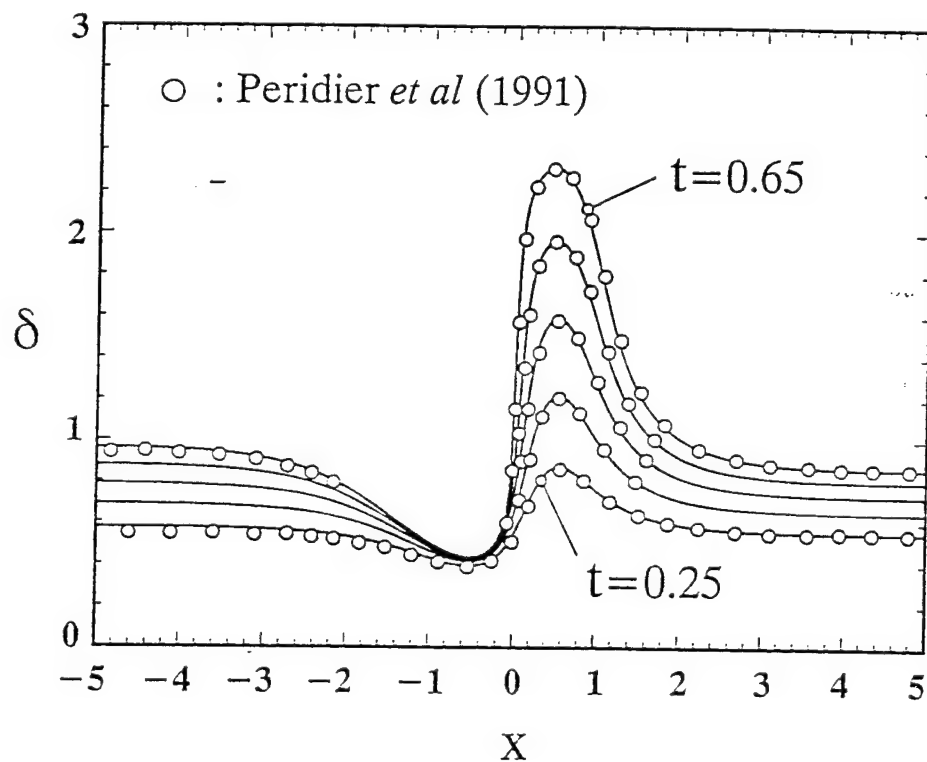
Fig. 11. Displacement thickness computed at various times, the time interval between plots is 0.1. Also shown are comparisons with Peridier *et al* (1991). Results were electronically scanned from original reprints of articles.
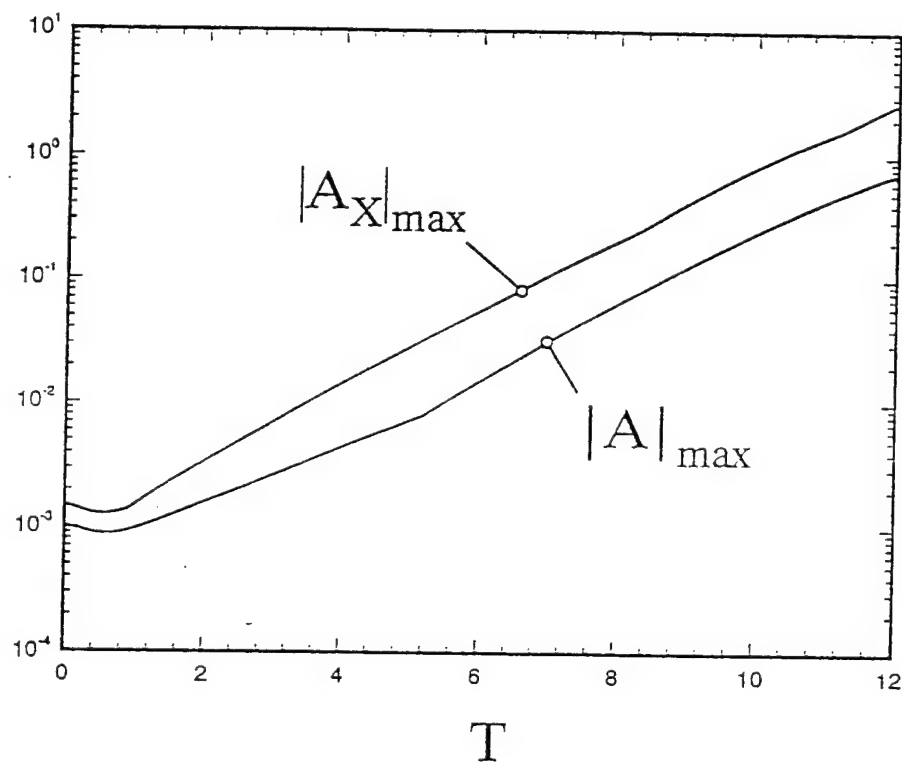
Fig. 12. Maximum absolute displacement function and displacement function slope showing the low amplitude exponential growth.
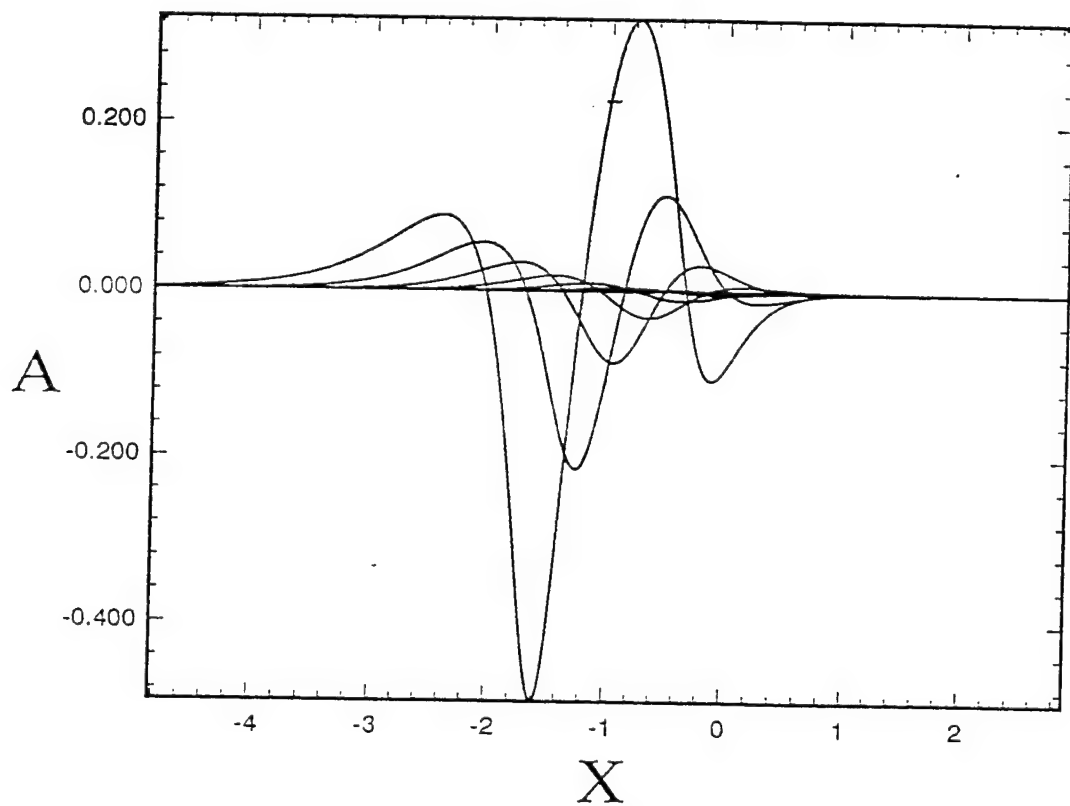
Fig. 13. Displacement function at various times, showing the growth of the displacement function with time.
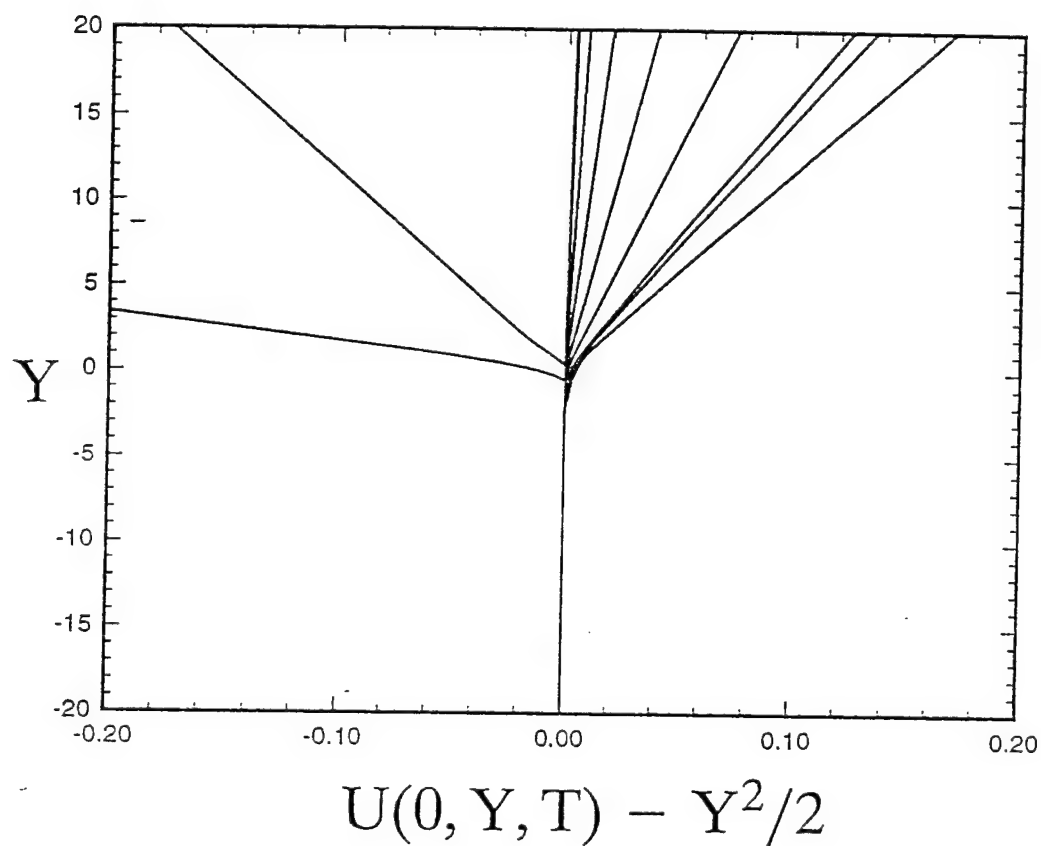
Fig. 14. Deviation of streamwise velocity from parabolic profile in the critical layer at various times, at a typical streamwise location.
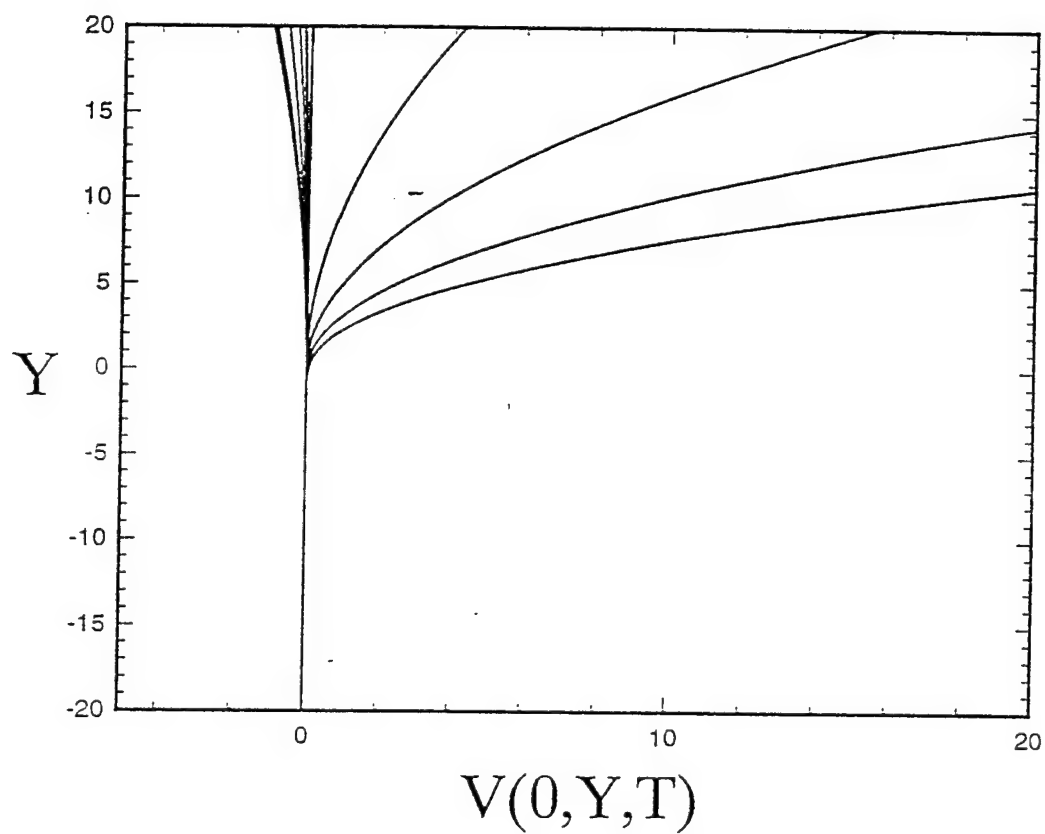
Fig. 15. Normal velocities in the critical layer at various times, at a typical streamwise location.
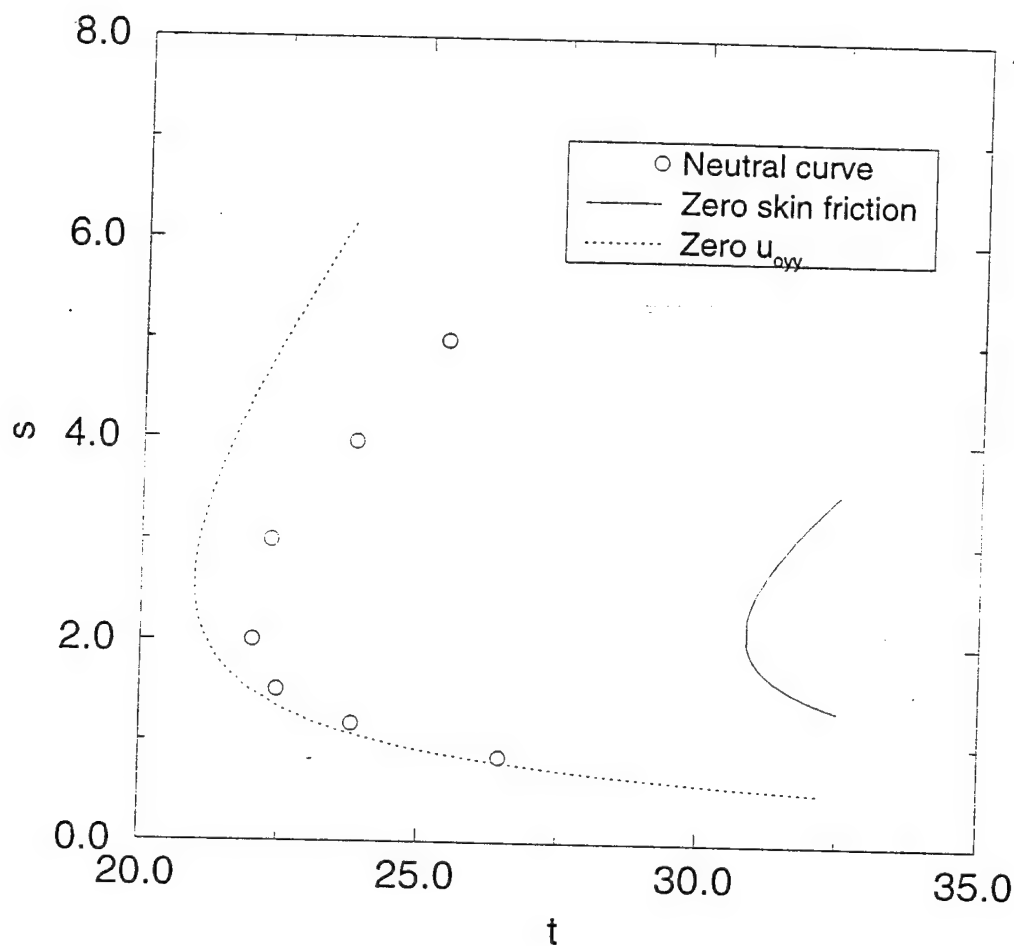
Fig. 16. The Rayleigh instability neutral curve for a parabola in smooth pitch−up. Also shown are the separation curve and the curve of first inflection point creation at the wall.
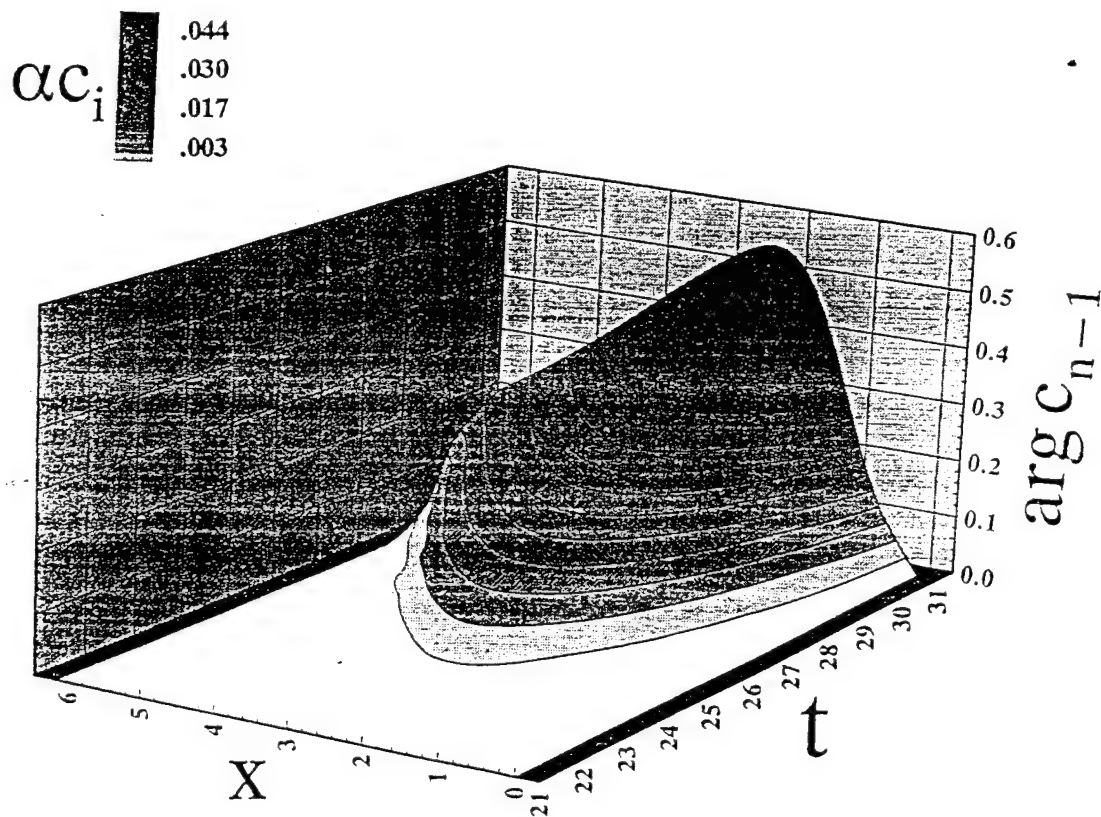
Fig. 17. The arg(c) for the primary Rayleigh instability for a parabola in smooth pitch−up.
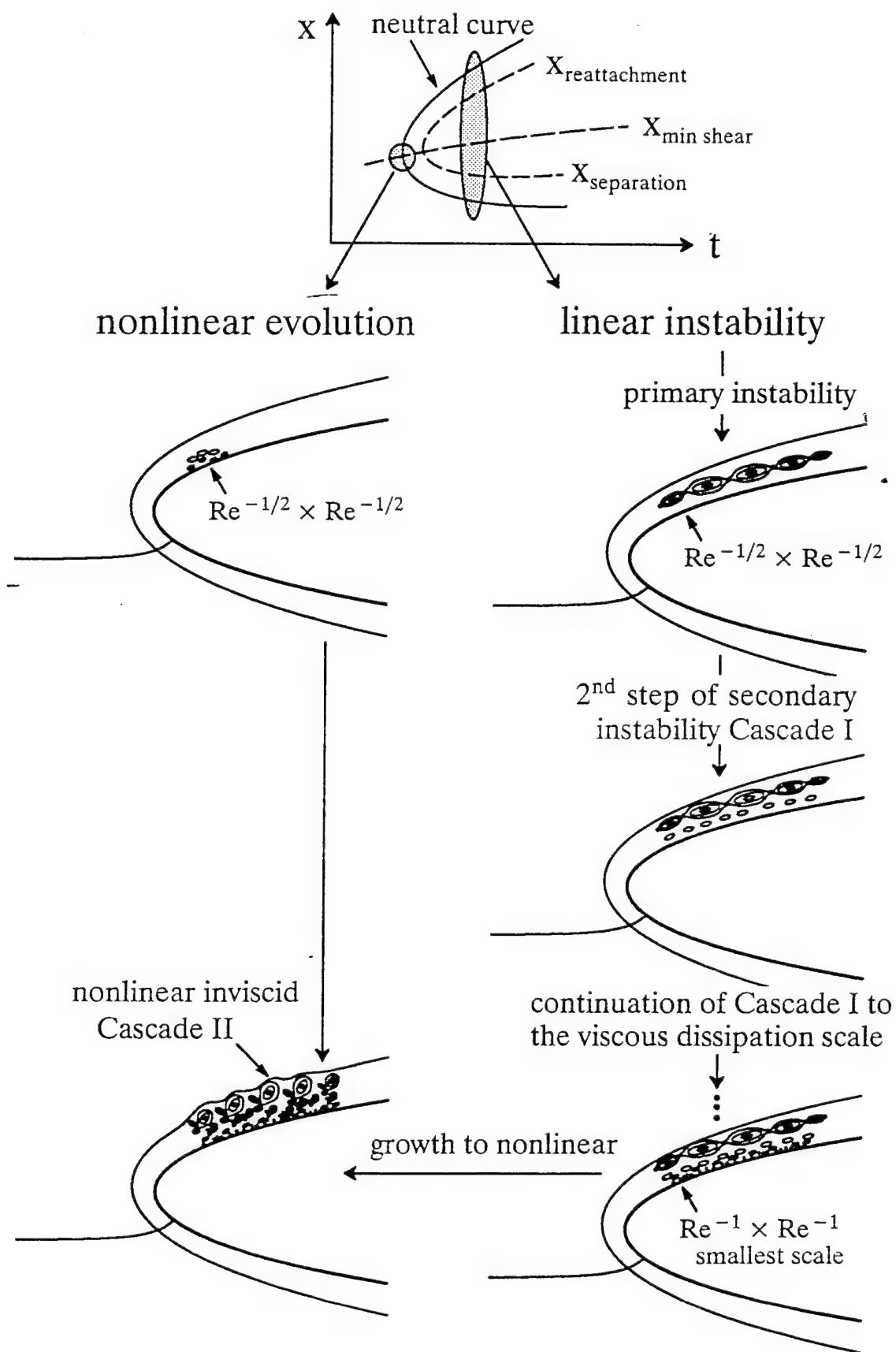
Fig. 18. Anticipated structure of the Rayleigh instability cascade.
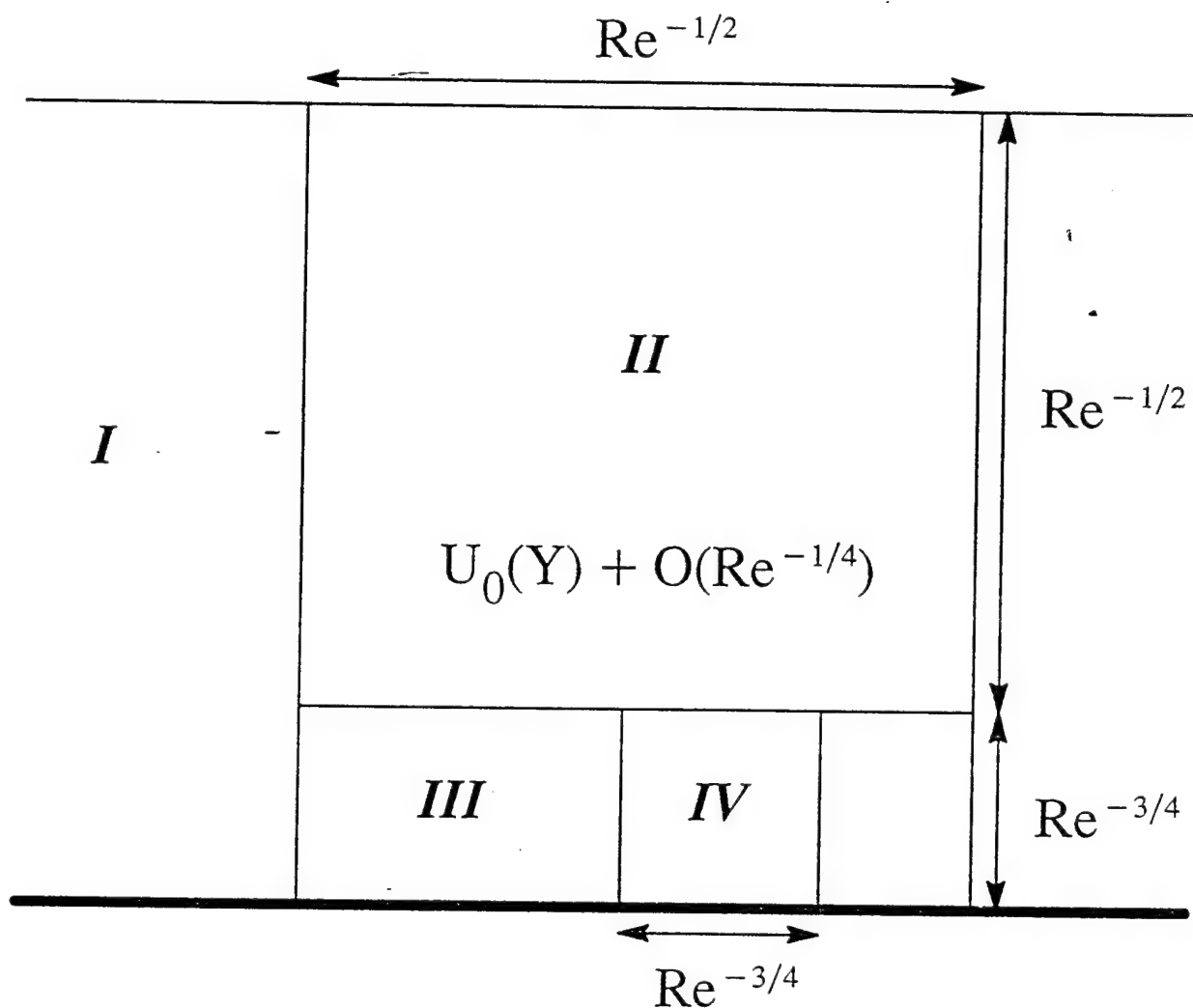
Fig. 19. The initial 2–step cascade: I–boundary layer; II–linear Euler; III–Stokes layer; IV linear or nonlinear Navier–Stokes region.
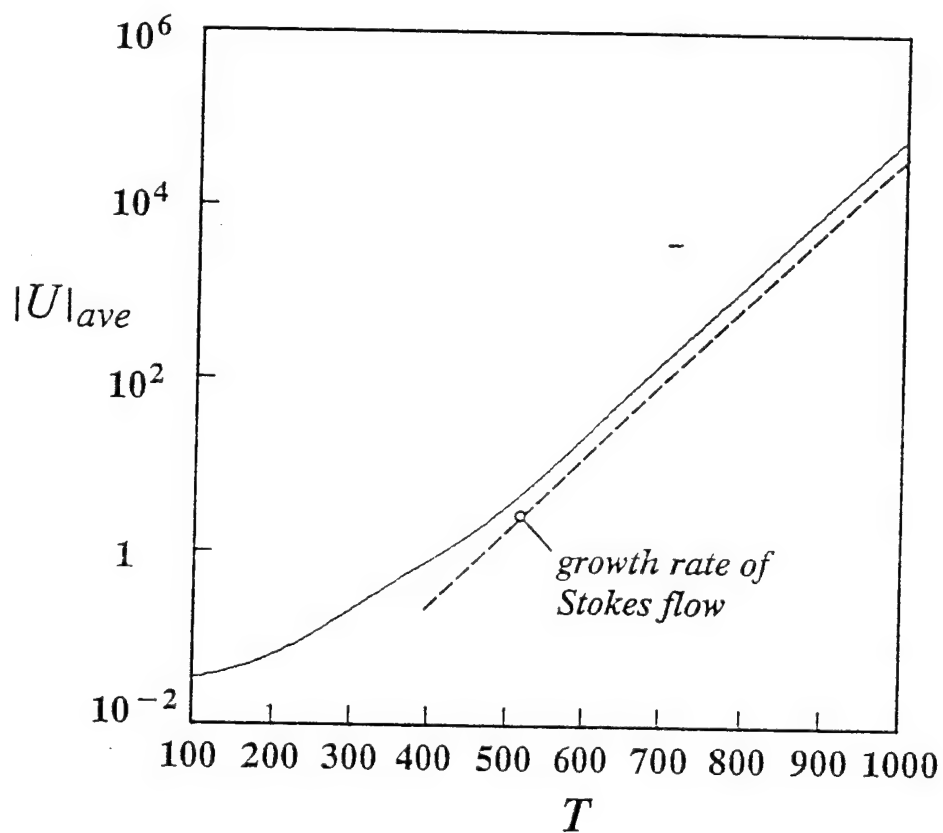
Fig. 20. Response of the Navier–Stokes region of the two–step cascade to an inviscid standing wave instability.
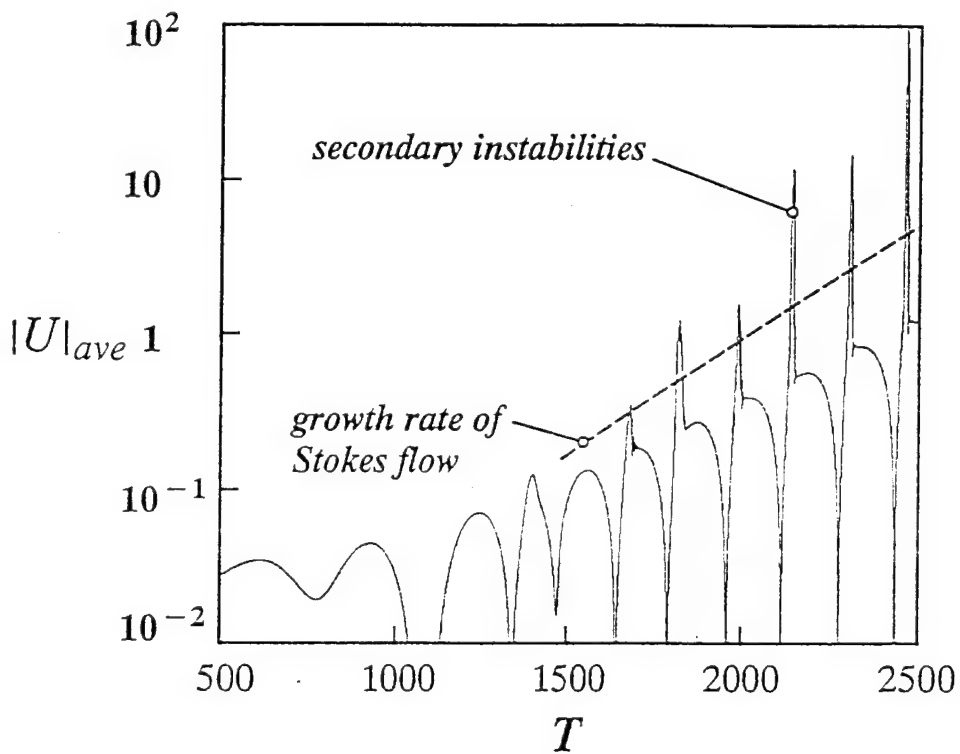
Fig. 21. Typical secondary instability in the Navier–Stokes region of the two–step cascade generated by an inviscid traveling–wave instability.
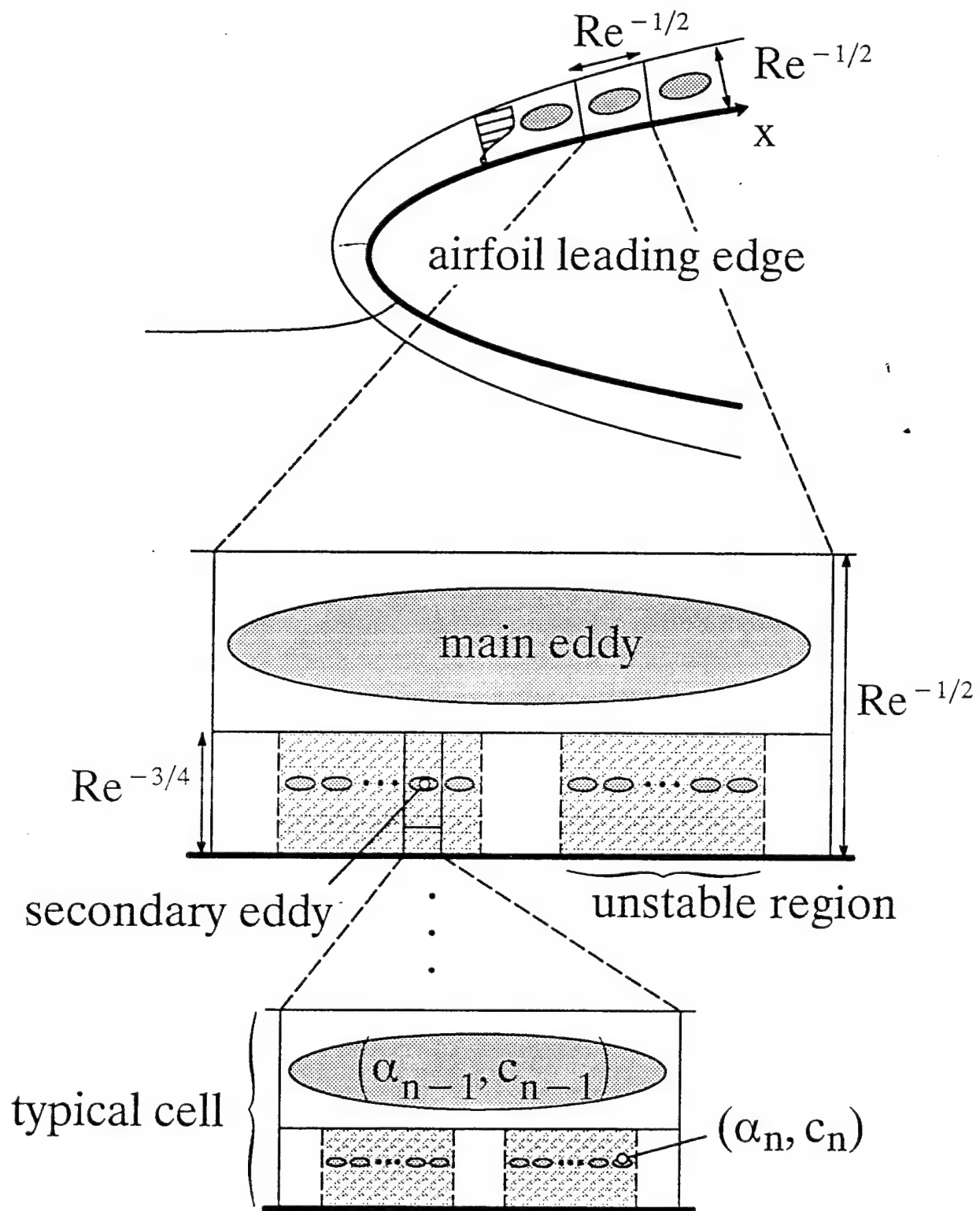
Fig. 22. Schematic diagram of the linear instability cascade.

$$\Delta_1 = \text{Re}^{-1/2}$$

II

$$u \sim U_1 + \varepsilon_1 u_1' + \dots$$

$$\text{Re}^{-1/4} \ll \varepsilon_1 \ll 1$$

$$\delta_1 = \text{Re}^{-1/2}$$

$\bar{I}$

III

$$\text{Re}^{-1/2}\varepsilon_1$$

V

IV

VI

$$\text{Re}^{-7/8}\varepsilon_1^{-1/2}$$

$$\text{Re}^{-3/4}$$

$$\Delta_2 = \text{Re}^{-3/4}$$
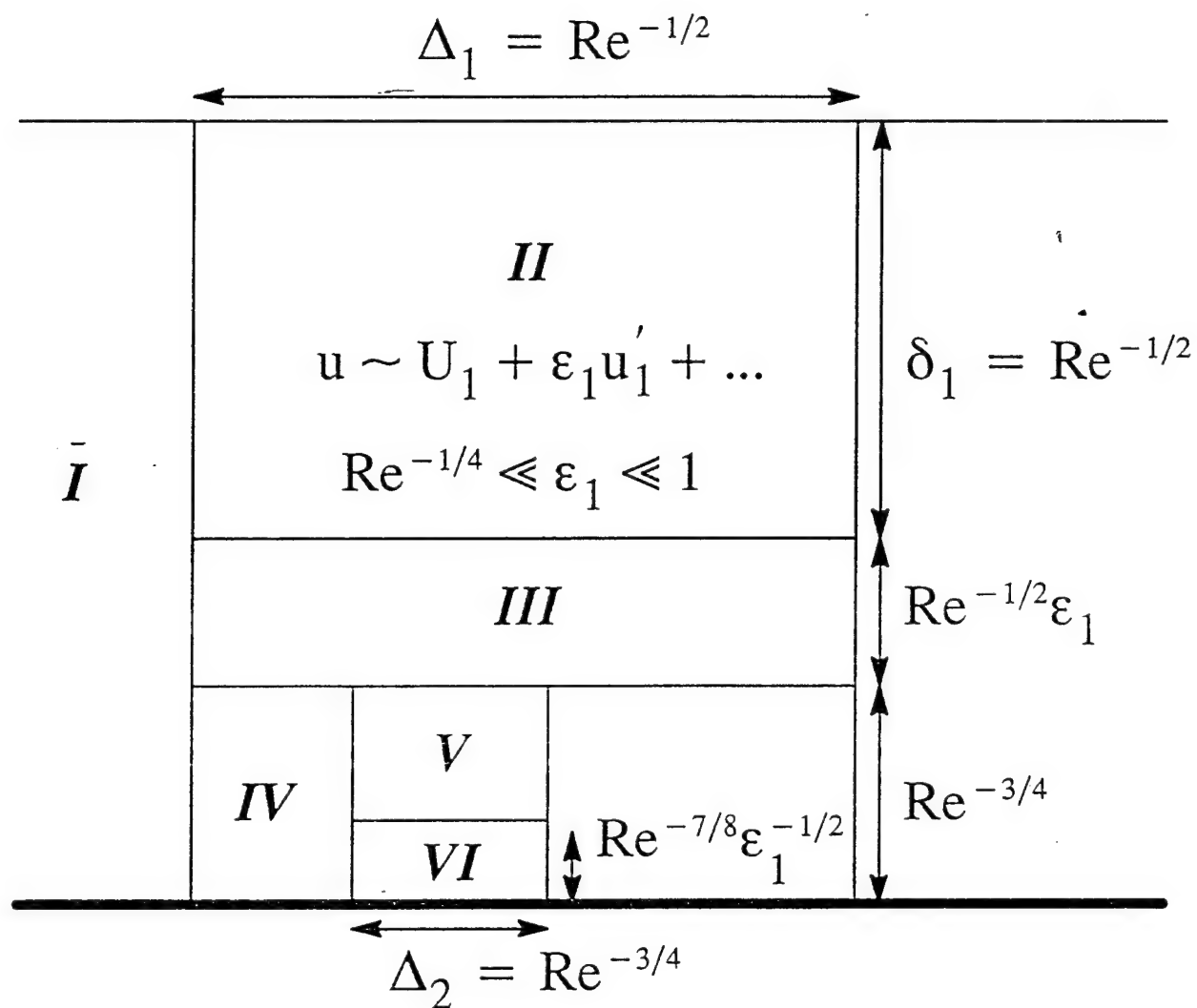
Fig. 23. The initial large amplitude 2–step cascade in a classical external boundary layer: I–classical boundary layer; II–linear Euler region; III– passive thin layer Euler; IV–Stokes layer; V linear or nonlinear Euler region; VI–Stokes layer.
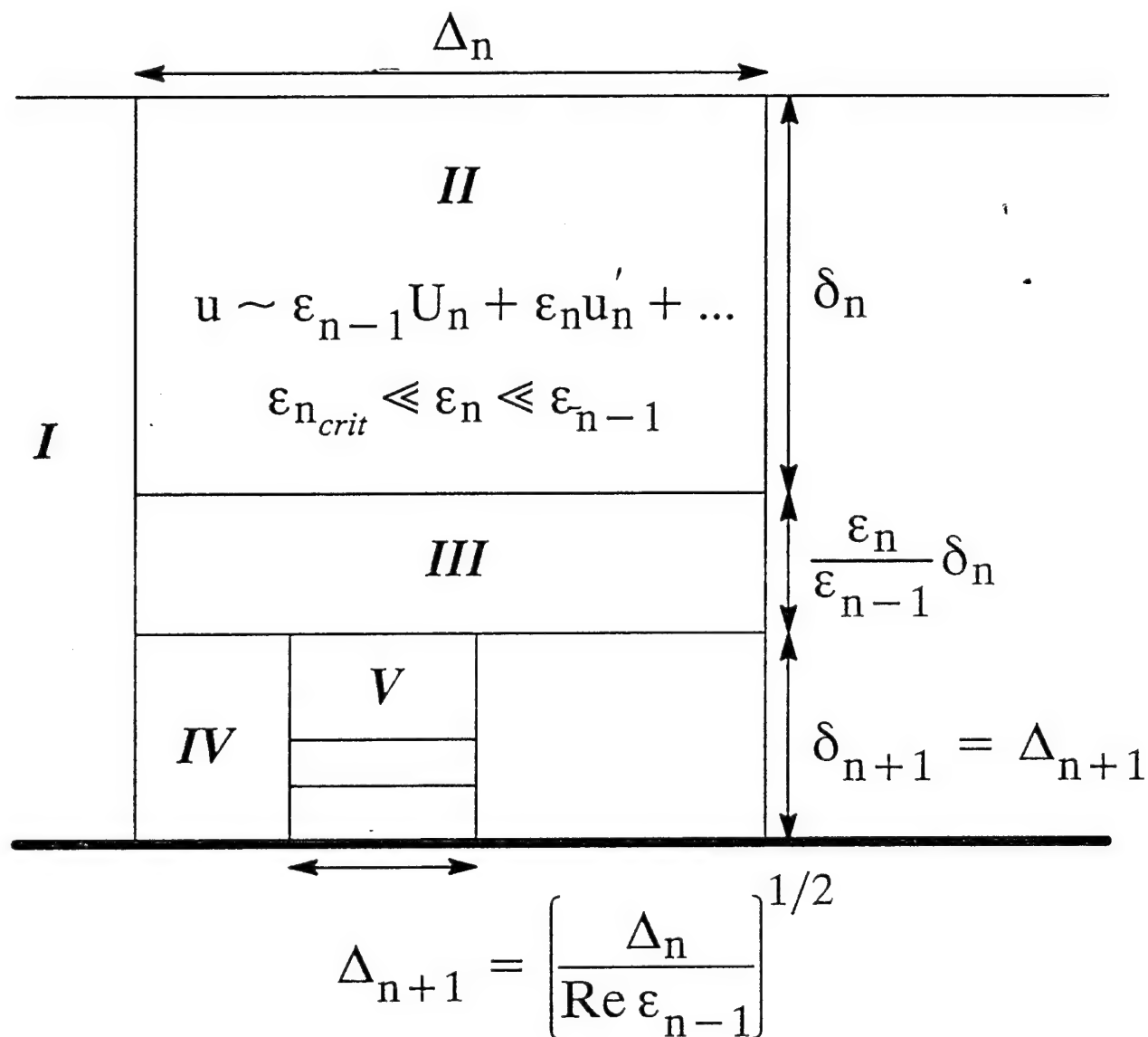
Fig. 24. A general step of the cascade: I– the initial Stokes layer; II–linear Euler; III– passive thin layer Euler; IV– secondary Stokes layer; V linear or nonlinear Euler region.

$$U_o(Y) = \mathrm{Re}^{i\theta}\left(1 - e^{-k_+Y}\right) + \mathrm{c.c}$$
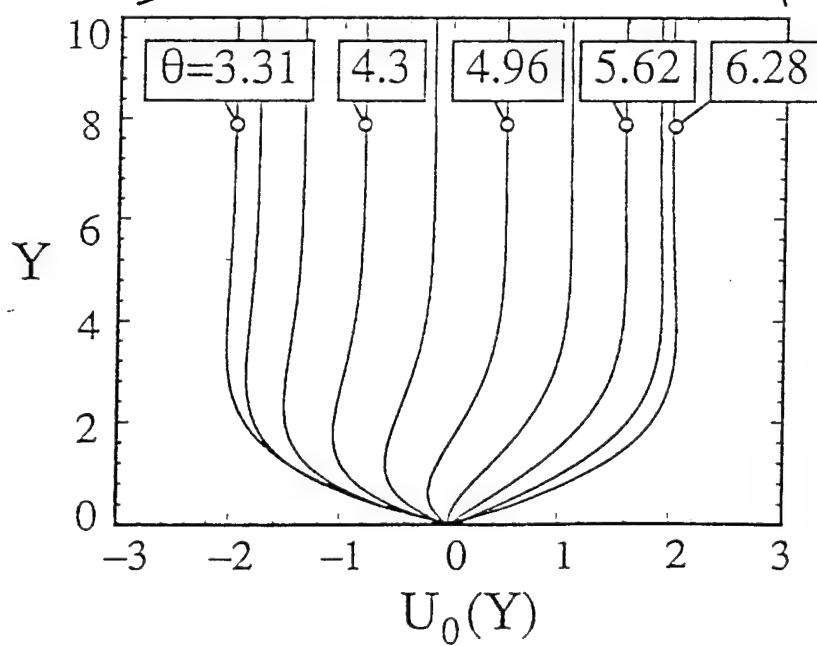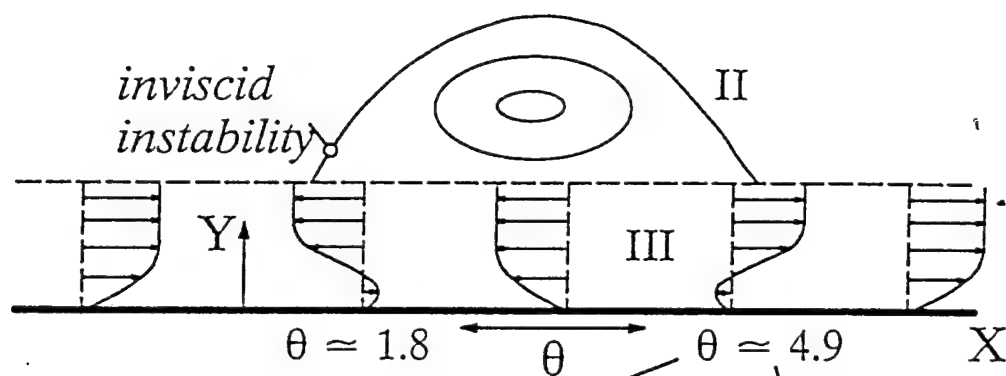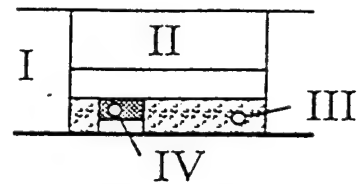
Fig. 25. Stokes layer velocity profiles near the $\theta=4.9$ unstable region.
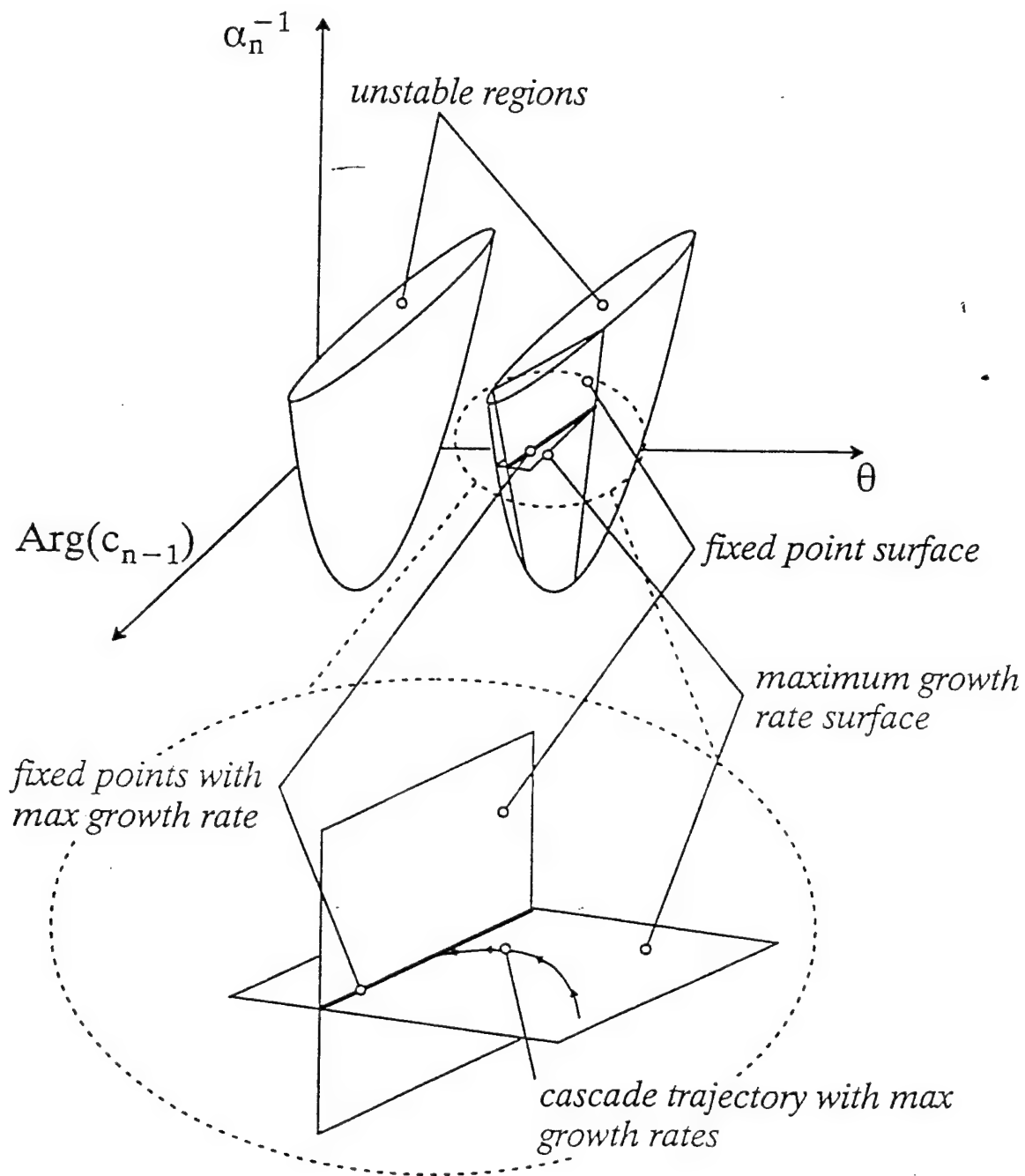
Fig. 26. Schematic diagram of the reduced stability problem for a typical cell in the instability cascade.

The labels in the figure read:

α_n^{-1}

unstable regions

θ

$\text{Arg}(c_{n-1})$

fixed point surface

maximum growth rate surface

fixed points with max growth rate

cascade trajectory with max growth rates

65
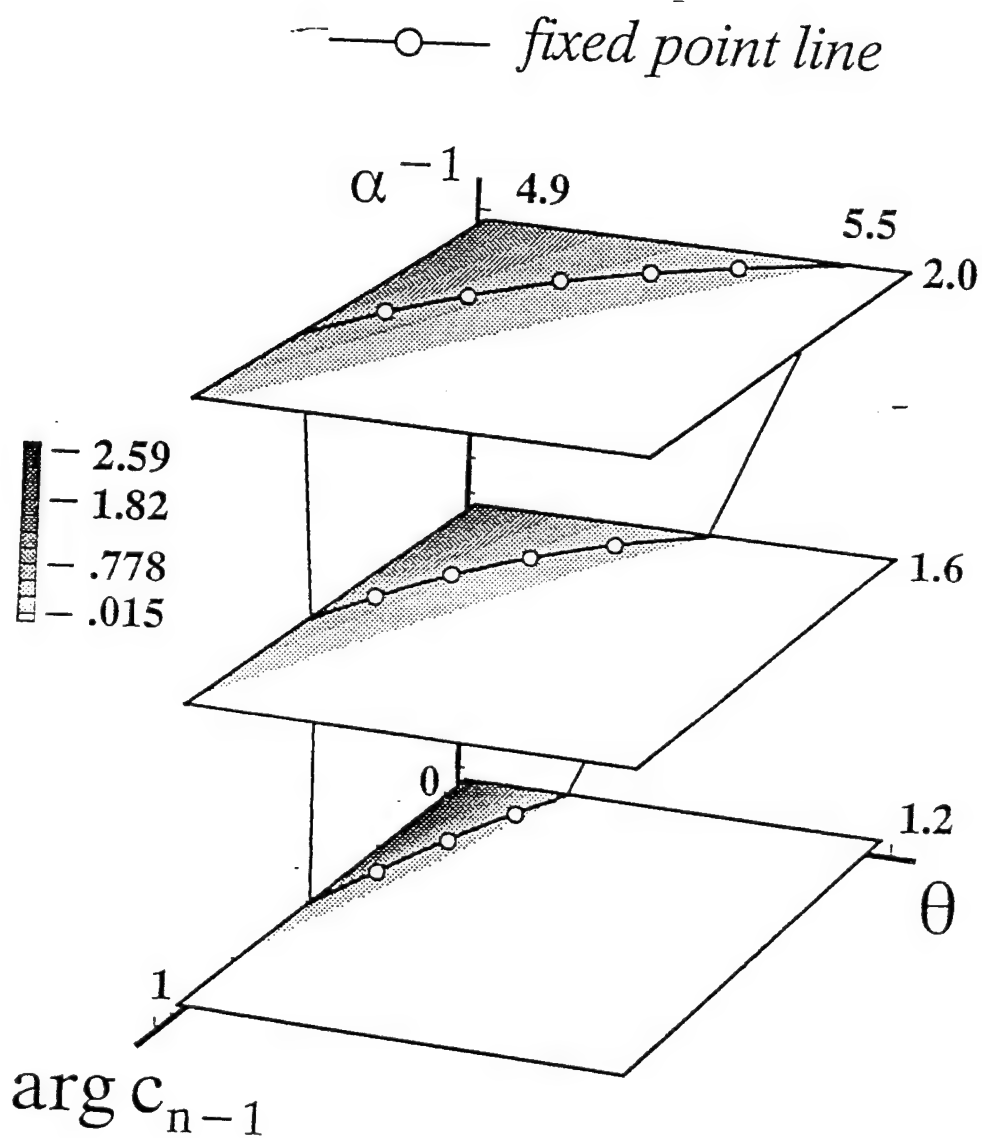
Fig. 27. A view of a portion of the right unstable
region containing the fixed point surface.
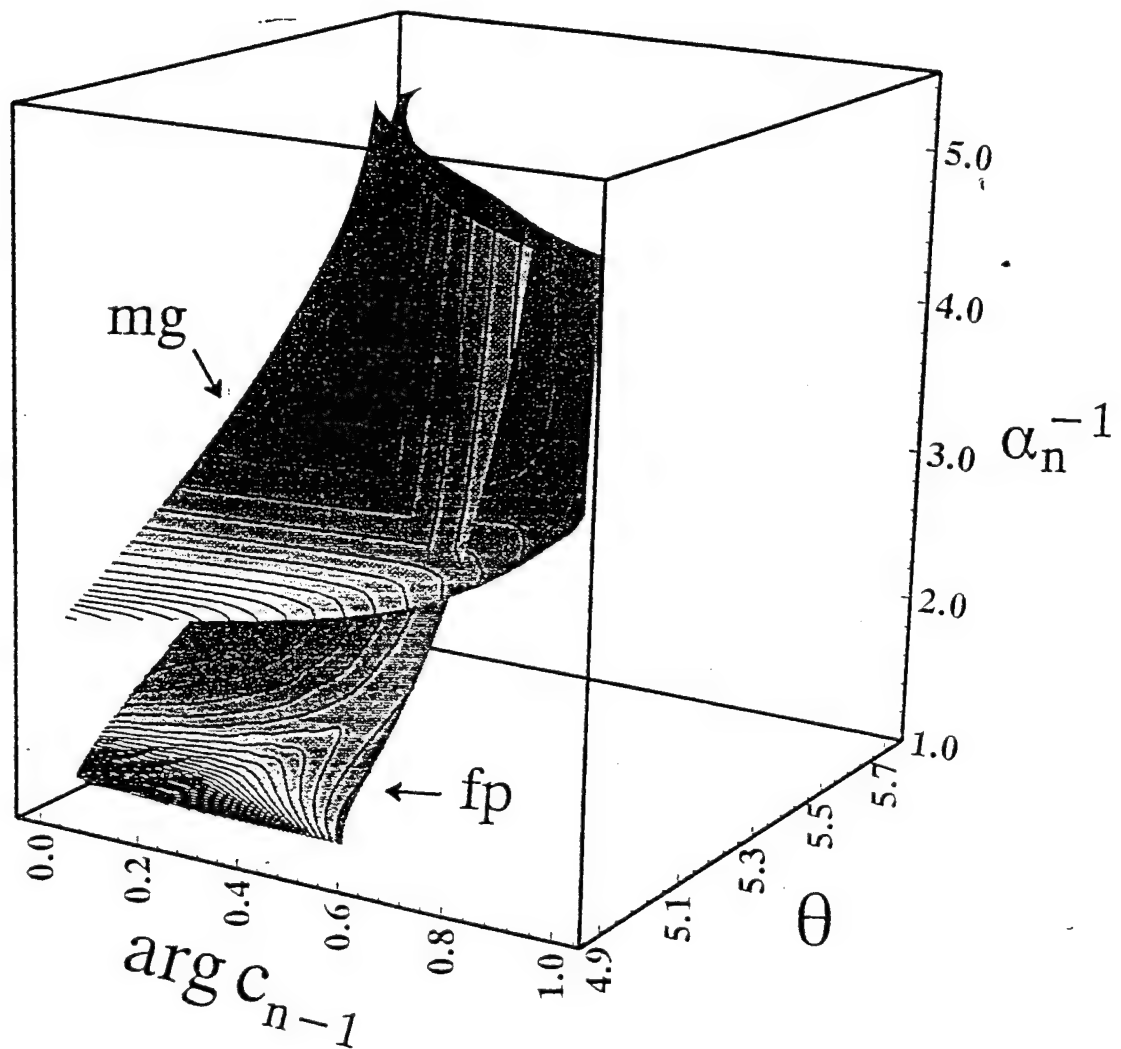
Fig. 28. The right fixed point surface showing contours of arg(c), as well as the maximum growth rate surface, showing the intersection of the maximum growth rate surface with the fixed point surface.
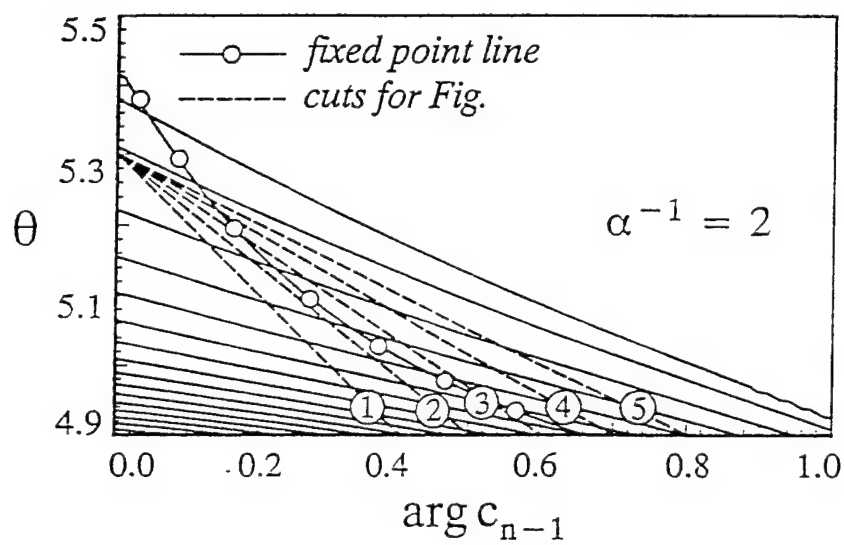
Fig. 29. A fixed wavelength cut through the unstable region.
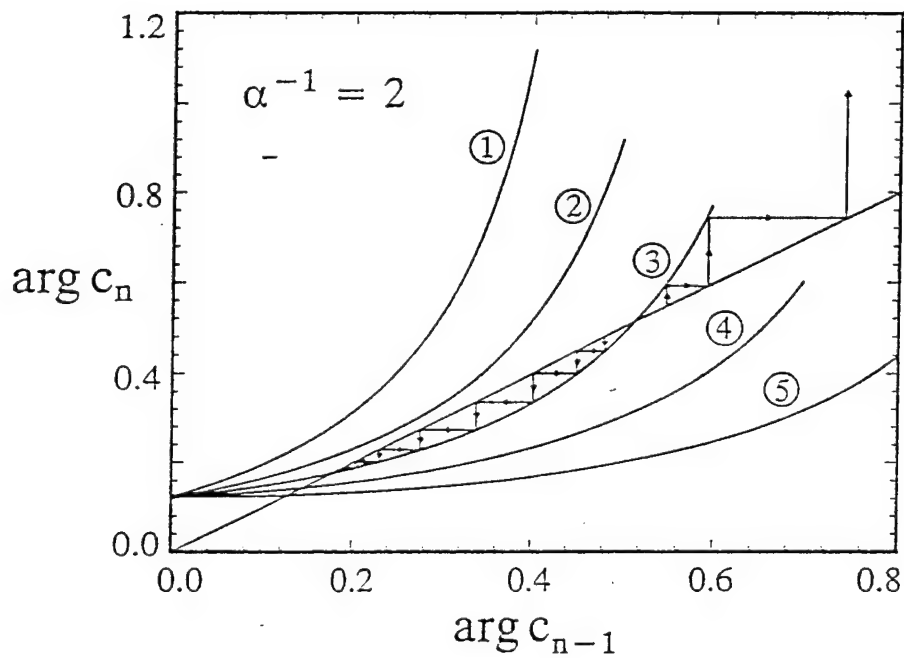
Fig. 30. Arg(c) along the cuts of Fig. 29 showing an unstable fixed point and a stable fixed point. The stable fixed point yields a self–similar cascade to the viscous dissipation scale.
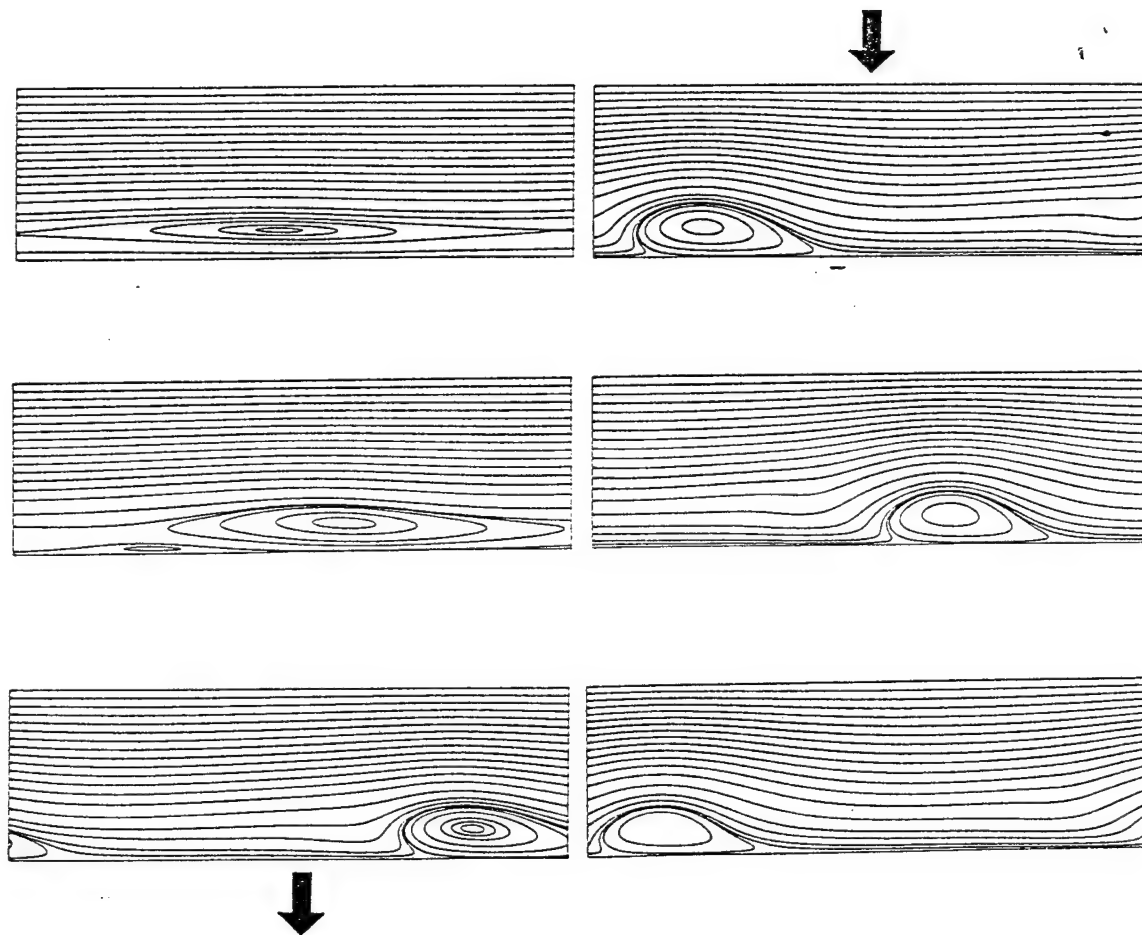
Fig. 31. Streamfunction contours for the nonlinear development of a viscous Rayleigh instability in a Stokes layer profile at Re=200.
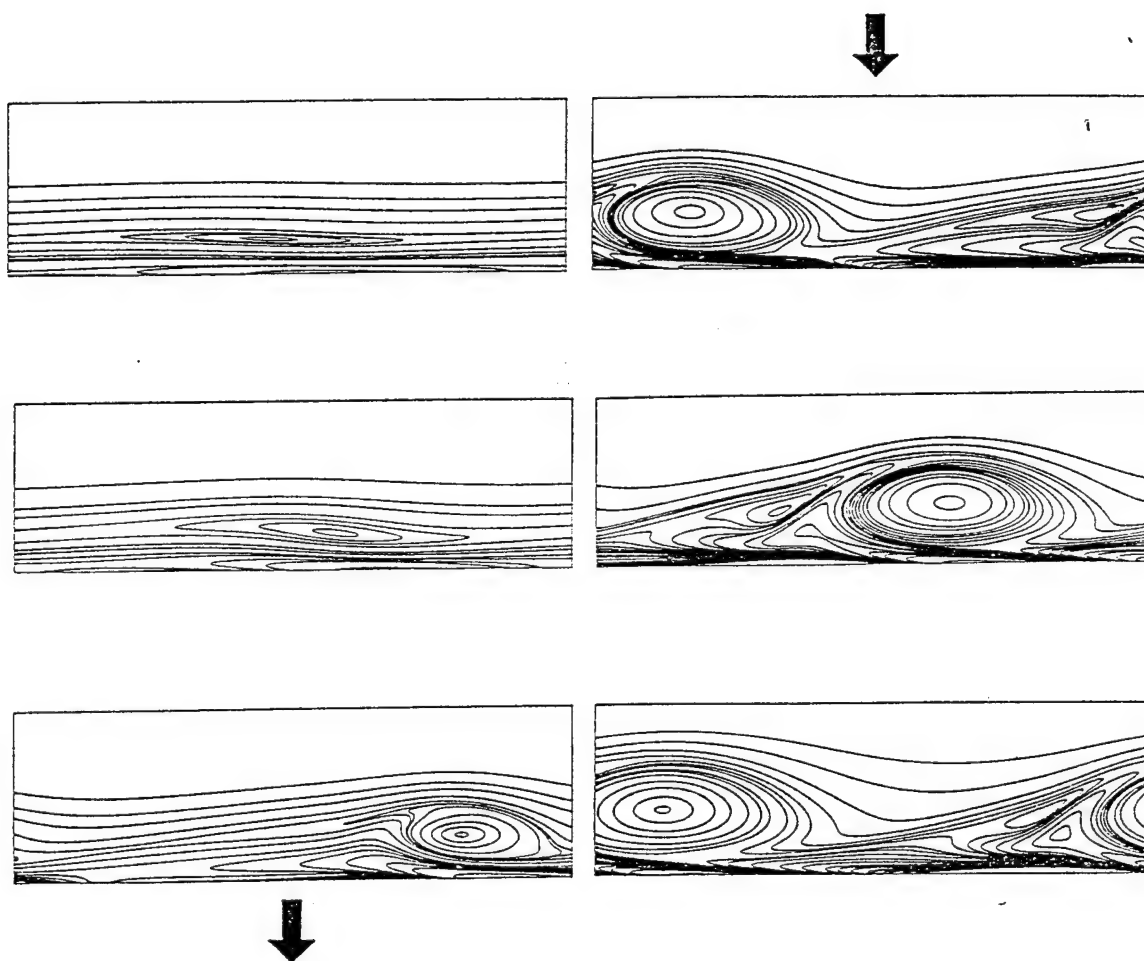
Fig. 32. Vorticity contours for the nonlinear development of a viscous Rayleigh instability in a Stokes layer profile at Re=200.
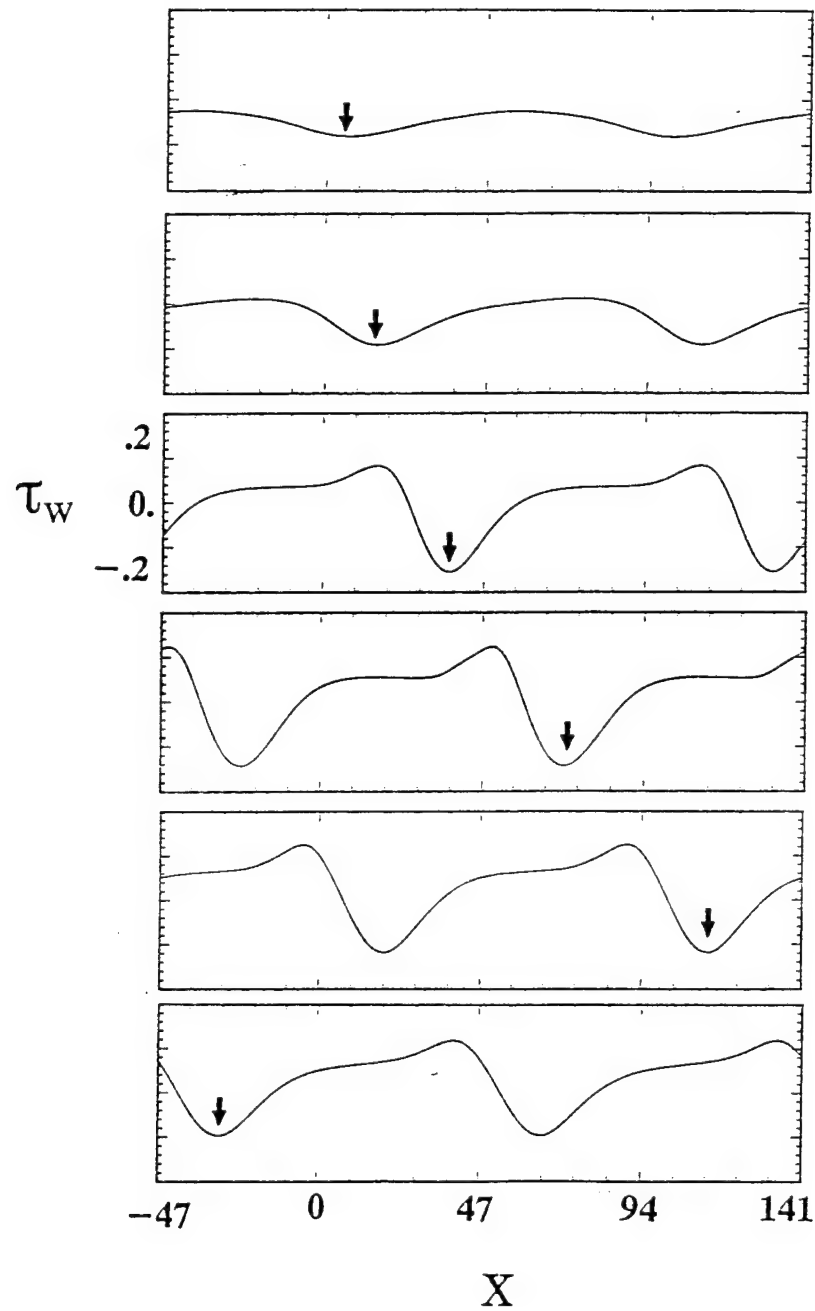
Fig. 33. Wall shear stress for the nonlinear development of a Rayleigh instability in a Stokes layer profile at Re=200, showing soliton like behavior at large time.
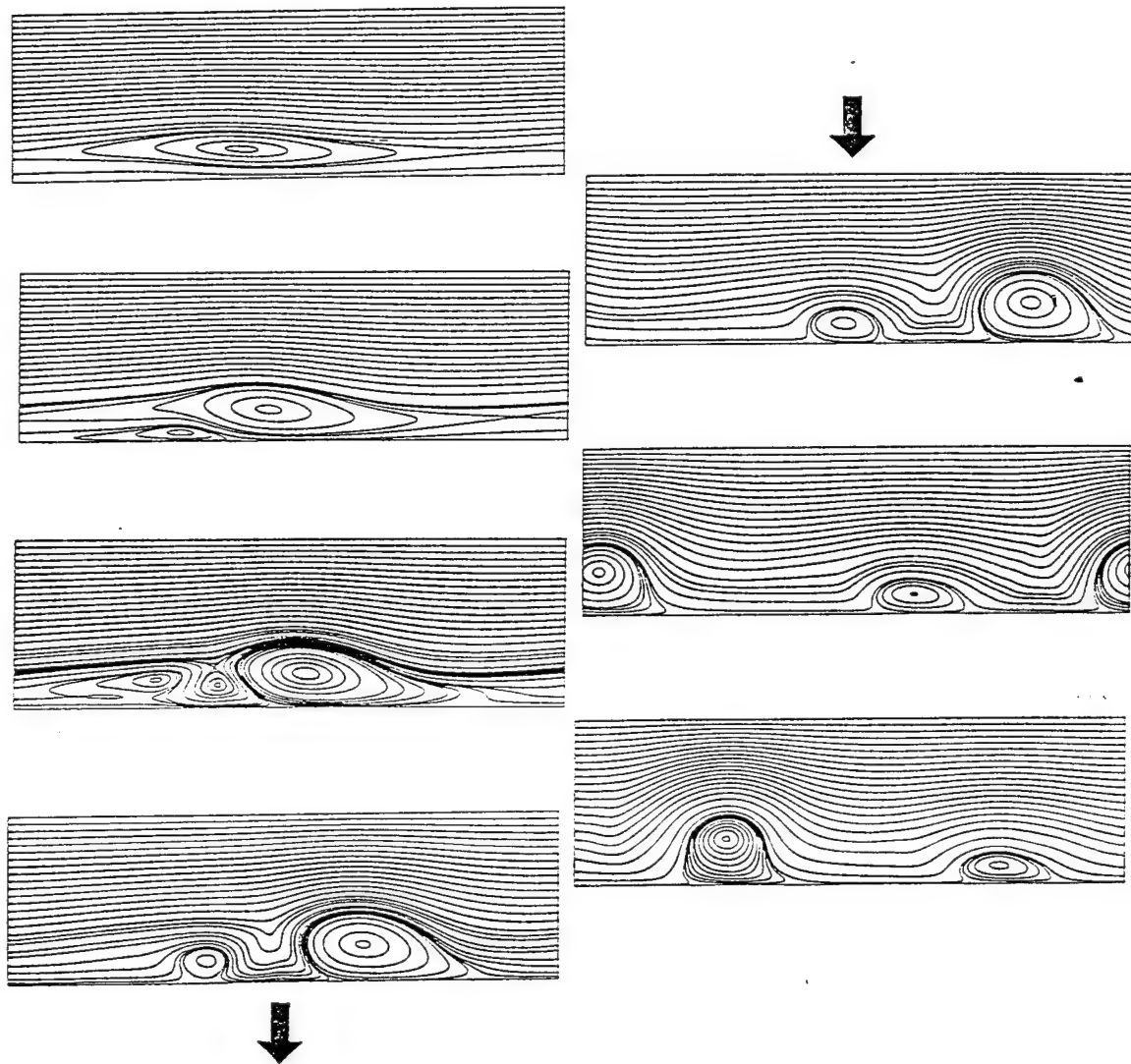
Fig. 34. Streamfunction contours for the nonlinear development of a viscous Rayleigh instability in a Stokes layer at Re=400. The vorticity contours for this solution show the spurious oscillations normally encountered in the central difference scheme for the high Re viscous problems and the inviscid problem.
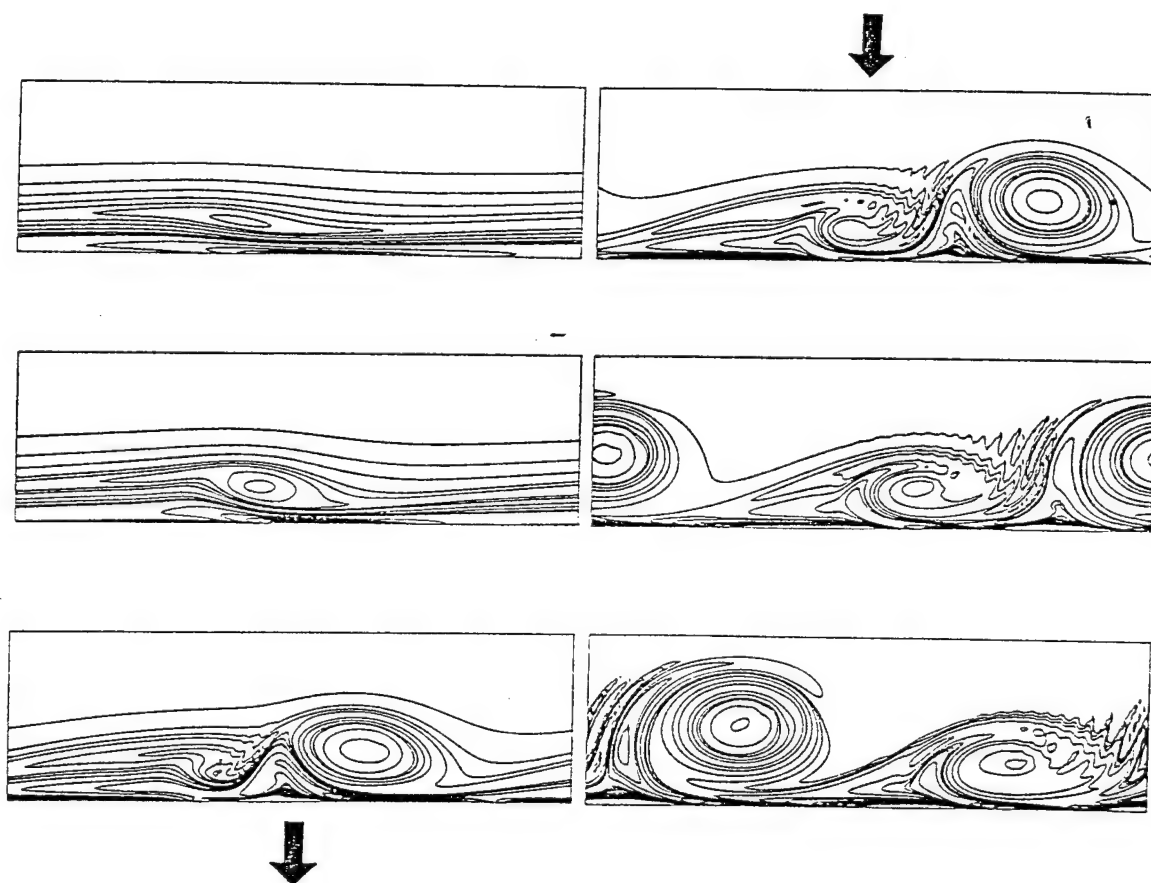
Fig. 35. Vorticity contours for the nonlinear development of a viscous Rayleigh instability in a Stokes layer at Re=400, showing spurious oscillations.

a) T=630:

b) T=924:

c) T=987:

d) T=1050:
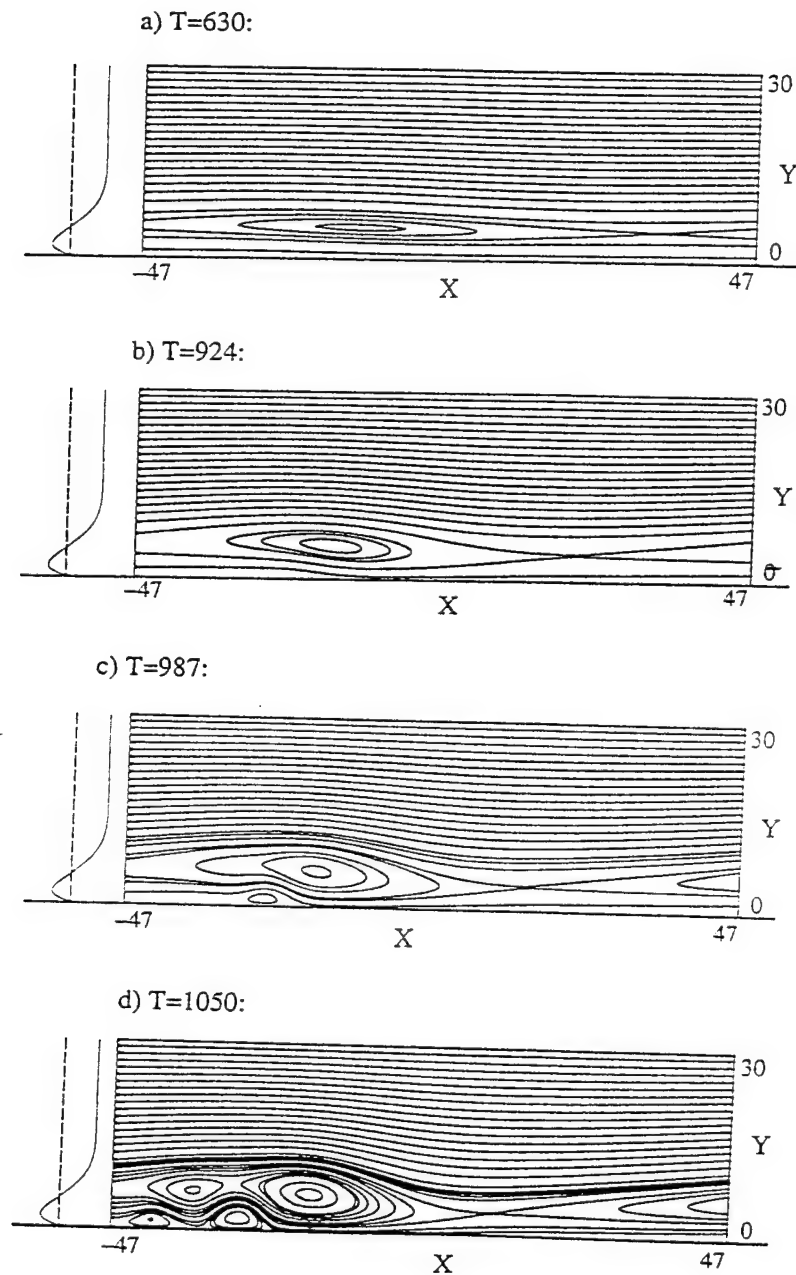
Fig. 36. Typical streamfunction contours for the nonlinear development of an inviscid Rayleigh instability in a Stokes layer, using central difference scheme.
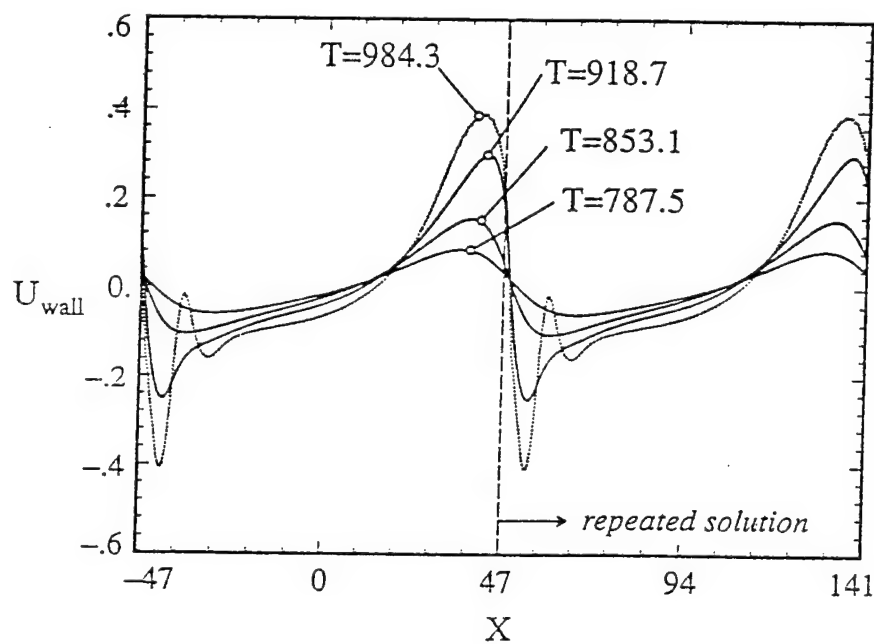
Fig. 37. Wall slip velocity for the nonlinear development of an inviscid Rayleigh instability in a Stokes layer profile using a central difference scheme.
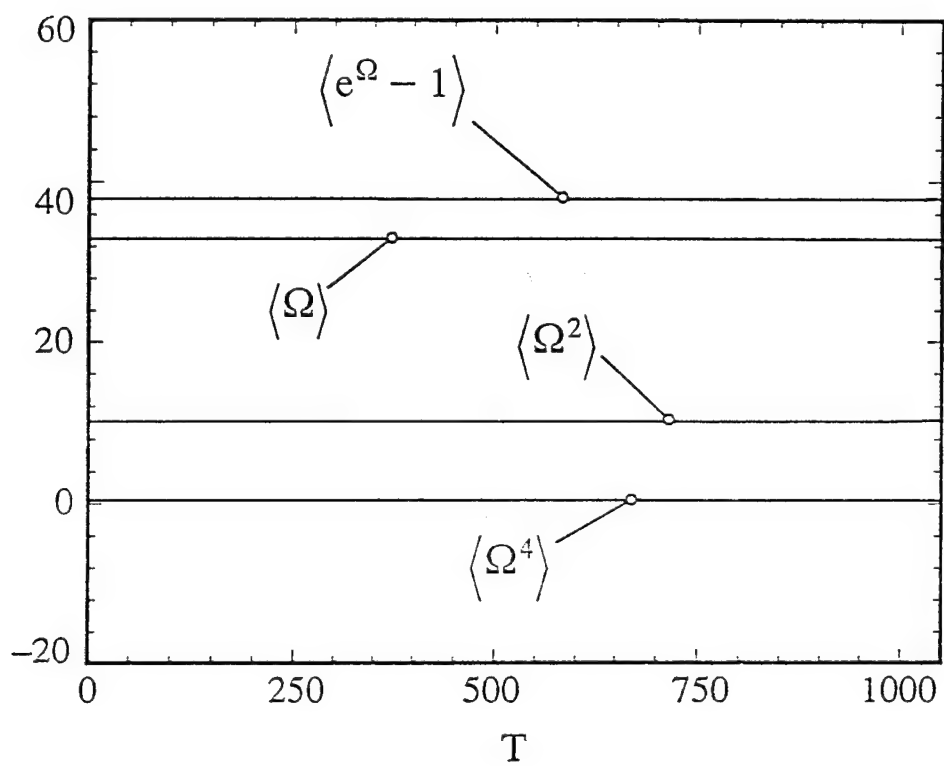
Fig. 38. Vorticity conservation in a central difference scheme.
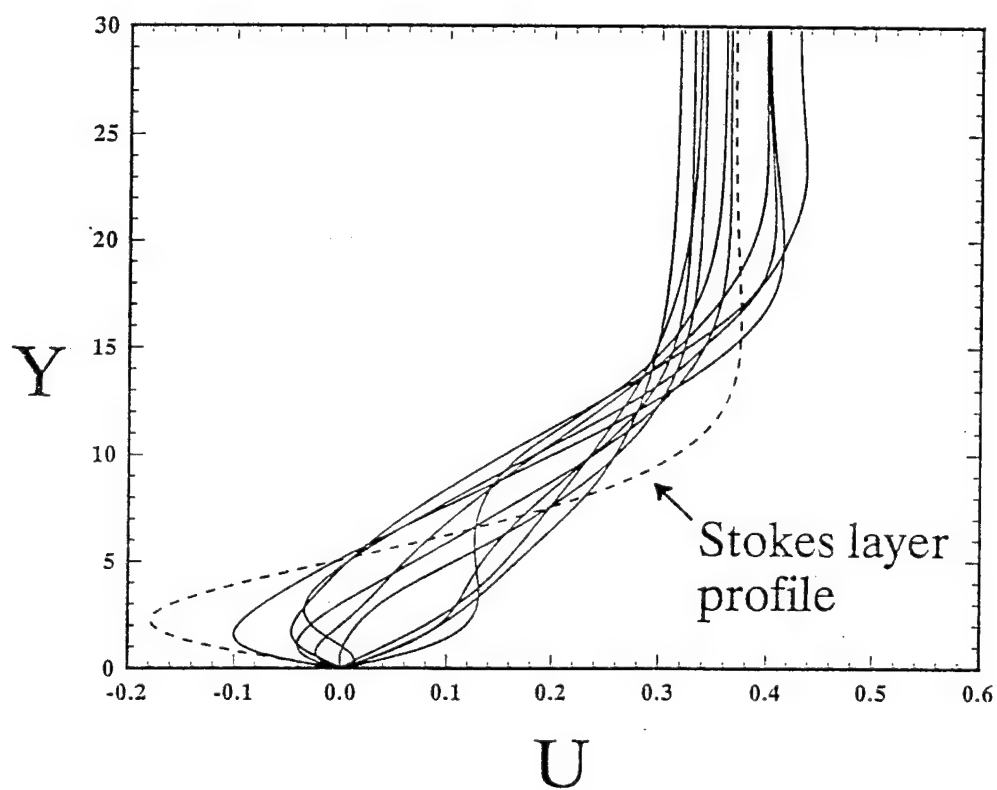
Fig. 39. Streamwise velocity profiles at a typical stream-wise station in a viscous Rayleigh instability.
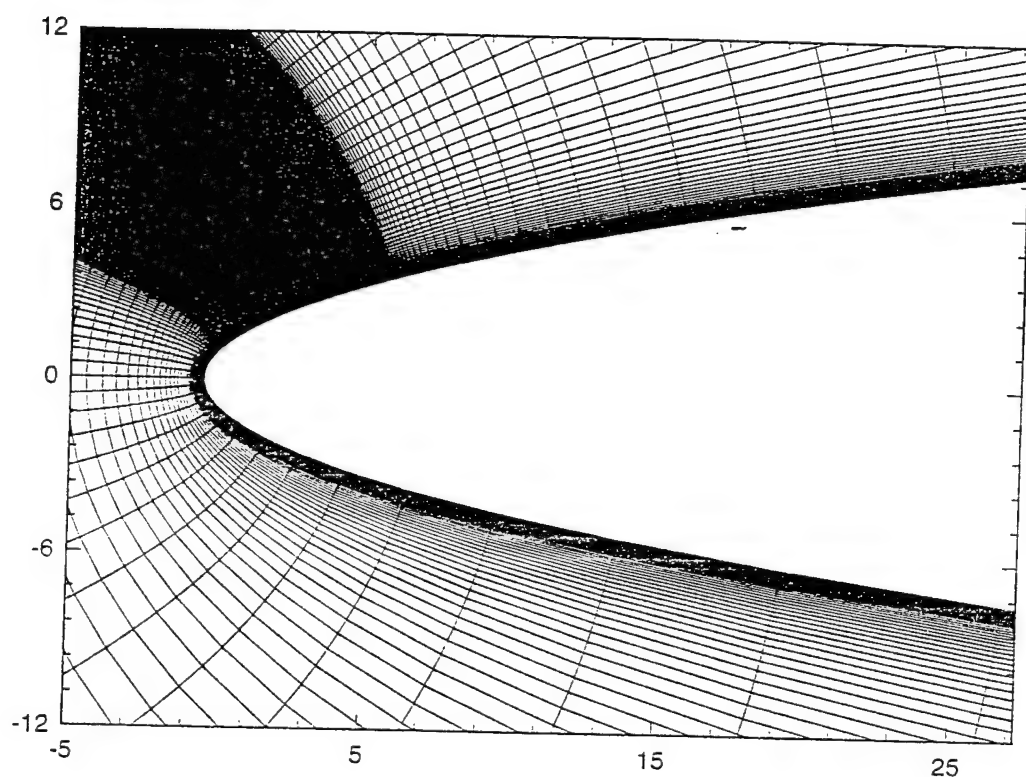
Fig. 40. Typical mesh used for the Navier–Stokes computations on a parabola at angle of attack. Up to 500 streamwise points have been used in the clustered region near the leading edge.
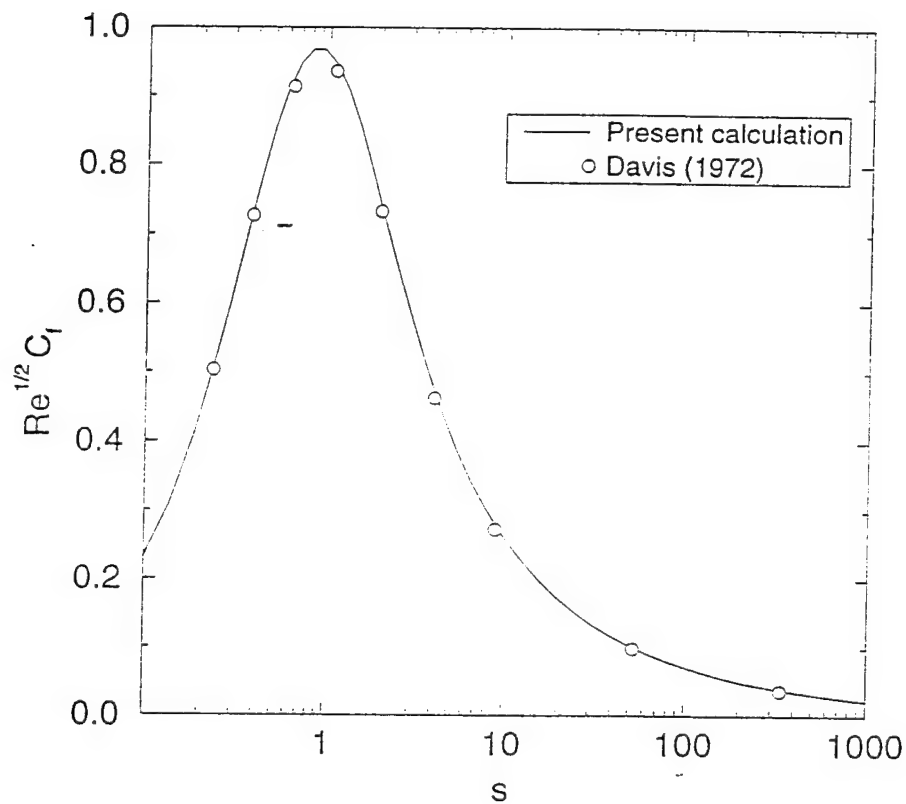
Fig. 41. Comparison of steady state limit of the unsteady
Navier–Stokes solutions with Davis (1972) computa-
tions of flow past parabola at zero angle of attack.
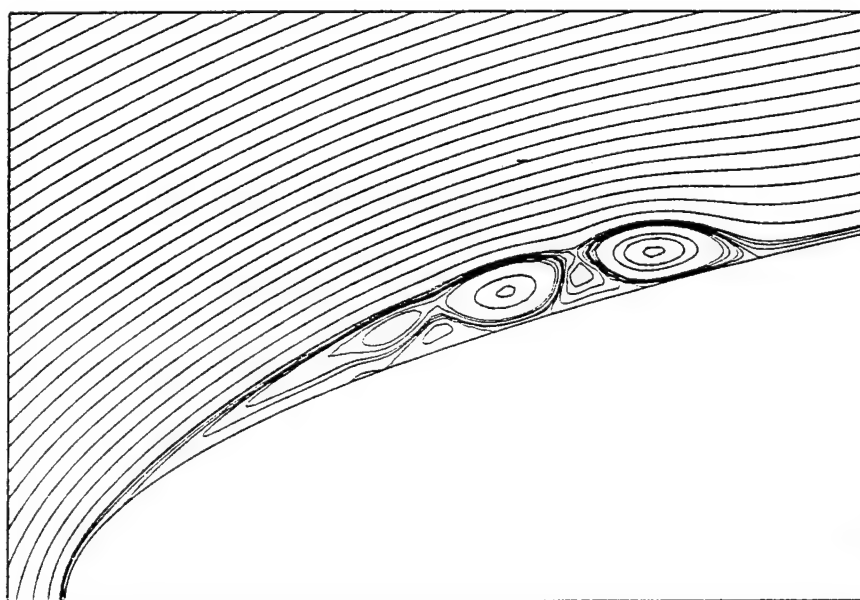
Fig. 42. Streamlines for Navier−Stokes solution past parabola with an impulsively applied no−slip condition.
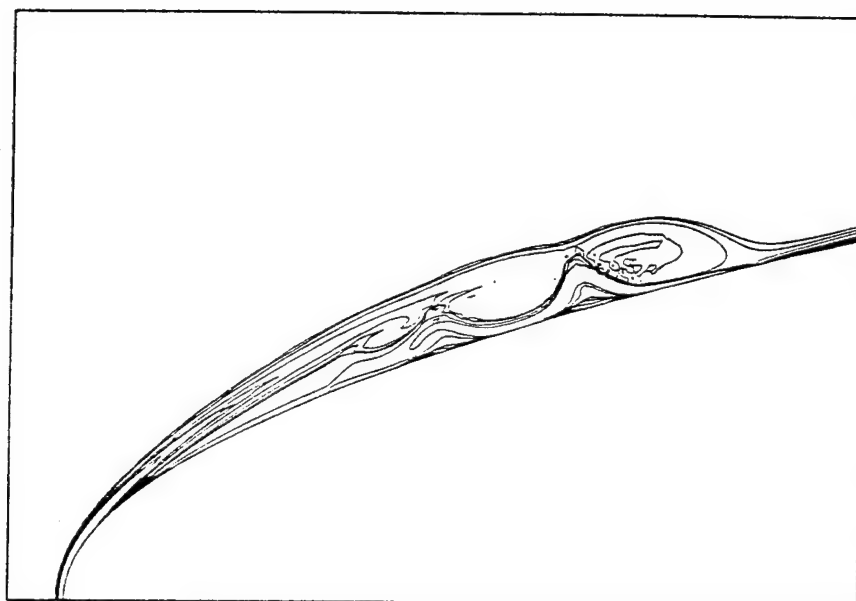
Fig. 43. Vorticity contours for Navier−Stokes solution past parabola with an impulsively applied no−slip condition.

t=10.0

t=20.0

t=30.0

t=32.5
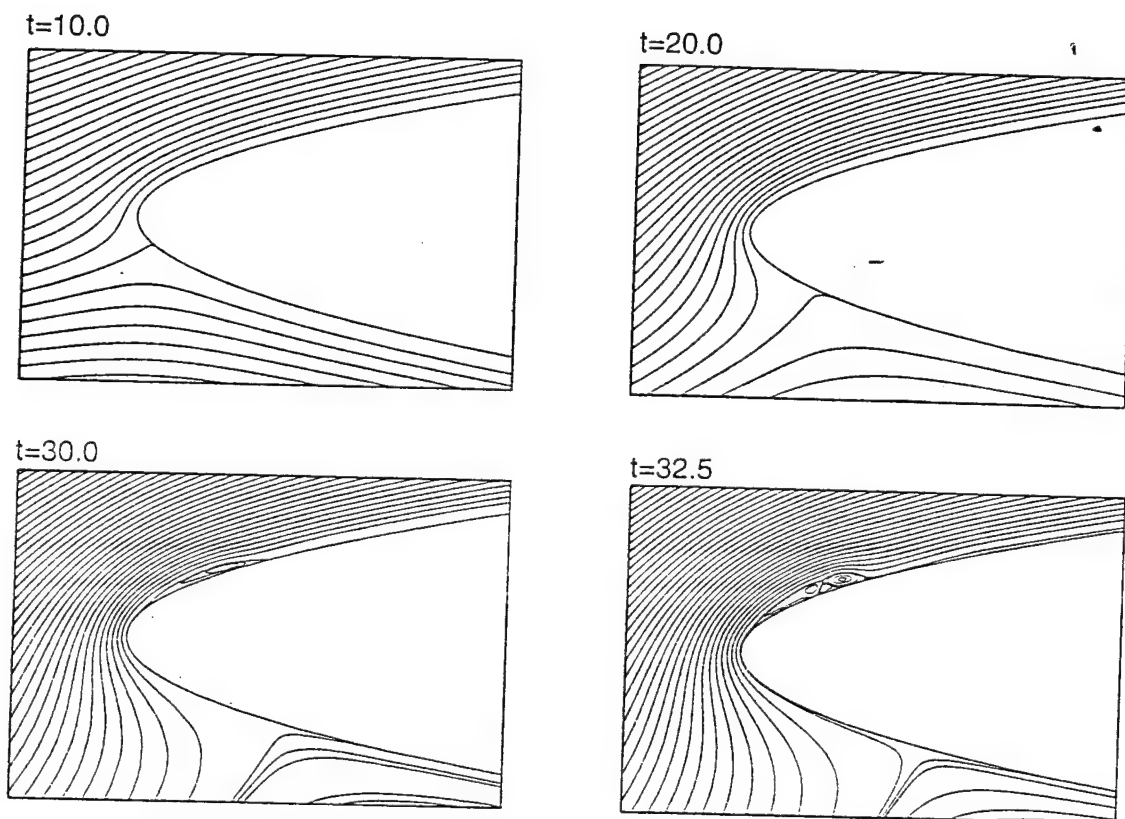
Fig. 44. Streamlines for Navier–Stokes solution past parabola undergoing smooth pitch–up.
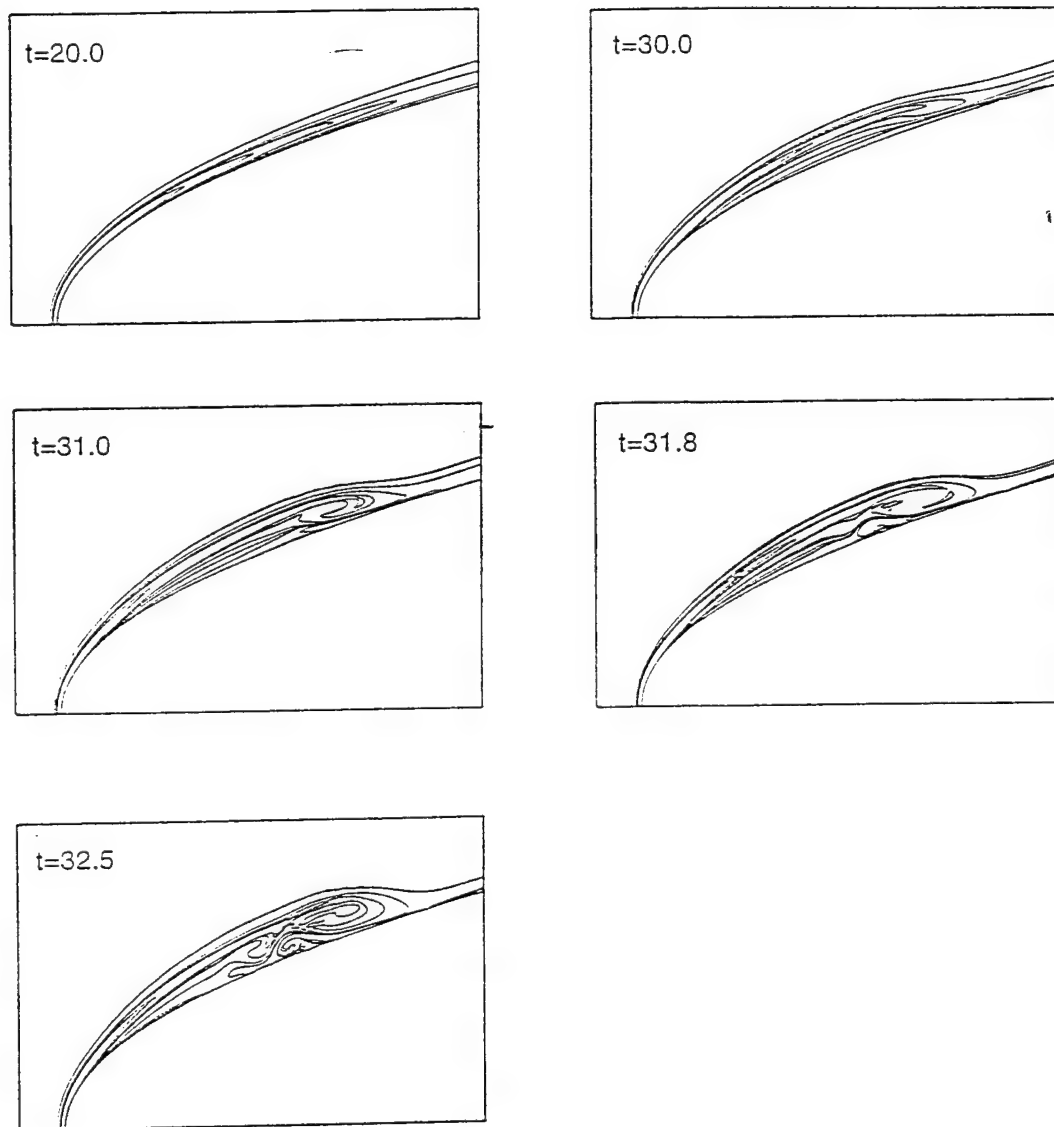
Fig. 45. Vorticity contours for Navier−Stokes solution past parabola undergoing smooth pitch−up.
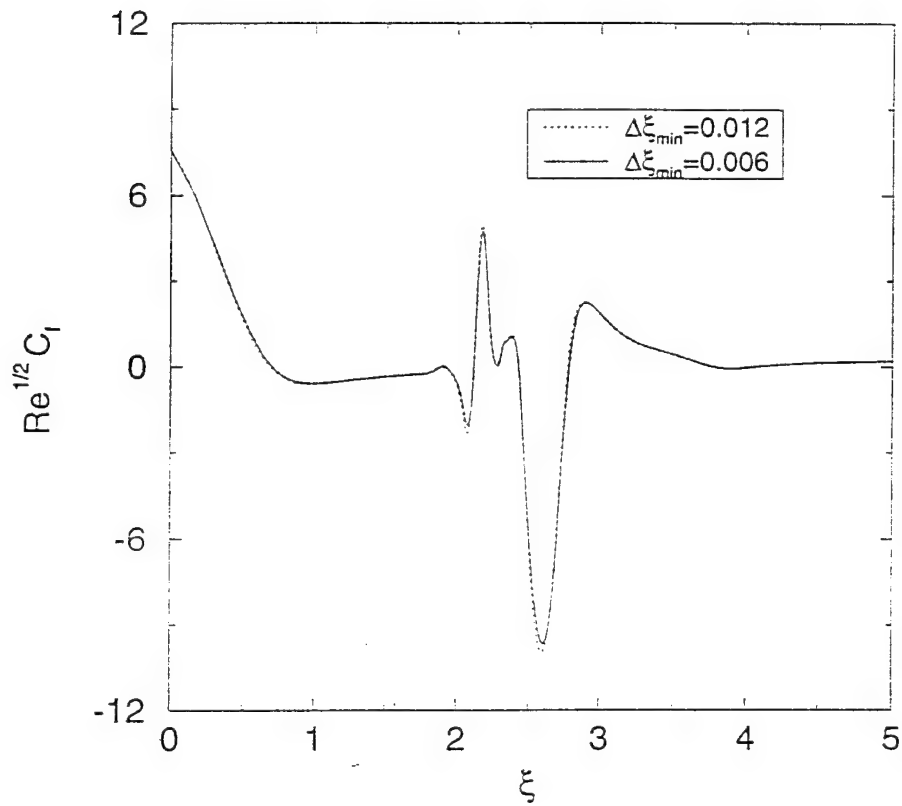
Fig. 46. Verification of streamwise grid–independence using wall shear for Navier–Stokes solution past parabola undergoing smooth pitch–up.
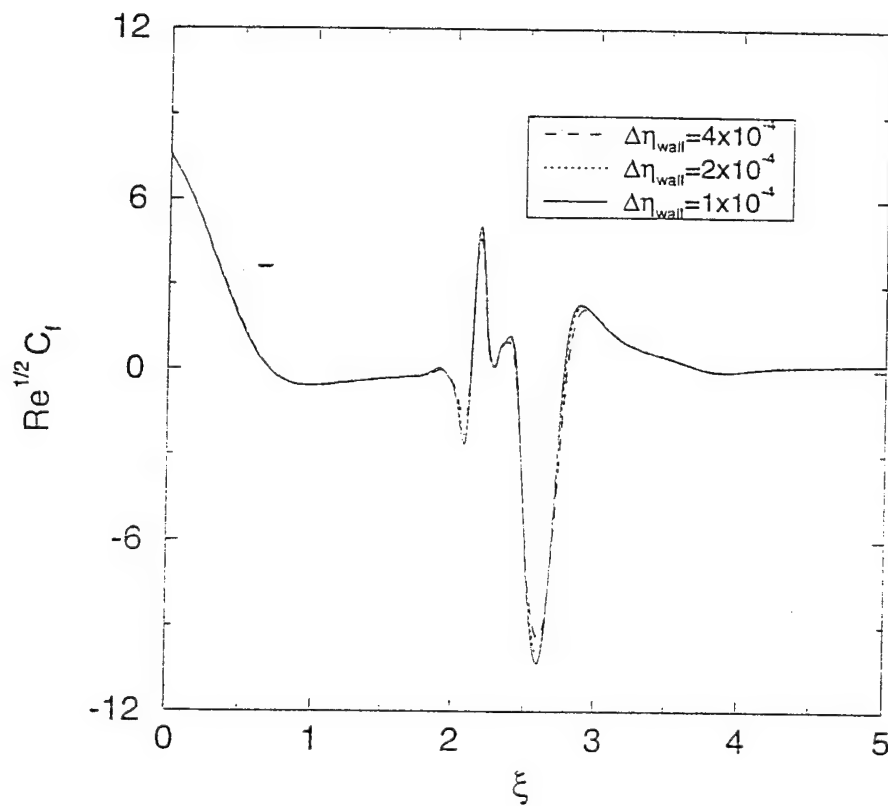
Fig. 47. Verification of normal grid–independence using wall shear for Navier–Stokes solution past parabola undergoing smooth pitch–up.
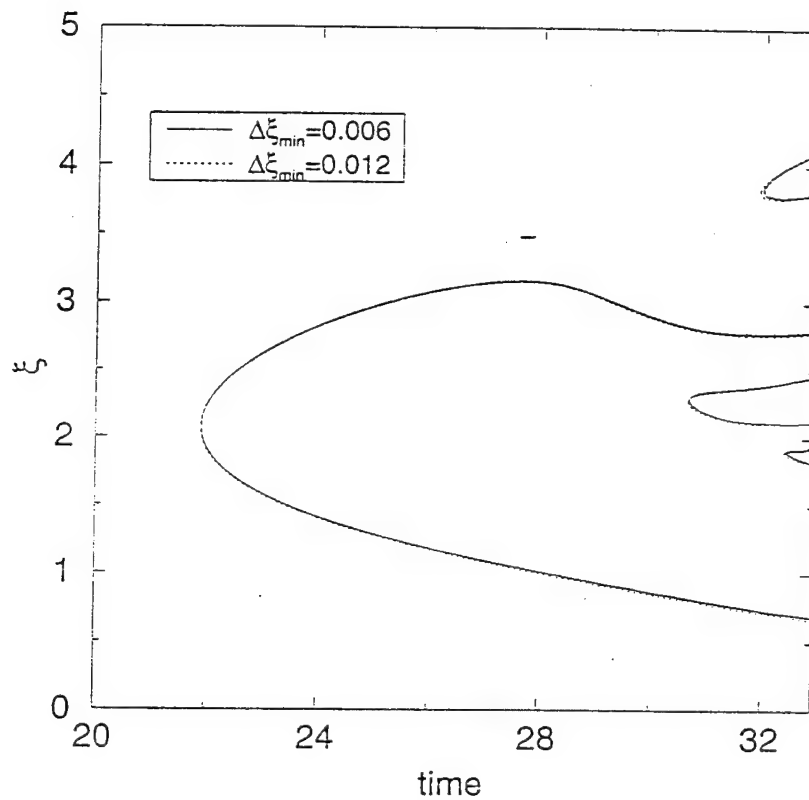
Fig. 48. Primary and secondary separation lines for Navi-
er–Stokes solution past parabola undergoing smooth
pitch–up. Also shown are comparisons at different grid
spacings.
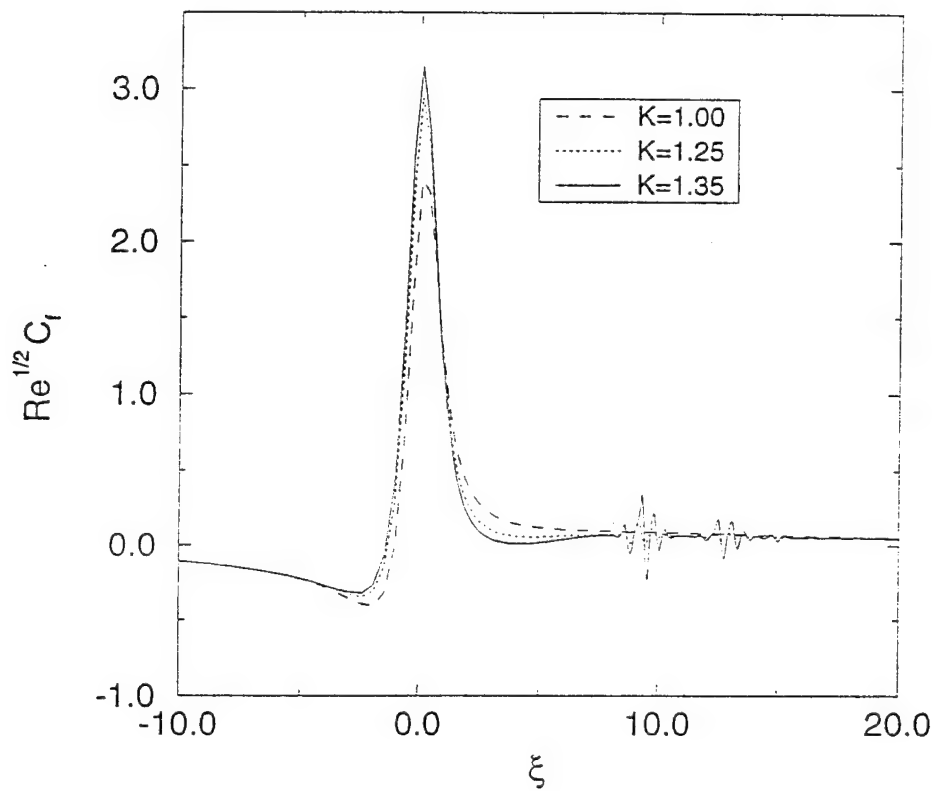
Fig. 49. Navier−Stokes solutions for an impulsive change in angle of attack which initially remains attached. Shown are local disturbance developments and the increase in growth rate as the base flow approaches separation.
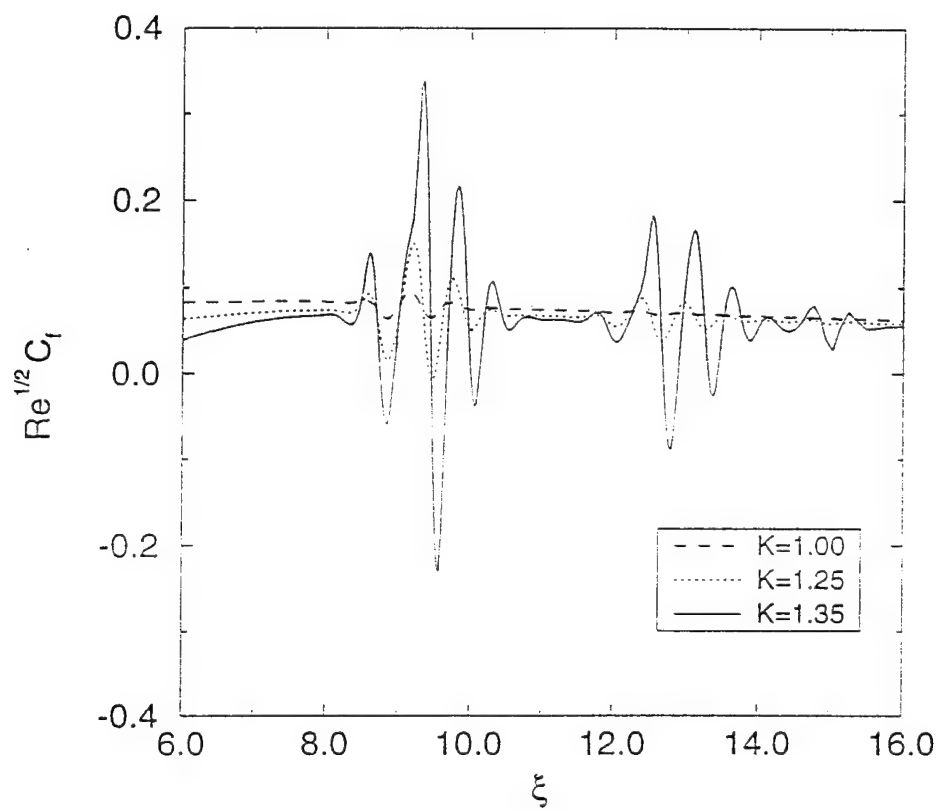
Fig. 50. Blow−up of the local oscillatory shear stress in figure 49, showing the multiple separations.
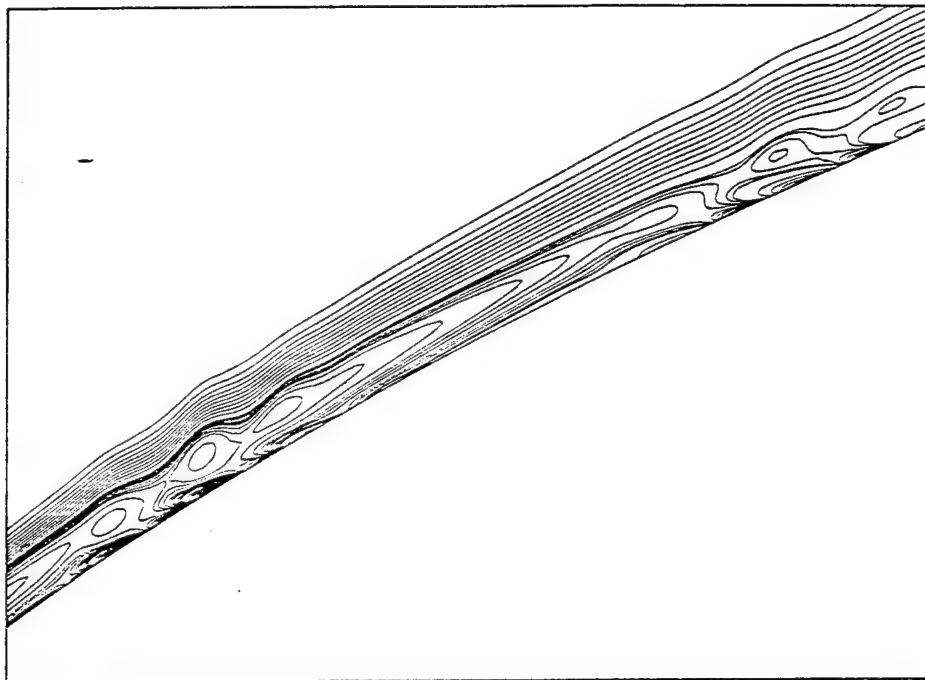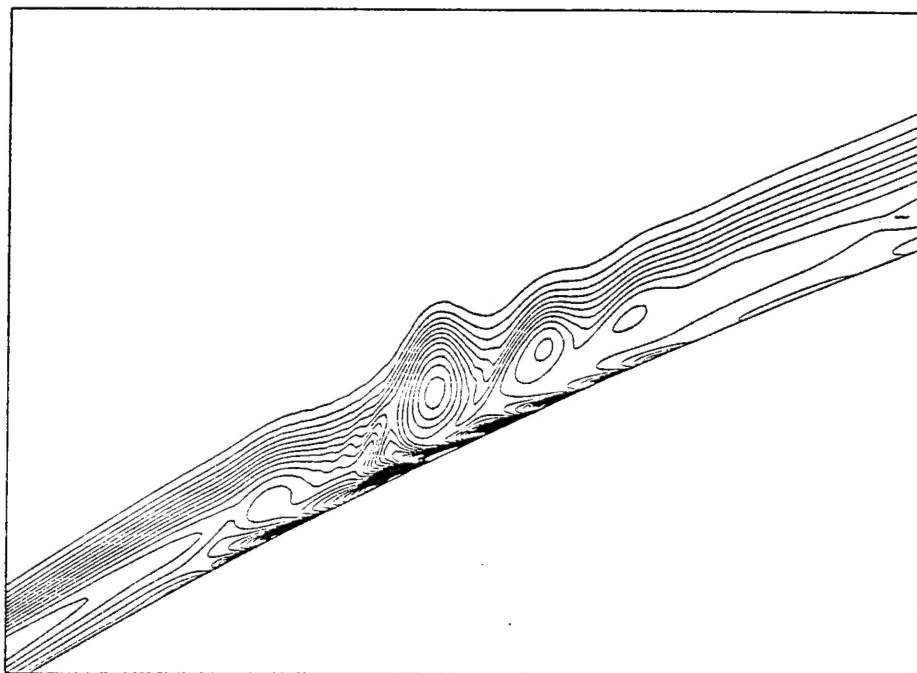
Fig. 51. Vorticity contours in the boundary layer corresponding to figure 50. Navier−Stokes solutions for an impulsive change in angle of attack which initially remains attached.
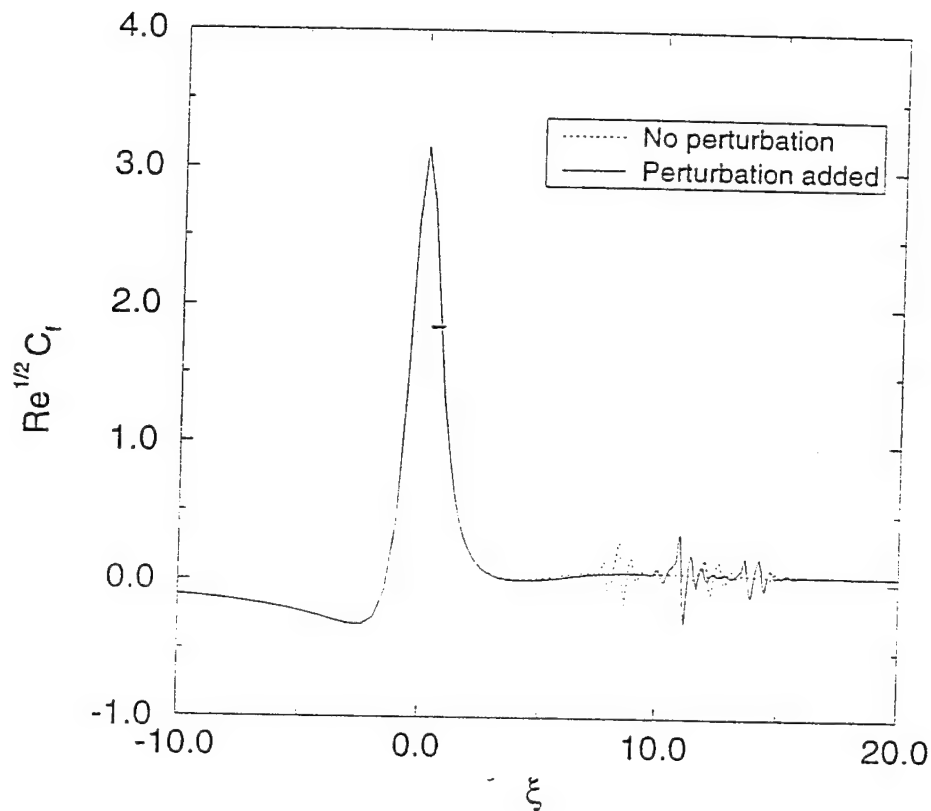
Fig. 52. Effect of surface perturbations on Navier–
Stokes solutions for impulsive changes in angle of attack
in attached flows. Disturbances increase final distur-
bance amplitude.

Fig. 53. Vorticity contours in the boundary layer corresponding to figure 52. Navier–Stokes solutions for an impulsive change in angle of attack which initially remains attached, with surface perturbations.
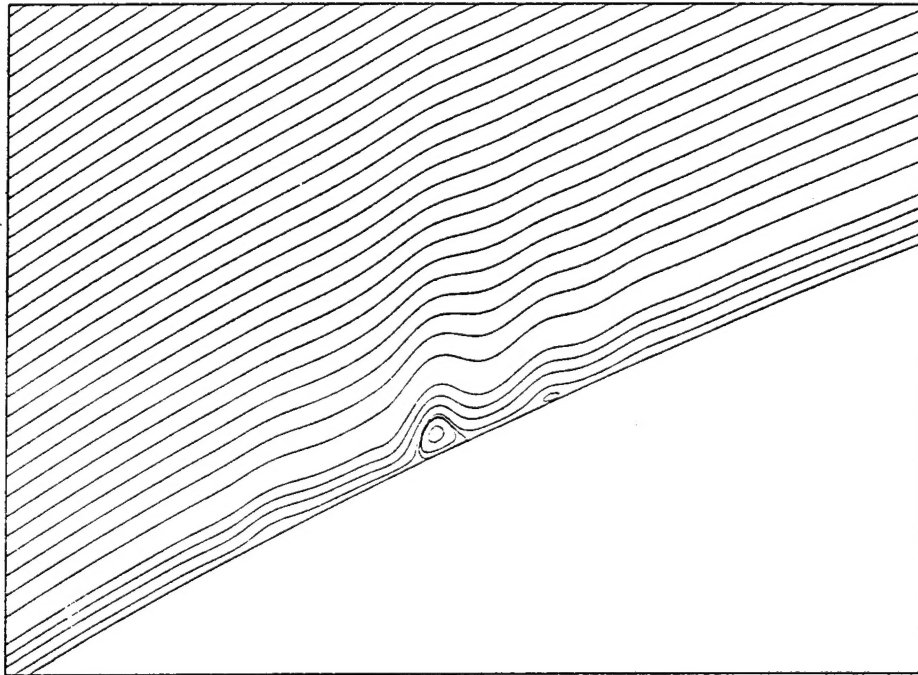
Fig. 54. Streamfunction contours in the boundary layer corresponding to figure 52. Navier–Stokes solutions for an impulsive change in angle of attack which initially remains attached (with surface perturbations).
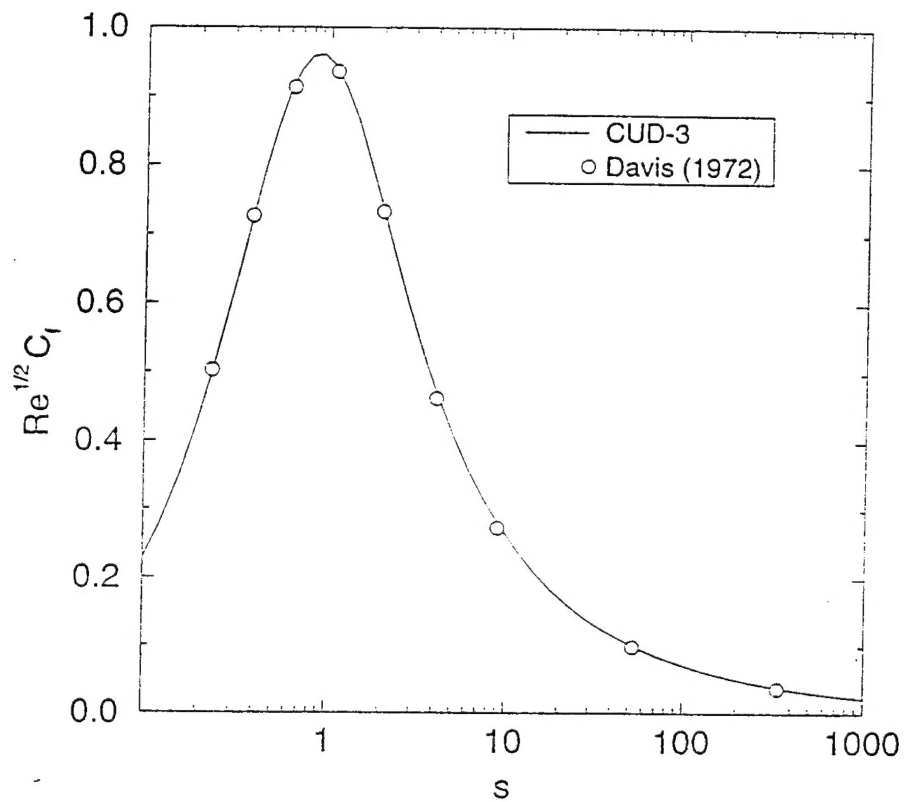
Fig. 55. Comparison of steady state limit of the unsteady Navier–Stokes CUD–3 solutions with Davis (1972) computations of flow past parabola at zero angle of attack.
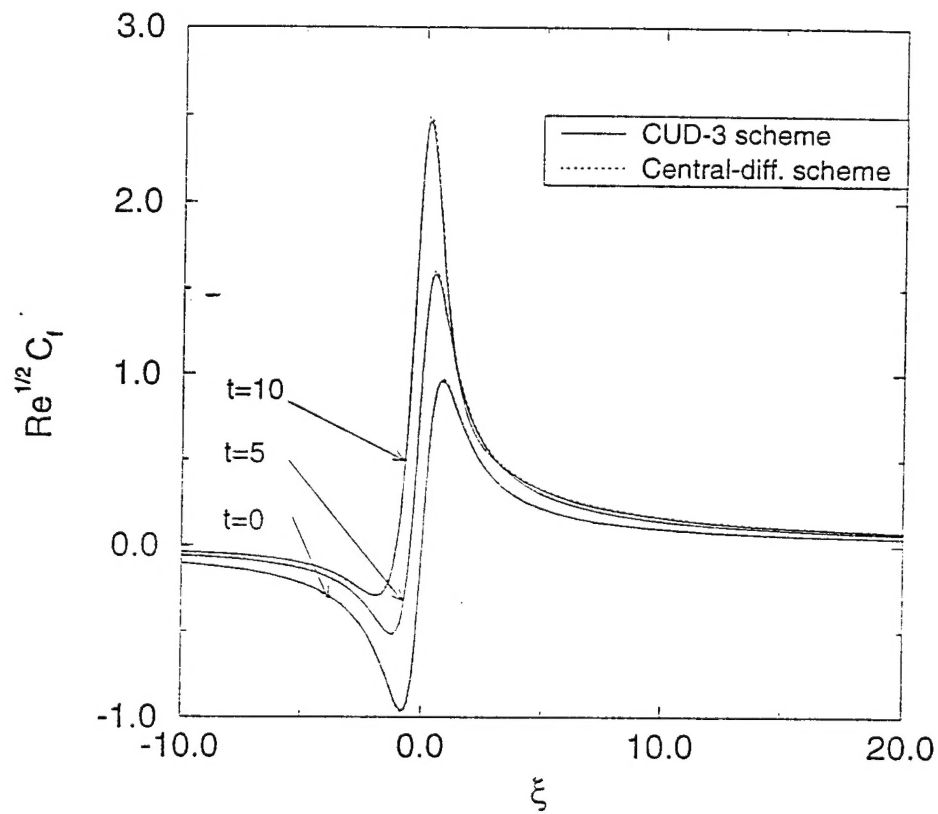
Fig. 56. Comparison of Navier−Stokes CUD−3 skin friction with central difference skin friction at early times in a parabola undergoing smooth pitch−up.